

ADVANCED SIGNAL PROCESSING STRATEGIES FOR RESILIENT SATELLITE NAVIGATION USING MULTI-CORRELATOR STRUCTURES

Von der Fakultät für Elektrotechnik und Informationstechnik der
Rheinisch-Westfälischen Technischen Hochschule Aachen zur
Erlangung des akademischen Grades eines

Doktors der Ingenieurwissenschaften

genehmigte Dissertation

vorgelegt von

Christian Siebert, M.Sc.

aus Kassel, Deutschland

Berichterstatter:

1. Univ.-Professor Dr.-Ing. habil. Michael Meurer
2. Univ.-Professor Mag. Dr. habil. Thomas Pany

Tag der mündlichen Prüfung: 07.04.2025

Diese Dissertation ist auf den Internetseiten der Universitätsbibliothek
online verfügbar.

Abstract

Positioning and timing has become a crucial component in a broad field of applications. This spans from positioning and navigation in aeronautics, maritime, and automobile applications to system critical time synchronization of power grids or mobile telecommunication networks. On a global scale, this is achieved already today with global navigation satellite systems (GNSSs). However, environmental conditions can affect their performance and reliability. A well-known threat in this context is the multipath propagation. Objects in the nearer receiver environment reflect the satellite signals, which can cause errors or even failure of conventional GNSS receivers.

A second threat are atmospheric effects, in particular due to the ionosphere. Solar radiation ionizes the remaining atoms and molecules in this layer of the atmosphere. The resulting free electrons introduce additional signal delays. As this effect is frequency-dependent, it can be largely eliminated with a multi-frequency receiver using the ionosphere-free combination. Unfortunately, other errors, such as multipath errors, tend to be amplified in this process. Multipath propagation depicts therewith a limiting factor in GNSS.

In the literature, a large number of approaches have been proposed in the past to mitigate the effect of multipath. They vary in effectiveness and complexity depending on the application and requirements they were developed for. Nevertheless, a certain gap has been identified in the literature regarding solutions, that are effective, provide a good noise performance, and are of feasible complexity.

In this work, a multipath mitigating algorithm has been developed, that is designed to fill this gap. Propagation characteristics are estimated in the form of a line-of-sight (LOS) delay and an impulse response that represents multipath components. This enables an improved delay estimation. The approach will be analyzed with synthetic data, hardware emulations, as well as actual measurement data, confirming that it fulfills the design criteria. In addition, the integration into an advanced vector tracking (VT) receiver architecture has been shown. The joint processing of all satellites increases reliability in challenging environments and depicts with the increased multipath resilience of the proposed algorithm a strong combination. Moreover, the extension to simultaneously processing multiple frequencies has been explored. The therewith achieved observability of the ionospheric delays is used to actively estimate this effect. The multipath resilience of the underlying developed algorithm allows for an accurate estimation, also in multipath environments. Last but not least, the extension to antenna arrays has been explored. The therewith additionally available spatial domain allows to overcome the temporal resolution limit that was limiting the effectiveness of the proposed solution against short delay multipaths.

Contents

Abstract	iii
List of Figures	ix
List of Tables	xi
Abbreviations	xiii
Nomenclature	xvii
1 Introduction	1
1.1 Motivation	1
1.2 State of the Art	2
1.2.1 Multipath Detection	5
1.2.2 Multipath Mitigation	5
1.2.3 Multipath Estimation	7
1.3 Research Questions	10
1.4 Outline	12
2 Multi-Correlator-Based Multipath Mitigation	15
2.1 Signal Model	15
2.2 Kalman Filtering Algorithm	18
2.2.1 Prediction Step	19
2.2.2 Update Step	19
2.3 Multipath Mitigating Extended Kalman Filter	20
2.3.1 Correlator Bank	20
2.3.2 Joint Estimation of Code Delay and Channel Impulse Response	21
2.3.3 Analysis of Computational Complexity	25
2.3.3.1 Uniform Sampling With Reduced Correlator Bank Width	26
2.3.3.2 Nonuniform Sampling	28
2.3.4 Receiver Architecture	28
2.3.5 Local Pseudorandom Noise Replicas	29
2.3.6 Effect of Doppler	29
2.3.7 Algorithm Initialization	30
3 Analysis of Scalar Tracking With Multi-Correlator-Based Multipath Mitigation	31
3.1 Simulation Parameters	31

3.2	Multipath Error Envelopes	32
3.2.1	Comparison With Other Multipath Mitigation Techniques . . .	36
3.2.2	Low-Complexity Variants	37
3.2.2.1	Uniform Sampling With Reduced Correlator Bank Width	38
3.2.2.2	Nonuniform Sampling	40
3.2.3	Effect of Measurement Noise Variance of Constraint	41
3.3	Dynamic Response	43
3.3.1	Step Response	45
3.3.2	Convergence Behavior	48
3.4	Noise Performance	49
3.5	Initialization Robustness	50
4	Vector Tracking Enhanced Multipath Mitigation	53
4.1	Vector Delay/Frequency Locked Loop Algorithm	54
4.1.1	Process Model	54
4.1.2	Measurement Model	55
4.1.3	Tracking Loop Closure	57
4.1.4	Receiver Architecture	58
4.2	Integration of Multipath Mitigating EKF	59
4.2.1	Receiver Architecture	59
4.3	Implementation Details	60
4.3.1	Concealed Satellites	60
4.3.2	Disabling Vector Tracking Loop	60
5	Estimation and Mitigation of Ionospheric Propagation Error	63
5.1	Ionospheric Multipath Mitigating EKF	63
5.1.1	Process Model	64
5.1.2	Measurement Model	65
5.1.3	Receiver Architecture	67
5.1.4	Hardware Imperfections	67
5.2	Summary	68
6	Performance Analysis and Validation	69
6.1	Setup of Simulations and Measurements	69
6.1.1	Ground Truth	72
6.2	Multipath Mitigating EKF	74
6.2.1	Hardware Emulation	74
6.2.2	Suburban Measurement Campaign	76
6.3	Vector Tracking Enhanced Multipath Mitigation	79
6.3.1	Simulated Urban Canyon	81
6.3.2	Urban Measurement Campaign	83
6.4	Ionospheric Multipath Mitigating EKF	87
6.4.1	Synthetic Signals	88
6.4.2	Hardware Emulation	89
6.4.3	Actual Measurements	91

7	Extension of Multi-Correlator-Based Multipath Mitigation to Antenna Arrays	95
7.1	Signal Model	95
7.2	Array Multipath Mitigating EKF	97
7.2.1	Correlator Bank	98
7.2.2	Joint Estimator	98
7.2.3	Receiver Architecture	100
7.3	Performance Evaluation	101
7.3.1	Multipath Mitigation	102
7.3.2	Noise Performance	103
8	Conclusion	107
8.1	Summary and Contributions	107
8.2	Recommendations	109
A	Jacobian Matrix for Multipath Mitigating EKF	111
B	Jacobian Matrix for Ionospheric Multipath Mitigating EKF	113
C	Jacobian Matrix for Array Multipath Mitigating EKF	115
D	Gauss-Jordan Elimination Complexity	117
	Bibliography	123
	Curriculum Vitae	137

List of Figures

2.1	Block diagram of signal processing chain	15
2.2	Proposed receiver architecture for the MMEKF	29
3.1	Multipath error envelopes	34
3.2	CIRs for different multipath delays	35
3.3	Multipath error envelopes of different multipath mitigation techniques	37
3.4	Multipath error envelopes for different numbers of correlators	39
3.5	Effect of measurement noise scaling	39
3.6	Error metrics for different numbers of correlators	39
3.7	Error metrics for different nonuniform correlator distributions over β	41
3.8	Multipath error envelopes for different σ_{constr}	42
3.9	Error metrics over different σ_{constr}	43
3.10	Error metrics for different nonuniform correlator distributions and σ_{constr}	44
3.11	Step response	46
3.12	Step response errors over STD of constraint	46
3.13	Step response errors over STD of constraint and number of correlators	47
3.14	Step response errors over STD of constraint and β	47
3.15	Convergence behavior	49
3.16	Convergence behavior of CIR estimate	50
3.17	Convergence behavior for different channel coefficient process noise STDs	51
3.18	Noise performance	51
3.19	Robustness against initialization errors	52
4.1	VDFLL receiver architecture	59
4.2	Proposed VDFLL receiver architecture with MMEKF	60
5.1	Proposed receiver architecture for IMMEKF	68
6.1	Schematic illustrations of the different measurement setups.	71
6.2	Hardware emulation setup	71
6.3	Satellite constellation of hardware emulations	72
6.4	Measurement vehicle	72
6.5	Detailed schematic illustration of the measurement setup.	73
6.6	Position RMSE of static hardware emulation scenario	75
6.7	Estimated CIRs of static hardware emulation scenario	75
6.8	Route of suburban measurement campaign	77
6.9	Satellite constellation of suburban measurement campaign	77
6.10	Results of suburban measurement campaign	78

6.11	Representation of suburban position estimates in 3D renderings	78
6.12	Altitude errors at the beginning of the suburban measurement campaign	80
6.13	Results of section of suburban measurement campaign	80
6.14	Simulated urban canyon environment	82
6.15	Number of GNSS signals during the urban canyon simulation	83
6.16	Results of urban canyon simulation	84
6.17	Route of urban measurement campaign	85
6.18	Satellite constellation of urban measurement campaign	85
6.19	Results of urban measurement campaign	86
6.20	Representation of urban position estimates in 3D renderings	86
6.21	Results of section of urban measurement campaign	87
6.22	Ionospheric TEC estimates from the IMMEKF using synthetic signals	89
6.23	Tracking errors for multi-frequency processing techniques using synthetic signals	90
6.24	Position RMSE using multi-frequency processing of hardware emulation	91
6.25	Ionospheric TEC estimates of IMMEKF of hardware emulation	92
6.26	Satellite constellation of rooftop measurement	92
6.27	Position RMSE of rooftop measurement campaign	93
6.28	Ionospheric TEC estimates of IMMEKF of rooftop measurement data	94
7.1	Schematic illustration of an antenna array	96
7.2	Proposed receiver architecture for the AMMEKF	101
7.3	Considered array configurations for the performance evaluation	102
7.4	Steady-state tracking error of the proposed AMMEKF using 4 antenna elements	103
7.5	Steady-state tracking error of the proposed AMMEKF using 16 antenna elements	104
7.6	Multipath errors for different multipath elevation angles	105
7.7	Noise performance of the proposed AMMEKF	106

List of Tables

1.1	Overview of existing stand-alone signal processing techniques for multipath propagation	6
2.1	Number of elementary arithmetic operations for the MMEKF	27
3.1	General simulation parameters	32
3.2	Parameters of MMEKF	32
3.3	Measurement noise STD of constraining measurement	33
3.4	Number of elementary operations of different multipath mitigation algorithms	37
6.1	GPS satellite parameters of hardware emulation for MMEKF	74
6.2	Parameters for VT EKF	81
6.3	IMMEKF specific parameters	88
6.4	Satellite and multipath parameters of hardware emulation for IMMEKF	90
D.1	First part of Gauss-Jordan Elimination	118
D.2	Second part of Gauss-Jordan Elimination	121

Abbreviations

3DBM	<u>3</u> <u>d</u> imensional <u>b</u> uilding <u>m</u> odel
ADC	<u>a</u> nalog-to- <u>d</u> igital <u>c</u> onverter
AIC	<u>A</u> kaike information <u>c</u> riterium
AMMEKF	array <u>M</u> MEKF
APME	<u>a</u> - <u>p</u> osteriori <u>m</u> ultipath <u>e</u> stimation
BGD	<u>b</u> roadcast <u>g</u> roup <u>d</u> elay
BOC	<u>b</u> inary <u>o</u> ffset carrier
BPSK	<u>b</u> inary <u>p</u> hase- <u>s</u> hift <u>k</u> eying
C/A	<u>c</u> oarse/ <u>a</u> cquisition
C/D	<u>c</u> ontinues-to- <u>d</u> iscrete-time
C/N₀	<u>c</u> arrier-to- <u>n</u> oise density ratio
CADLL	<u>c</u> oupled <u>a</u> mplitude <u>d</u> elay <u>l</u> ocked <u>l</u> oop
CIR	<u>c</u> hannel <u>i</u> mpulse <u>r</u> esponse
DDC	<u>d</u> ouble- <u>d</u> elta correlator
DET	<u>d</u> eterministic beamformer
DLL	<u>d</u> elay locked loop
DLR	<u>D</u> eutsches Zentrum für <u>L</u> uft- und <u>R</u> aumfahrt (German Aerospace Center)
DOA	<u>d</u> irection of <u>a</u> rrival
DOP	<u>d</u> ilution of <u>p</u> recision
DPE	<u>d</u> irect <u>p</u> osition <u>e</u> stimation
e1/e2	<u>e</u> arly1/ <u>e</u> arly2
ECEF	<u>E</u> arth- <u>c</u> entered, <u>E</u> arth- <u>f</u> ixed
EKF	<u>e</u> xtended <u>K</u> alman <u>f</u> ilter
ELP	early <u>l</u> ate <u>p</u> hase
ELS	early-late <u>s</u> lope
EML	early <u>m</u> inus late
FIMLA	<u>f</u> ast <u>i</u> terative <u>M</u> L <u>a</u> lgorithm
FLL	<u>f</u> requency locked loop
GDOP	<u>g</u> eometric <u>d</u> ilution of <u>p</u> recision
GGTO	<u>G</u> alileo- <u>G</u> PS <u>t</u> ime <u>o</u> ffset
GNSS	<u>g</u> lobal <u>n</u> avigation <u>s</u> atellite <u>s</u> ystem
GPS	<u>G</u> lobal <u>P</u> ositioning <u>S</u> ystem
HRC	<u>h</u> igh- <u>r</u> esolution <u>c</u> orrelator
IF	<u>i</u> ntermediate frequency
IGS	<u>I</u> nternational <u>G</u> NSS <u>S</u> ervice

IMMEKF	ionospheric <u>MMEKF</u>
IMU	<u>i</u> nertial <u>m</u> easurement <u>u</u> nit
IR	<u>i</u> nfrared
KF	<u>K</u> alman <u>f</u> ilter
LEO	<u>l</u> ow <u>E</u> arth <u>o</u> rbit
LHCP	<u>l</u> eft- <u>h</u> and <u>c</u> ircular <u>p</u> olarization
LiDAR	<u>l</u> ight <u>d</u> etection and <u>r</u> anging
LM	<u>L</u> evenberg- <u>M</u> arquardt
LOS	<u>l</u> ine- <u>o</u> f- <u>s</u> ight
MDL	<u>m</u> inimum <u>d</u> escriptive <u>l</u> ength
MEDLL	<u>m</u> ultipath <u>e</u> stimating <u>d</u> elay <u>l</u> ocked <u>l</u> oop
MET	<u>m</u> ultipath <u>e</u> limination <u>t</u> echnique
ML	<u>m</u> aximum <u>l</u> ikelihood
MMEKF	<u>m</u> ultipath <u>m</u> itigating <u>EKF</u>
MMSE	<u>m</u> inimum <u>m</u> ean <u>s</u> quare <u>e</u> rror
MMT	<u>m</u> ultipath <u>m</u> itigation <u>t</u> echnology
NCO	<u>n</u> umerically- <u>c</u> ontrolled <u>o</u> scillator
NLOS	<u>n</u> on- <u>l</u> ine- <u>o</u> f- <u>s</u> ight
OS	<u>O</u> pen <u>S</u> ervice
PLL	<u>p</u> hase <u>l</u> ocked <u>l</u> oop
PNT	<u>p</u> osition, <u>n</u> avigation, and <u>t</u> iming
PPP	<u>p</u> recise <u>p</u> oint <u>p</u> ositioning
PRN	<u>p</u> seudorandom <u>n</u> oise
PSR	<u>p</u> seudorange
PVT	<u>p</u> osition, <u>v</u> elocity, and <u>t</u> ime
RAIM	<u>r</u> eciever <u>a</u> utonomous <u>i</u> ntegrity <u>m</u> onitoring
RF	<u>r</u> adio <u>f</u> requency
RHCP	<u>r</u> ight- <u>h</u> and <u>c</u> ircular <u>p</u> olarization
RMSE	<u>r</u> oot- <u>m</u> ean-square <u>e</u> rror
SAGE	space <u>a</u> lternating <u>g</u> eneralized <u>e</u> xpectation-maximization
SAM	<u>s</u> lope <u>a</u> symmetric <u>m</u> etric
SOP	<u>s</u> ignal <u>o</u> f <u>o</u> ppportunity
SQM	<u>s</u> ignal <u>q</u> uality <u>m</u> onitoring
ST	<u>s</u> calar <u>t</u> racking
STD	<u>s</u> tandard <u>d</u> eviation
TEC	<u>t</u> otal <u>e</u> lectron <u>c</u> ontent
TECU	<u>T</u> EC <u>u</u> nit
TGD	<u>t</u> iming <u>g</u> roup <u>d</u> elay
TOA	<u>t</u> ime <u>o</u> f <u>a</u> rrival
TTFF	<u>t</u> ime <u>t</u> o <u>f</u> irst <u>f</u> ix
UWB	<u>u</u> ltra- <u>w</u> ide <u>b</u> and
VDFLL	<u>v</u> ector <u>d</u> elay/ <u>f</u> requency <u>l</u> ocked <u>l</u> oop
VT	<u>v</u> ector <u>t</u> racking

WSS wheel speed sensor

WSSUS wide-sense stationary uncorrelated scattering

Nomenclature

Signal model, correlation, and multipath mitigating EKF related variables

Symbol	Description	Unit of component
B	One-sided signal bandwidth	Hz
\mathbf{C}	Correlator bank	
c_0	Speed of light	m/s
d	Navigation data bits	
f_c	Carrier frequency	Hz
$f_{D,\text{carr}}$	Carrier Doppler	Hz
f_s	Sampling frequency	Hz
$f_T(\tau)$	Tukey window function	
g	Impulse response for chip shaping	1/s
$h(t, \tau)$	Time-varying tapped delay line channel model	1/s
$h^{(l_h)}$	Complex channel coefficient of l_h -th channel tap	1/s
i	GNSS signal index	
j	GNSS signal band index	
k	Sampling index	
l_c	Correlator index	
l_h	Channel tap index	
L_c	Number of causal correlators	
L_h	Number of causal channel taps	
m	Modulating sequence for PRN sequence	
n	Sample index	
N	Number of samples within the integration interval T_{int}	
N_{band}	Number of GNSS signal bands	
N_{corr}	Number of correlators in the correlator bank	
N_{eq}	Number of equally spaced correlators for the nonuniform correlator spacing	
N_{sys}	Number of GNSSs used	
$N_{\text{sig},j}$	Number of GNSS signals in the j -th band	
N_{tap}	Number of channel taps	
$\mathbf{R}_{\hat{\eta}_C}$	Covariance matrix of noise of correlator outputs	
$\mathbf{R}_{w\hat{\eta}_C}$	Scaled covariance matrix of noise of correlator outputs	
s	Modulated and chip-shaped PRN signal with navigation data	
\bar{s}	PRN sequence	

t	Time	s
T_c	Duration of one PRN code chip	s
T_{code}	PRN code period	s
$T_c^{(l_c)}$	Correlator position of the l_c -th correlator	s
$T_h^{(l_h)}$	Channel tap delay of l_h -th channel tap	s
T_{int}	Integration time	s
T_s	Sampling interval	s
\mathbf{w}	Weighting function	
W_{bank}	One-sided width of correlator bank	s
W_{CIR}	One-sided width of CIR	s
y	Received baseband signal	
$\tilde{\mathbf{z}}$	Complex correlator outputs	
z_{constr}	Constraining measurement	
α	Tuning parameter of Tukey window function	
β	Exponential base for the nonuniform correlator spacing	
$\Delta_c^{(l_c)}$	Correlator spacing between the $(l_c - 1)$ -th and the l_c -th correlator	s
Δ_{el}	Early-late spacing	s
$\Delta_h^{(l_h)}$	Channel tap spacing between $(l_h - 1)$ -th and l_h -th channel tap	s
η	Zero mean Gaussian noise of received baseband signal	
$\tilde{\boldsymbol{\eta}}_c$	Colored noise of correlator outputs	
λ	Carrier wavelength	m
σ_{constr}	STD of measurement noise of constraining measurement	
σ_η	STD of noise of received baseband signal	
$\sigma_{P,h}$	Initial STD of state estimate of channel coefficients	
$\sigma_{P,\tau}$	Initial STD of state estimate of LOS code delay	s
$\sigma_{P,\dot{\tau}}$	Initial STD of state estimate of LOS code Doppler	
$\sigma_{Q,h}$	STD for process noises of channel coefficients	
$\sigma_{Q,\dot{\tau}}$	STD for process noises of LOS code delay and Doppler	1/s
$\tau^{(0)}$	LOS code delay	s
$\dot{\tau}^{(0)}$	LOS code Doppler	
τ_{mul}	Multipath access delay	s
$\tau_{\text{err}}^{(0)}$	Tracking error	s
$\Phi_{s,s}(\tau)$	Autocorrelation function of s	

A continuous-time parameter or signal is indicated by the time variable t in parenthesis, e.g., $\tau^{(0)}(t)$ for the line-of-sight (LOS) code delay or $y(t)$ for the received baseband signal. Discrete-time parameters use the sampling index k as a subscript, e.g., $\tau_k^{(0)}$. The n -th sample of the k -th integration period of a discrete-time signal is indicated by the sample index n in brackets, e.g., $y_k[n]$. When stacking all N samples over the integration time T_{int} to a column vector, the vector notation, i.e., bold lowercase letters, is used with \mathbf{y}_k . Matrices are represented with bold uppercase letters, e.g., \mathbf{R} .

The signal and band indices i and j , respectively, indicate the corresponding signal and band to which a signal or parameter belongs in the index, e.g., $s_{j,i}$ for the pseudorandom noise (PRN) signal or $\tau_j^{(0)}$ for the LOS delay.

The estimate of a parameter is indicated using the hat notation as, e.g., $\hat{\tau}^{(0)}$ which is the estimate of the LOS code delay.

Kalman filter related variables

Symbol	Description	Unit of component
\mathbf{A}	Process matrix	
$\mathbf{f}(\mathbf{x}_k)$	Measurement model	
\mathbf{J}_f	Jacobian matrix of measurement model	
\mathbf{K}	Kalman gain	
N_{meas}	Number of measurements	
N_{st}	Number of state variables	
\mathbf{P}	State estimate covariance matrix	
\mathbf{Q}	Process noise covariance matrix	
\mathbf{R}	Measurement noise covariance matrix	
\mathbf{S}	Innovation matrix	
\mathbf{u}	Measurement noise	
\mathbf{v}	Process noise	
\mathbf{x}	State vector	
$\tilde{\mathbf{x}}$	State correction	
$\hat{\mathbf{x}}$	State estimate	
\mathbf{z}	Measurements	
$\hat{\mathbf{z}}$	Predicted measurements	

For the generic Kalman filter (KF), the state vector is dimensionless as the state parameters are assumed to be normed. The different KF configurations in Section 2.3, 4.1, 5.1, and 7.2 introduce the state vector units accordingly.

Vector tracking related variables

Symbol	Description	Unit of component
\vec{a}	LOS unit vector	
h_0	Allan variance coefficient	s
h_{-2}	Allan variance coefficient	1/s
l_s	Satellite index	

l_g	GNSS index	
N_{sat}	Number of GNSS satellites	
\vec{r}_{sat}	Satellite position vector	m
\vec{r}_{u}	User position vector	m
T_{PVT}	PVT interval time	s
t_{u}	User clock bias	s
\dot{t}_{u}	User clock drift	
\vec{v}_{sat}	Satellite velocity vector	m/s
\vec{v}_{u}	User velocity vector	m/s
x_{u}	User position in x-direction	m
\dot{x}_{u}	User velocity in x-direction	m/s
y_{u}	User position in y-direction	m
\dot{y}_{u}	User velocity in y-direction	m/s
z_{u}	User position in z-direction	m
\dot{z}_{u}	User velocity in z-direction	m/s
Δf	Carrier frequency discriminator output	Hz
Δf_{code}	Code NCO correction	
Δf_{carr}	Carrier frequency error	Hz
$\Delta \rho$	Code discriminator output	m
ρ	Pseudorange	m
$\dot{\rho}$	Pseudorange rate	m/s
$\hat{\rho}$	Predicted pseudorange	m
$\hat{\dot{\rho}}$	Predicted pseudorange rate	m/s
$\tilde{\rho}$	Pseudorange correction	m
$\tilde{\dot{\rho}}$	Pseudorange rate correction	m/s
σ_{acc}	STD for process noise of user position	m/s ²
σ_{DLL}	STD of noise of code discriminator output	m
σ_{FLL}	STD of noise of carrier frequency discriminator output	Hz
$\sigma_{\text{P, pos}}$	Initial STD of state estimate of user position	m
$\sigma_{\text{P, } t_{\text{u}}}$	Initial STD of state estimate of user clock bias	s
$\sigma_{\text{P, } \dot{t}_{\text{u}}}$	Initial STD of state estimate of user clock drift	
$\sigma_{\text{P, vel}}$	Initial STD of state estimate of user velocity	m/s
σ_{to}	STD of GGTO measurement noise	s
$\tilde{\tau}^{(0)}$	LOS code delay estimate correction	s

The arrow above a parameter is a vector notation that refers to geometrical vectors. Examples are the user position vector \vec{r}_{u} or the user velocity vector \vec{v}_{u} .

Ionospheric multipath mitigating EKF related variables

Symbol	Description	Unit of component
N_{comb}	Number of frequency band combinations	
n_e	Ionospheric TEC	TECU
\dot{n}_e	Ionospheric TEC rate	TECU/s
$z_{j_1, j_2, \text{g-free}}$	Geometric-free carrier range rate measurement	TECU/s
$z_{j_1, j_2, \text{i-free}}$	Ionosphere-free carrier range rate measurement	
α_1	Ionospheric TEC conversion factor	m^3/s^2
σ_{P, n_e}	Initial STD of ionospheric TEC	TECU
$\sigma_{\text{P}, \dot{n}_e}$	Initial STD of ionospheric TEC rate	TECU/s
$\sigma_{\text{P}, \tau_{\text{g}}}$	Initial STD of geometric LOS code delay	s
$\sigma_{\text{P}, \dot{\tau}_{\text{g}}}$	Initial STD of geometric LOS code Doppler	
$\sigma_{\text{Q}, \dot{\tau}_{\text{g}}}$	STD for process noises of geometric LOS code delay and Doppler	1/s
$\sigma_{\text{Q}, \dot{n}_e}$	STD for process noises of ionospheric TEC and ionospheric TEC rate	TECU/s ²
$\sigma_{\dot{\phi}}$	STD of noise of carrier range observable	s
$\sigma_{z_{j_1, j_2, \text{g-free}}}$	Measurement noise STD of geometric-free carrier range rate measurement	TECU/s
$\sigma_{z_{j_1, j_2, \text{i-free}}}$	Measurement noise STD of ionosphere-free carrier range rate measurement	
τ_{g}	Geometric LOS code delay	s
$\dot{\tau}_{\text{g}}$	Geometric LOS code Doppler	
ϕ	Carrier range observable	s
$\dot{\phi}$	Carrier range rate observable	
ϕ_{err}	Carrier range errors	s
ϕ_{g}	Geometric carrier range	s
$\dot{\phi}_{\text{g}}$	Geometric carrier rate range	

Array multipath mitigating EKF related variables

Symbol	Description	Unit of component
a	Steering vector	
j	Imaginary unit	
k	Wave vector	rad/m
N_{ant}	Number of antenna elements	
r	Antenna element index	
r	Antenna element position vector	

ϕ_{mul}	Multipath phase	◦
θ	Elevation angle	◦
φ	Azimuth angle	◦
θ_{a}	Elevation angle of provided steering vector	◦
φ_{a}	Azimuth angle of provided steering vector	◦

Miscellaneous

Symbol	Description	Unit of component
p	Integer number $\in \mathbb{Z}$, i.e., $\dots, -2, -1, 0, 1, 2, \dots$	
q	Natural number $\in \mathbb{N}$, i.e., $1, 2, 3, \dots$	
$\mathbf{0}_q$	Column vector of zeros with length q	
$\mathbf{1}_q$	Column vector of ones with length q	
\mathbf{I}_q	Identity matrix of dimension q	
$\delta(t)$	Dirac distribution	
$\text{sgn}(\bullet)$	Sign function	
$*$	Convolution operator	
$[\bullet]^*$	Complex conjugate	
$[\bullet]^T$	Transpose	
$[\bullet]^H$	Hermitian	
$\ \bullet\ $	Euclidean norm	
$\langle \bullet, \bullet \rangle$	Inner product	
\circ	Hadamard product	
$\mathcal{N}(\mu, \sigma^2)$	Normal distribution with mean μ and covariance σ^2	
$\text{Var}(\bullet)$	Computes variance of provided vector	

1 Introduction

1.1 Motivation

Since the development of the very first global navigation satellite system (GNSS), its performance and widespread use has come a long way. From being initially invented for military use only, it is nowadays impossible to imagine everyday life without it. Many critical infrastructures rely on GNSSs, e.g., for time synchronization in mobile telecommunication networks or power grids [Eur24]. Moreover, GNSSs are being used more and more in aeronautics, maritime and car navigation, as well as the navigation of autonomous vehicles. Under nominal conditions, a reliable and precise timing and position is already possible today. However, such conditions are often not encountered in the field. Usually the satellite signals reach the receiver distorted by environmental effects.

A major environmental effect is the multipath propagation. Objects in the closer vicinity of the receiver reflect the satellite signals, leading to additional delayed replicas at the receiver, superimposing with the direct line-of-sight (LOS) signal. If not considered in the receiver algorithm, it can cause position errors of up to multiple meters [Kos+10]; [vNee92a]; [Bre+97]. Correspondingly, relying on GNSS for safety-critical applications like autonomous cars or unmanned aerial vehicles is a challenging task, requiring additional countermeasures.

In addition, different atmospheric layers introduce a time, location, weather, and solar activity dependent effect on the signal propagation, namely the tropospheric and the ionospheric delay. While the first can be modeled quite reliably [Teu+17, Chapter 6], modeling for the latter can be more difficult, especially in regions of higher ionospheric activity as it can be found in equatorial or polar regions. With the most commonly used Klobuchar model [Klo87] only 50% of the ionospheric delay can be removed on average. As the ionospheric delay is a dispersive effect, it becomes observable for multi-frequency receivers and its dominating first-order effect can be eliminated using the ionosphere-free combination [Hof+01, Chapter 6]. Unfortunately, this linear combination amplifies other errors. These includes not only noise contributions [Mis+06, Chapter 5] but also multipath errors [Win00, Chapter 5] that reflect as erroneous pseudorange measurements in the individual signal bands. Thus, with the attempt to reduce ionospheric errors, one might end up with even larger errors due to multipath effects. Multipath propagation depicts therefore the major constraining factor in GNSS.

In the following, existing solutions to address the effects of multipath propagation in GNSS receivers are reviewed.

1.2 State of the Art

Multipath mitigation has been a research subject for a long time. Correspondingly, a large variety of approaches has been proposed. They differ strongly in complexity and effectiveness, based on the application and requirements they were designed for. An overview of the different categories of approaches to reduce the effect of multipath for GNSSs is given in Figure 1.1. Existing approaches are split into four main classes, i.e., sensor fusion, antenna, assisted signal processing, and stand-alone signal processing approaches.

Sensor fusion approaches reduce the effect of multipath by incorporating information from other independent sensors. Most commonly, one relies on acceleration measurements from an inertial measurement unit (IMU) [Par+96, Chapter 7]. While IMUs on their own are in general not a stable navigation system due to the inherent increase in dead reckoning errors [Kao91], they can provide accurate information about relative position changes over the short term. Therewith, they can be beneficial as an aiding for GNSS-based positioning to mitigate the errors of short-term multipath effects. Moreover, they allow to bridge short GNSS outages, reduce noise, and increase tolerance to dynamics [Teu+17, Chapter 28]. Similar to that, odometry sensors, such as wheel speed sensors (WSSs) [Ner+15], or magnetometers [Mei+07]; [Bar+12] can be used to provide additional information to the GNSS receiver. The fusion with imaging and other environmental sensors, such as optical [Suz+14] or infrared (IR) [Meg+09] fish eye cameras, or the use of light detection and ranging (LiDAR) systems [Mai+10] allows to capture the nearer receiver environment. This permits the exclusion of satellites that have currently blocked LOS paths, which would otherwise be potentially received via reflections, providing erroneous measurements for the position, velocity, and time (PVT) solution. Alternatively, one can use the images of the receiver environment to conduct a visual odometry [Sch+16]; [Cio+20]; [Lee+22]. The category of environmental sensors also includes barometers, which can be used to aid in particular the GNSS height estimates [Chi+20]. Obviously, multiple sensors can be fused simultaneously to further increase robustness [Hen+18]; [Chi+20]. Another field within the class of sensor fusion approaches is the exploitation of signals of opportunity (SOPs). Examples are the use of Wi-Fi [Bis+14] or cellular [Mor+16] signals to aid GNSS. With the considerable increase of low Earth orbit (LEO) satellites, those newly arising signals from space also gained attention as SOPs, also known as LEO position, navigation, and timing (PNT) [Pro+22]; [Kas+23].

With the class of *assisted signal processing* techniques, such as primarily 3D mapping techniques, the shape of buildings are incorporated in order to reduce the effect of multipath. Those techniques are particularly designed for urban environments. So called 3 dimensional building models (3DBMs) are used to predict the current signal propagation conditions so that satellite visibility and multipath propagation can be considered for the position estimation. The most straight forward approaches determine the currently visible satellites at the user position using ray tracing techniques. This allows to introduce a satellite masking in the PVT solution to exclude, or at least de-weight, satellites that are currently blocked [Piñ+11]; [Obs+12]; [Pey+13],



Figure 1.1: Overview of different classes of approaches to reduce effect of multipath.

similar to the sensor fusion approaches with fish eye cameras mentioned above. As the exclusion of measurements leads to a degraded dilution of precision (DOP), more sophisticated approaches instead use the ray tracing results to correct measurements obtained from blocked satellites and in addition to that also to remove multipath errors from available satellites received via multiple paths [Suz+13]; [Hsu+16]; [Zie17]. Naturally, this leads to a more computational demanding solution compared to the simple masking. A different approach is the so called shadow matching [Gro11]; [Wan+13]. Here, the position is found by comparing the predicted satellite visibility with the measured one. This results in particular in an improved cross-street accuracy which is generally poor in urban canyons. As the ray tracing results are highly position depending, one would typically rely on particle filters to reflect the uncertainty of the user position [Suz+12]; [Yoz+15]; [Suz16].

The use of specialized *antennas* allows to reject multipath signals even before they reach the GNSS receiver, contrary to the approaches above. A prominent example is the choke-ring antenna [Sci+09] which attenuates signals from lower elevations. It is therewith commonly used to eliminate ground reflections at reference stations where

the dimension and weight of the antenna is less crucial. In other applications, where multipath also impinges from higher elevations, choke-ring antennas are of limited use. In this case, antenna arrays in combination with spatial signal processing provide more adaptability. They enable the differentiation of interfering signals based on their spatial characteristics instead of being restricted to the time and frequency domain. Yet, this remains a challenging task due to the strong temporal correlation between LOS and multipath signals. Solutions for that typically involve spatial smoothing [Sha+85] in order to de-correlate the individual signal components. However, this procedure comes at the cost of reducing the effective array aperture and requires specific antenna geometries. More advanced solutions estimate the individual multipath direction of arrivals (DOAs) and actively suppress them [Sah+07]. This concept has been further extended to include the estimation of array specific parameters allowing for a more general application [Zor+20]. While solutions involving antenna arrays can be very powerful, they come along with an increased cost due to the more complex antenna design and required multichannel receiver architecture. The so called correlator beamforming [Gun+19] attempts to soften this additional hardware and processing burden while maintaining the spatial domain. It still relies on multiple antenna elements, however, a hardware radio frequency (RF) switch selects always just one antenna at a time to be fed to the single channel RF front end and GNSS receiver. The lower hardware and processing requirements come at the cost of a correspondingly overall performance degradation due to the limited temporal observation of each antenna element. With synthetic-aperture processing, the advantages of an antenna array can be achieved to some extent with only a single antenna element. Based on the principles of synthetic-aperture radars, a single moving antenna is used to coherently combine GNSS signals observed from different spatial locations [Bre+92]; [Pan+08]; [Pan+13]. To achieve the required long integration times of up to a few seconds, the navigation data bits have to be stripped or one needs to rely on data-free pilot signals. This allows to maximize the LOS power and at the same time mitigate multipaths, impinging from other DOAs due to their distinct Doppler signatures. This approach has been extended to the so called supercorrelator [Far+18]. The two main challenges of this kind of approaches are the need for accurate knowledge of the user clock drift and motion. While the first can be resolved with appropriate modeling or higher grade clocks, the latter is typically achieved with an IMU aiding. This concept has been combined with 3DBMs in [Gro+20] in order to further improve accuracy. Instead of rejecting multipath signals, the use of dual-polarized antennas follows an opposing approach. Since all major GNSSs broadcast right-hand circular polarization (RHCP) signals, the direct LOS signals reach the receiver likewise as RHCP signals. Nevertheless, also left-hand circular polarization (LHCP) GNSS signals can reach the receiver. The polarization direction change is caused by reflections. While these typically unwanted signals are suppressed with conventional RHCP GNSS antennas, their exploitation allows to gain information about the multipath conditions. A first experimental investigation was conducted by [Man+04]. [Jia+14] proposed to detect and exclude satellites affected by multipath propagation based on the LHCP component. Dual-polarized antennas were used in [Gro+10]; [Xie+17] to mitigate multipath. Spatial signal processing has

also been combined with dual-polarization [Bre+07]; [Foh+17].

The final class is named *stand-alone signal processing*. It aggregates approaches that maintain the conventional GNSS receiver setup consisting of a single antenna element, a front end, and an analog-to-digital converter (ADC). No additional sensors, prior knowledge, or assistance information such as 3DBMs are used. Thus, a comparable wide range of application is possible, without specific GNSS receiver requirements and independent of the availability of information about the operation environment. It is subdivided into three categories, detection, mitigation, and estimation. Table 1.1 provides an overview of existing solutions for the three categories.

1.2.1 Multipath Detection

For a simple multipath detection, signal quality monitoring (SQM) techniques [Mor+21, Chapter 10] can be used. They can detect signal anomalies and thus also reveal the distorting effects of multipath propagation. Identified satellites can then be weighted less in the PVT solution or excluded altogether. Examples for well-known metrics are the Delta or Ratio metrics [Phe01], the early late phase (ELP) [Mub+10b]; [Mub+10a], or the slope asymmetric metric (SAM) [Fra+13]. Receiver autonomous integrity monitoring (RAIM) techniques [Lee86]; [vGra+93] also attempt to detect erroneous satellite measurements. An overview can be found in [Par+96, Chapter 5]. They rely on exploiting the measurement redundancy when more than four satellites are available. By determining the PVT solution multiple times, whereby individual satellites are excluded in each case, faulty measurements can be revealed. While such approaches can be effective in moderate multipath environments where only individual satellites are affected, it quickly reaches its limits in more demanding environments.

1.2.2 Multipath Mitigation

This leads to the group of multipath mitigation techniques. Considerable efforts have been made to develop advanced correlator structures, that outperform the conventional early-late discriminators with respect to their multipath performance. The Narrow CorrelatorTM, proposed by [Van+92], depicts in this context the most straightforward one. It simply reduces the spacing between the early and late correlators, lowering the influence of multipaths onto the code tracking. The class of double-delta correlators (DDCs) augments the conventional early-late correlator structure for the code tracking by one additional correlator pair. The additional information allows the DDC techniques to outperform [Bra01]; [Irs+03] the Narrow CorrelatorTM, while maintaining a relatively low computational complexity. Different implementations have been proposed, such as the high-resolution correlator (HRC) [McG+99] or the Strobe Correlator [Gar+96]; [Gar+97]. Essentially, the DDCs narrow the effective correlation function. This can also be achieved with a modified reference waveform design, e.g., the gated correlator [Kan+98], or with the as superresolution named pre-

Table 1.1: Overview of existing stand-alone signal processing techniques for multipath propagation.

Category	Existing Techniques
Detection	<p>Signal quality monitoring (SQM) [Phe01]; [Mub+10b]; [Mub+10a]; [Fra+13] [Mor+21, Chapter 10]</p> <p>Receiver autonomous integrity monitoring (RAIM) [Par+96, Chapter 5]</p>
Mitigation	<p><i>Advanced correlator structures</i></p> <ul style="list-style-type: none"> • Narrow CorrelatorTM [Van+92] • High-resolution correlator (HRC) [McG+99] • Strobe correlator [Gar+96]; [Gar+97] • Gated correlator [Kan+98] • Superresolution [Wei98] • Early-late slope (ELS) technique [Tow+94] • Early1/early2 (e1/e2) technique [Van+97] • A-posteriori multipath estimation (APME) technique [Sle+01] <p>Vector tracking (VT) [Cop+80]</p> <p>Direct position estimation (DPE) [Clo+07a]</p>
Estimation	<p><i>Structured channel model</i></p> <p>Non-sequential estimation</p> <ul style="list-style-type: none"> • Multipath estimating delay locked loop (MEDLL) [vNee92b] [vNee+94]; [Tow+95] • Multipath mitigation technology (MMT) [Wei02] • Vision Correlator [Fen+05] • Space alternating generalized expectation-maximization (SAGE) algorithm [Ant+05]; [Clo+07b] • Fast iterative ML algorithm (FIMLA) [Sah+08]; [Lan+11] • Saarnisaari's method [Saa96] • Levenberg–Marquardt (LM) algorithm [Nun+07]; [Nun+08] • Sequential Maximum likelihood (ML) methods [Sah+09]; [Sok+16] • Selva's method [Sel04b]; [Sel04a] • Grid search approach [Bla+12] <p>Sequential estimation</p> <ul style="list-style-type: none"> • Particle Filtering [Len+08]; [Clo+09]; [Kra+10] • Turbo delay locked loop (DLL) [Dov+04] • Coupled amplitude delay locked loop (CADLL) [Che+11]; [Che+13] <p><i>Unstructured channel model</i></p> <ul style="list-style-type: none"> • Multipath distribution estimation [Enn+17]

correlation signal shaping filter [Wei97]; [Wei98]. The narrower correlation function also comes along with a smaller range over which the discriminator function provides non-zero values. This can result in loss of lock in lower carrier-to-noise density ratio (C/N_0) situations or highly dynamic scenarios [Mor+21, Chapter 15]. In addition to that, these techniques come at the cost of a poorer noise performance compared to the conventional early-late tracking [McG+99]; [Pra04]. Other solutions relying on additional correlators depict the early-late slope (ELS) technique [Tow+94], also known as the multipath elimination technique (MET), the early1/early2 (e1/e2) tracking [Van+97] using only two early correlators, and the a-posteriori multipath estimation (APME) [Sle+01] relying on an additional late correlator. An entirely different approach, but still in the category of multipath mitigation are vector tracking (VT) processing architectures [Spi+96, Chapter 7], initially proposed by [Cop+80]. Instead of tracking satellites individually, all satellite tracking loops are coupled and driven by a central filter, exploiting the redundancy of the measurements. Doing so mitigates the effect of individual multipaths [Luo+14]. This advanced processing structure can be very powerful, especially as it handles well frequent LOS blockages. However, since multipaths are not actively suppressed the remaining multipath error increases the more satellites are affected. The direct position estimation (DPE) [Clo+07a] takes the concept of the joint processing of all satellites from the VT architecture one step further. Instead of relying on the intermediate step of calculating the discriminator function, the DPE determines straight from the correlator outputs the position estimates. Obviously, no closed-form solution exists for this estimation problem [Mor+21, Chapter 21]. Implementations need to rely for example on Bayesian filtering [Clo+10]. This higher computational load is rewarded by a reduced position error in scenarios where conventional tracking-based receivers fail [Clo+17], especially when the PVT probability distribution is multi-modal [Dam21].

1.2.3 Multipath Estimation

In order to achieve a higher resilience against multipath propagation and the ability to maintain it when numerous satellites are affected, multipaths have to be actively taken into account and suppressed, leading to the category of parameter estimation techniques. Hereby, a signal model is used that considers for multipath propagation. The estimation relies usually on the outcome of a correlator bank, that is sampling the observed distorted correlation function. In this context, the correlation acts as a compression of the raw signal so that only the correlation result, is provided to the estimator [Sel04b]; [Boc+22]. Different types of channel models have been used in the past for the estimation. They can be categorized into structured and unstructured channel models.

With the *structured channel model*, the received signal is described as the superposition of the direct LOS signal with a finite number of multipaths. Each multipath component is a delayed, attenuated, and phase-shifted replica of the LOS. An estimator is then derived, to determine the delay, amplitude, and phase of each signal component [Pan10, Chapter 8]. The multipath estimating delay locked loop (MEDLL),

proposed by [vNee92b] and further investigated in [vNee+94]; [Tow+95], depicts a well-known approach in this field that aroused with its publication the interest in this area of research. It derives a maximum likelihood (ML) estimator to determine the signal parameters. Since no straightforward closed-form solution to the nonlinear ML problem exists, the multidimensional ML estimator is approximated iteratively by breaking it down into one-dimensional ones which are solved sequentially and iterated further. However, it remains a computational demanding task and further grows in complexity with the number of multipath signals taken into account. In order to lower the computational burden, many different variants thereof have been proposed in the past. A prominent example is the multipath mitigation technology (MMT) [Wei02], which introduced a reversible nonlinear transformation to simplify the solving of the ML problem. This concept of the MMT has been taken up and applied to the domain of chip transitions by [Fen+05], which led to the so called Vision Correlator. [Ant+05] proposed to approximate the ML problem using the iterative space alternating generalized expectation-maximization (SAGE) algorithm [Fes+94], which has been used before for communication systems [Fle+99]. This approach was further investigated by [Clo+07b]. Then, [Sah+08] proposed, based on [Sou+02], the fast iterative ML algorithm (FIMLA), where the computational burden is reduced by an efficient implementation of the Newton iterative likelihood-maximization method. An implementation in a standard tracking loop structure can be found in [Lan+11]. Apart from the already mentioned ones, a variety of other ML approaches were suggested such as Saarnisaari's method [Saa96], the use of the Levenberg–Marquardt (LM) algorithm [Nun+07]; [Nun+08], sequential ML methods [Sah+09]; [Sok+16], or Selva's method [Sel04b]; [Sel04a]. The latter reduced the computational complexity by an additional compressing of the correlator outputs. An analysis of its close-loop behavior can be found in [Len+06]. A general weakness of iterative solvers, as the ones mentioned above, is, that the convergence to the global optimum cannot be guaranteed. Measures were taken to reduce this risk, for example by running the solver multiple times with different initial values at the cost of additional computational load [Nun+08]. To eliminate convergence problems entirely, a closed-form solution is needed, as it has been achieved with the grid search approach from [Bla+12], where interpolation was used to subsequently increase resolution.

All the above mentioned approaches for multipath estimation are non-sequential solutions. They solve the channel model for each time step individually. As a result, the temporal correlation that radio propagation channels typically show is disregarded. Sequential estimators, on the other hand, exploit this temporal component in order to track individual multipaths over time. Examples are solutions based on the recursive Bayesian estimation, typically relying on particle filtering with Rao-Blackwellization to keep the complexity within limits [Len+08]; [Clo+09]; [Kra+10]. Also among the sequential estimators belongs the Turbo delay locked loop (DLL) [Dov+04] with its further development, the coupled amplitude delay locked loop (CADLL) [Che+11]; [Che+13]. Based on the same fundamental idea of a structured channel model, the individual signal paths are separated via several consecutive tracking units, where each unit tracks one signal path and subtracts it from the received

signal for the following units in the sense of an inference calculation. In order to avoid stability problems, one needs to ensure that not more tracking units are used than available signal paths exist.

This brings us to a common drawback of the solutions based on a structured channel model. The unknown number of currently present number of multipaths need to be estimated. This can be done with model order estimation techniques [Wax+85]. These are computational costly methods that typically rely on the Akaike information criterium (AIC) [Aka74] or the minimum descriptive length (MDL) criterion [Ris78]. For the MEDLL it has been proposed to increase the number of signal paths until the optimization problem is sufficiently well solved or to rely on a static number of multipaths for simplicity. Other approaches have developed their own likelihood ratio test [Sok+16]. Approaches based on particle filtering allow to estimate the number of paths as a hidden channel state variable [Len+08]; [Kra+10]. The CADLL implements the path estimation by monitoring the state of the individual tracking units in order to shut down or add one if needed. The accurate estimation of the number of signal paths is crucial. As already mentioned by [Mor+21, Chapter 22], an incorrect estimate results inevitable in model errors. At the same time, with a correct estimate, the model gain can be fully exploited. Correspondingly, with a structured channel model one operates on a fine line between model gain and model errors. Apart from these potential model mismatches, such a structured channel model also means that the computational load of the algorithms depends on the number of signal paths considered. The more multipaths need to be resolved, the more unknowns need to be estimated. In practice, one is limited to a handful of paths in order to remain feasible for a real-time implementation. Moreover, observability concerns arise for approaches relying on structured channel models. Individual signal paths become increasingly correlated with decreasing differences in signal delays and Dopplers. As a result, the estimates of the parameters of closely spaced signal paths are increasingly subject to noise to the point where the estimator can no longer provide reliable estimates. This is also known as the problem of noise amplification.

These problems can be resolved with an *unstructured channel model*. Instead of resolving individual signal paths, the multipath signal contribution is described as a statistical distribution. Therewith, a model order estimation is no longer required and the estimation problem comes down to determining the LOS delay and the parameters of the multipath distribution, independent of the actual number of multipaths. This also avoids the aforementioned observability concerns for closely spaced signals paths. Already [Sto+90] proposed the use of a random model instead of a deterministic description, though in the context of DOA estimation. The first mentioning in the field of time of arrival (TOA) estimation has been made by [Sou+02] without further pursuing it. In [Rib+07] and [Bia+12] such unstructured multipath models have been applied to mobile radio channels and ultra-wideband (UWB) signals, respectively. [Wen+15] proposed a simple rank-one model for a dual-polarization setup. A more general approach can be found in [Enn+17], where a wide-sense stationary uncorrelated scattering (WSSUS) model has been used. Such a multipath distribution estimation even allows for a backtracking of the LOS delay when it is

obscured. Naturally, the choice of the underlying multipath distribution is crucial. An inappropriate distribution will again lead to model errors, which can result in a poor performance. Yet, a certain degree of model robustness has been demonstrated in [Enn+17].

1.3 Research Questions

The previous section gave a broad overview of existing solutions for multipath propagation in GNSSs. A total of four main classes of approaches were identified. The focus was brought to the class of stand-alone signal processing techniques, that, in contrast to the remaining ones, does not require prior information about the operation environment, specialized antennas, or additional sensors to operate. It thus allows for a more universal application. Despite the large number of approaches existing in this field, certain gaps still remain.

In the category of parameter estimation techniques, existing solutions largely rely on a structured channel model that describes the received signal as a superposition of multiple delayed, attenuated, and phase-shifted signal replicas. The major drawback of this channel model is that it requires a model order estimation. This is not only a computationally intensive process, but can also lead to model errors if the number of paths is estimated incorrectly. In addition to that, observability limitations for closely spaced signal paths exist. The use of an unstructured channel model has been proposed, resolving these issues. It no longer relies on the knowledge of the number of individual signal paths and instead describes the multipath propagation statistically. This introduces the new model assumption that multipaths occur according to a certain statistical distribution, again posing a risk for model errors. In general it can be said that the more assumption are made about the radio propagation channel, the higher is the potential model gain. On the other hand, a more specific model increases the risk for model mismatches as no longer all scenarios might satisfy the assumptions made. A solution suitable for a general application must therefore make minimal assumptions about the radio propagation channel. In the category of multipath mitigation techniques, well-working solutions have been found that indeed introduce minimal assumptions, an example in this context is the HRC. However, their major drawback depict the inferior noise performance [McG+99]; [Pra04]. As the noise performance is a crucial parameter in basically all applications, the following first research question can be formulated:

1) How can a multipath mitigation solution be designed to make minimal assumptions about the radio propagation channel and remain competitive in terms of its noise performance?

Besides the model fidelity and noise concerns described above, complexity is another important factor. This is in particular crucial for the estimation techniques based on structured channel models. They require not only model order estimations, but also the multipath estimators themselves can be computational demanding. Moreover, the more signal paths are considered, the higher is the total computational

burden. Therewith, one is limited in practice to a handful of paths in order to remain feasible for a real-time implementation. The use of unstructured channel models resolved that as the estimation problem is brought down to the parameters of the multipath distribution, independent of the number of multipaths. An increased complexity is not only a drawback regarding a cost-effective implementation, it also tends to increase the burden for a certification for safety of life applications. Proving the integrity requirements can be very challenging for such advanced estimators, especially for the mentioned sequential estimators relying on particle filtering. This brings up the question, whether a solution based on a signal model with minimal assumptions remains competitive with respect to complexity concerns:

2) Can the complexity of such a general multipath mitigation technique be determined and what are the performance tradeoffs when it is brought to a reasonable level?

Having found such a general multipath mitigation technique of low complexity, it is of interest, whether its performance can be further improved by integrating it into existing advanced processing architectures, such as VT. They are known to improve not only the overall performance due to the joint processing of all satellites, but in particular also for the reliable handling of frequently blocked satellites. This brings up the question, to which extent a general multipath mitigation technique can benefit from such an architecture:

3) To what extent can the multipath mitigation performance of such an approach be improved with the joint processing of signals of multiple satellites?

The motivation in Section 1.1 has drawn attention to ionospheric effects as a second important error contributor, besides multipath propagation. While a multi-frequency receiver is theoretically able to largely eliminate ionospheric delays, this improvement comes along with the price of a substantially increased impact of multipath errors. This brings up the following research question:

4) To what extent can such an approach be extended to ionospheric delay estimation in multipath environments keeping impact of multipath errors low?

So far, the focus has been mainly on techniques from the stand-alone signal processing class. However, approaches from the remaining classes, see Figure 1.1, offer entirely new possibilities in terms of multipath suppression performance. This is due to the fact that additional sensors, environmental information, or antenna characteristics provide an inherent advantage over the stand-alone signal processing techniques. The use of multi-antenna systems is particularly noteworthy in this context. They enable the exploitation of the spatial domain, in contrast to a single antenna receiver, that is limited to the time and frequency domain. This raises the question, to which extent the multipath robustness of the general multipath mitigation technique can be enhanced under consideration of the spatial component:

5) Is it possible to further improve multipath robustness of this general approach with the help of multi antenna systems?

1.4 Outline

In order to answer the above defined research questions and to fill the identified gap, the thesis is structured as follows. Subsequent to this introduction, Chapter 2 derives the signal model and the proposed multipath mitigation algorithm. The signal model is defined in such a way that minimal assumptions were made about the radio propagation channel in order to address the first part of the first research question. Correspondingly, the proposed algorithm does not need to perform model order estimations as with structured channel models, nor are assumptions made over the multipath distribution as with unstructured channel models. Only the simple condition, that the LOS signal is the strongest signal path, had to be introduced. The required number of elementary arithmetic operations for this algorithm was derived as a complexity metric. This allows for a complexity comparison later on, addressing the second research question.

In Chapter 3, this multipath mitigation algorithm is analyzed extensively with synthetic GNSS signals. Thereby, the multipath robustness, its dynamic response, and the noise performance were demonstrated. The latter answers the second part of the first research question. In addition to that, performance tradeoffs are analyzed when reducing the overall complexity of the proposed approach, fulfilling the second research question. In order to set the obtained performance into perspective, comparisons are drawn to other multipath mitigation and estimation techniques.

The assumption made that the LOS signal is the strongest signal path is also common in conventional code tracking algorithms relying for example on the early minus late (EML) discriminator. However, especially in dense urban environments, this is not always fulfilled. The direct LOS path might be obstructed due to buildings or other objects. VT architectures with their joint processing of all satellites are known to be more resilient against such LOS blockages. The integration of the proposed multipath mitigation algorithm into VT processing architectures is therefore investigated in Chapter 4, addressing the third research question.

Chapter 5 examines the extension of the developed multipath mitigation algorithm to multiple frequencies. This has been done to allow for an ionospheric delay estimation instead of relying on models for that, targeting the fourth research question.

In Chapter 6, the proposed algorithm is then verified and analyzed with authentic GNSS signals from a GNSS signal generator as well as actual measurement data. This demonstrates its capabilities in different real-world environments. On top of that, the proposed integration into VT structures as well as the extension to multiple frequencies for the ionospheric delay estimation were also demonstrated.

Last but not least, the proposed solution is extended to the use of antenna array

systems in Chapter 7. The increased multipath robustness achieved is compared to existing beamforming techniques.

The conclusion of this thesis is given in Chapter 8.

2 Multi-Correlator-Based Multipath Mitigation

In this chapter a novel multi-correlator-based multipath mitigation is introduced. The multipath mitigation aims to reduce multipath errors in the code tracking of global navigation satellite system (GNSS) receivers. Therefore, a signal model is first of all derived below followed by a general Kalman filter (KF) description in Section 2.2. Subsequently, the proposed joint estimator is developed in Section 2.3.

2.1 Signal Model

A multi-frequency multi-signal GNSS signal model is derived in the following. The signal model originates from [Sie+23a] which in turn depicts an extension to [Ili+17] and [Ilt90]. Figure 2.1 schematically illustrates the signal processing chain from the signal generation in the satellite to the sampled baseband signal at the receiver. This representation depicts only a simplification with aspects, such as Doppler effects, missing. All elements in this chain are assumed to be ideal. Moreover, components that are not strictly necessary for the signal model derivation have been omitted, e.g., transmit and receive antennas and amplifiers. It is assumed that a GNSS satellite operates on N_{band} frequency bands, with $N_{\text{sig},j}$ different signals being broadcast in the j -th band. The i -th navigation data stream in the j -th band $d_{j,i}(t)$ is spread in frequency before transmission by a pseudorandom noise (PRN) sequence

$$\bar{s}_{j,i}(t) \equiv \bar{s}_{j,i}(t - pT_{\text{code},j,i}), \quad \forall p \in \mathbb{Z}, \quad j = 1, \dots, N_{\text{band}}, \quad i = 1, \dots, N_{\text{sig},j} \quad (2.1)$$

where $T_{\text{code},j,i}$ is the i -th code period in the j -th band. Each PRN code consists of individual chips with duration $T_{c,j}$. As all currently deployed civil GNSSs rely on the same chip duration within one band, $T_{c,j}$ is assumed to be equal for all $N_{\text{sig},j}$ signals of one band. Before the raw PRN code is used to spread the navigation message, it

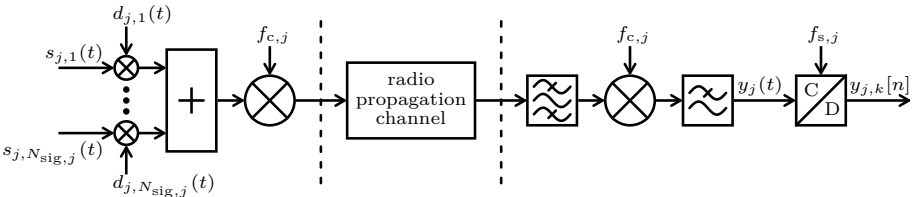


Figure 2.1: Block diagram of signal processing chain for the j -th band. The vertical dashed lines separate the three segments: signal generation in the satellite, radio propagation, and signal down-conversion and sampling in the receiver. The last element in the chain is a continues-to-discrete-time (C/D) converter.

is modulated itself with the sequence $m_{j,i}(t)$. The legacy Global Positioning System (GPS) L1 coarse/acquisition (C/A) code uses a binary phase-shift keying (BPSK) for this purpose, for which the modulating sequence is simply $m_{j,i}(t) = 1, \forall t \in \mathbb{R}$. Since the Galileo Open Service (OS) relies on binary offset carrier (BOC) modulation schemes, $m_{j,i}(t)$ is the corresponding sub-carrier signal. In addition to that, the individual chip sequences $\bar{s}_{j,i}(t)$ undergo a chip-shaping. This is modeled with the impulse response $g(t)$. The resulting modulated PRN signal is referred to as $s_{j,i}(t)$ with

$$s_{j,i}(t) = m_i(t)\bar{s}_{j,i}(t) * g(t), \quad (2.2)$$

where $*$ denotes the convolution operator. Without loss of generality, it is assumed that the impulse response $g(t)$ and the sub-carrier signal $m_{j,i}(t)$ are scaled in such a way that the following applies for the modulated signal:

$$\int_{T_{\text{code},j,i}} s_{j,i}(t) dt = 1. \quad (2.3)$$

The modulated navigation signals are then transmitted on their carrier frequency $f_{c,j}$ and correspondingly down-converted on the receiver side. The relative velocity between satellite and user introduces a Doppler shift. It leads to a frequency shift as well as a shortening or stretching of the received PRN signals. In order to maintain readability, this effect is omitted in this derivation. However, Subsection 2.3.6 will revisit this topic. The signal propagation path between satellite and user introduces a temporal delay $\tau_j^{(0)}(t)$, equal for all $N_{\text{sig},j}$ in one band. This is also referred to as the code delay. Further distortions are introduced by channel characteristics, such as multipath, or hardware imperfections. Assuming these can be modeled by a filtering operation, the complex received baseband signal of the j -th band can be expressed as

$$y_j(t) = \sum_{i=1}^{N_{\text{sig},j}} y_{j,i}(t) + \eta_j(t), \quad (2.4)$$

where

$$y_{j,i}(t) = \int_{-\infty}^{\infty} s_{j,i}(t - \tau - \tau_j^{(0)}(t)) d_{j,i}(t) h_j(t, \tau) d\tau. \quad (2.5)$$

The noise is modeled as an additive zero mean complex Gaussian noise $\eta_j(t) \sim \mathcal{N}(0, \sigma_{\eta_j}^2)$, as in [Teu+17, Chapter 14]. The channel characteristics are approximated by a time-varying tapped delay line channel model with

$$h_j(t, \tau) \approx \sum_{l_h = -L_{h,j}}^{L_{h,j}} h_j^{(l_h)}(t) \delta(\tau - T_{h,j}^{(l_h)}), \quad (2.6)$$

where $\delta(t)$ is the Dirac distribution, $h_j^{(l_h)}(t) \in \mathbb{C}$, $l_h = -L_{h,j}, \dots, L_{h,j}$ are the complex channel coefficients, and $T_{h,j}^{(l_h)} = \text{sgn}(l_h) \sum_{l=0}^{|l_h|} \Delta_{h,j}^{(l)}$, $\Delta_{h,j}^{(0)} = 0$ are the channel tap delays with the sign function

$$\text{sgn}(l_h) = \begin{cases} 0 & \text{for } l_h = 0 \\ l_h/|l_h| & \text{for } l_h \neq 0 \end{cases} \quad (2.7)$$

and the channel tap spacings $\Delta_{h,j}^{(l)}(t)$, $l > 0$. Thus, a total of $N_{\text{tap},j} = 2L_{h,j} + 1$ channel taps are placed, symmetrically distributed around the central tap $h_j^{(0)}$. Correspondingly, the channel impulse response (CIR) spans over $\pm W_{\text{CIR},j}$ with $W_{\text{CIR},j} = T_{h,j}^{(L_{h,j})}$. Moreover, it is equal for all $N_{\text{sig},j}$ as all signals propagate with the same carrier frequency $f_{c,j}$ along the same path. The channel coefficients $h_j^{(l_h)}(t)$ have the unit s^{-1} . In contrast to [Ilt90]; [Ili+17], we also allow channel coefficients with $l_h < 0$, despite the fact that GNSSs are causal systems. Before the first signal path, the CIR may contain pre-oscillations, which can only be described accurately with an acausal impulse response. For a better readability, we assume from now on without loss of generality that the navigation data bits are $d_{j,i}(t) = 1$, $\forall t \in \mathbb{R}$, so that we can omit them in the following expressions. It should be noted, however, that for the proposed algorithm introduced later on in Section 2.3, the data bits need to be estimated, see Subsection 2.3.4. The received baseband signal can then be expressed with

$$y_j(t) \approx \sum_{l_h=-L_{h,j}}^{L_{h,j}} h_j^{(l_h)}(t) \sum_{i=1}^{N_{\text{sig},j}} s_{j,i}(t - T_{h,j}^{(l_h)} - \tau_j^{(0)}(t)) + \eta(t). \quad (2.8)$$

Next, the baseband signal is brought to the discrete signal space by sampling it at $f_{s,j} = 1/T_{s,j} \geq 2B_j$, with B_j being the one-sided bandwidth of $y_j(t)$, fulfilling the Nyquist-Shannon sampling theorem. Therefore, we make the approximation of blockwise constant channel coefficients $h_{j,k}^{(l_h)} = h_j^{(l_h)}(kT_{\text{int}})$ and code delay $\tau_{j,k}^{(0)} = \tau_j^{(0)}(kT_{\text{int}})$ with $k = \lfloor t/T_{\text{int}} \rfloor$ and the integration time T_{int} . Doing so assumes that the channel coherence time is larger than T_{int} , which is a valid assumption for most applications. Moreover, without loss of generality, we limit T_{int} to common multiples of all $T_{\text{code},j,i}$. Therewith, the periodicity of all $s_{j,i}(t)$ is preserved over the integration time T_{int} , enabling a simpler mathematical notation in the following. This leads then, under consideration of the just mentioned periodicity, to the following sampled received baseband signal

$$\begin{aligned} y_{j,k}[n] &= y((kN_j + n)T_{s,j}) + \eta((kN_j + n)T_{s,j}), \quad k = 0, 1, \dots \\ &= \sum_{l_h=-L_{h,j}}^{L_{h,j}} h_{j,k}^{(l_h)} \sum_{i=1}^{N_{\text{sig},j}} s_{j,i}(nT_{s,j} - T_{h,j}^{(l_h)} - \tau_{j,k}^{(0)}) + \eta_j((kN_j + n)T_{s,j}) \end{aligned} \quad (2.9)$$

with $N_j = T_{\text{int}}/T_{s,j} \in \mathbb{Z}^+$. Without loss of generality, the sampling frequency $f_{s,j}$ is assumed to be chosen such that N_j is an integer. The sample index n is restricted to $n = 0, \dots, N_j - 1$. With the unrestricted time step index $k = 1, 2, \dots$, however, the

sampled signal representation in Equation (2.9) still covers the entire time domain. Each time step k , N_j samples are stacked to a column vector before further processing. The signal in matrix notation is then given by

$$\begin{aligned} \mathbf{y}_{j,k} &= [y_{j,k}[0], \dots, y_{j,k}[N_j - 1]]^\top \in \mathbb{C}^{N_j \times 1} \\ &= \sum_{l_h = -L_{h,j}}^{L_{h,j}} h_{j,k}^{(l_h)} \mathbf{s}_j(\tau_{j,k}^{(0)} + T_{h,j}^{(l_h)}) + \boldsymbol{\eta}_{j,k} \end{aligned} \quad (2.10)$$

with $[\cdot]^\top$ denoting the transpose of a matrix or vector. The noise vector and the vector of PRN signals are defined as follows:

$$\boldsymbol{\eta}_{j,k} = [\eta_{j,k}(kT_{\text{int}}), \eta_{j,k}(T_{s,j} + kT_{\text{int}}), \dots, \eta_{j,k}((N_j - 1)T_{s,j} + kT_{\text{int}})]^\top, \quad (2.11)$$

$$\mathbf{s}_j(\tau_{j,k}^{(0)}) = \sum_{i=1}^{N_{\text{sig},j}} \mathbf{s}_{j,i}(\tau_{j,k}^{(0)}) \in \mathbb{C}^{N_j \times 1}, \quad (2.12)$$

$$\mathbf{s}_{j,i}(\tau_{j,k}^{(0)}) = [s_{j,i}(-\tau_{j,k}^{(0)}), s_{j,i}(T_{s,j} - \tau_{j,k}^{(0)}), \dots, s_{j,i}((N_j - 1)T_{s,j} - \tau_{j,k}^{(0)})]^\top. \quad (2.13)$$

In GNSS receivers designed to simultaneously operate on multiple signals on the same carrier, the phase locked loop (PLL) can hold only one signal in phase. As not all signal components are necessarily in-phase, other signals may be left in quadrature in this process. To account for this in the signal model, the PRN signals $s_{j,i}(t)$ were defined as complex. Therewith, the received baseband signal is fully described.

2.2 Kalman Filtering Algorithm

In the following, a general description of a KF can be found on which the algorithm proposed in the next Section 2.3 is based on. Since the considered measurement models in this work are nonlinear, but the process models are linear, a combination of the linear KF and the nonlinear extended Kalman filter (EKF) [Bar+01, Chapter 10] is used. First of all, the state vector $\mathbf{x}_k \in \mathbb{R}^{N_{\text{st}} \times 1}$ with N_{st} states needs to be defined. This vector holds the parameters to be estimated and evolves over time according to the linear process model [Bar+01, Chapter 5]

$$\mathbf{x}_{k+1} = \mathbf{A}\mathbf{x}_k + \mathbf{v}_k, \quad (2.14)$$

with the process matrix $\mathbf{A} \in \mathbb{R}^{N_{\text{st}} \times 1}$ and the process noise $\mathbf{v}_k \sim \mathcal{N}(\mathbf{0}_{N_{\text{st}}}, \mathbf{Q})$, where $\mathbf{0}_q \in \mathbb{R}^{q \times 1}$ denotes a column vector of zeros. The filter processes each time step k the measurement vector $\mathbf{z}_k \in \mathbb{R}^{N_{\text{meas}} \times 1}$ which is related to the state vector through the measurement model with

$$\mathbf{z}_k = \mathbf{f}(\mathbf{x}_k) + \mathbf{u}_k, \quad (2.15)$$

where $\mathbf{u}_k \sim \mathcal{N}(\mathbf{0}_{N_{\text{meas}}}, \mathbf{R})$ is the measurement noise with the covariance matrix \mathbf{R} . With the process and measurement model defined, the EKF estimates the state vector

\mathbf{x}_k based on the measurements $\mathbf{z}_0, \dots, \mathbf{z}_k$ in the minimum mean square error (MMSE) sense [Bar+01, Chapter 10]. This is done in two steps. First, the state vector of the next time step k is predicted. Then, when the new measurement \mathbf{z}_k becomes available, the state prediction is updated. The two steps are explained in the following.

2.2.1 Prediction Step

In the prediction step, the state vector of the upcoming time step k is predicted based on the previous state estimate $\hat{\mathbf{x}}_{k-1|k-1}$ and the process model \mathbf{A} . As we have a linear process model, one can use the standard KF equations for that with [Bar+01, Chapter 5]

$$\hat{\mathbf{x}}_{k|k-1} = \mathbf{A}\hat{\mathbf{x}}_{k-1|k-1} \quad (2.16)$$

$$\mathbf{P}_{k|k-1} = \mathbf{A}\mathbf{P}_{k-1|k-1}\mathbf{A}^\top + \mathbf{Q}, \quad (2.17)$$

where \mathbf{P} is the covariance matrix of the estimated state vector $\hat{\mathbf{x}}$. The indexing notation $k|k-1$ indicates that the estimate at time step k is based on all measurements up to and including $k-1$. The prediction of the measurements are simply

$$\hat{\mathbf{z}}_{k|k-1} = \mathbf{f}(\hat{\mathbf{x}}_{k|k-1}). \quad (2.18)$$

As the KF is a recursive estimator, an initial state estimate $\hat{\mathbf{x}}_{-1|-1}$ with an initial state covariance $\mathbf{P}_{-1|-1}$ must be provided.

2.2.2 Update Step

Once the next measurement becomes available, the update step can be performed. It corrects the predicted state estimate $\hat{\mathbf{x}}_{k|k-1}$ with the new measurement vector \mathbf{z}_k . With the nonlinear measurement model from Equation (2.15), we need the full EKF equations with [Bar+01, Chapter 10]

$$\text{Innovation covariance} \quad \mathbf{S}_k = \mathbf{J}_{f,k}\mathbf{P}_{k|k-1}\mathbf{J}_{f,k}^\top + \mathbf{R}_k \quad (2.19)$$

$$\text{Kalman gain} \quad \mathbf{K}_k = \mathbf{P}_{k|k-1}\mathbf{J}_{f,k}^\top\mathbf{S}_k^{-1} \quad (2.20)$$

$$\text{State correction} \quad \tilde{\mathbf{x}}_{k|k} = \mathbf{K}_k(\mathbf{z}_k - \hat{\mathbf{z}}_{k|k-1}) \quad (2.21)$$

$$\text{Updated state estimate} \quad \hat{\mathbf{x}}_{k|k} = \hat{\mathbf{x}}_{k|k-1} + \tilde{\mathbf{x}}_{k|k} \quad (2.22)$$

$$\text{Updated state covariance} \quad \mathbf{P}_{k|k} = (\mathbf{I}_{N_{\text{st}}} - \mathbf{K}_k\mathbf{J}_{f,k})\mathbf{P}_{k|k-1}, \quad (2.23)$$

where $\mathbf{I}_q \in \mathbb{R}^{q \times q}$, $q \in \mathbb{N}$ denotes an identity matrix. The measurement model has been linearized at the current state estimate $\hat{\mathbf{x}}_{k|k-1}$ with the Jacobian matrix [Bar+01, Chapter 10]

$$\mathbf{J}_{f,k} = \left. \frac{d\mathbf{f}(\mathbf{x}_k)}{d\mathbf{x}_k} \right|_{\mathbf{x}_k = \hat{\mathbf{x}}_{k|k-1}}. \quad (2.24)$$

2.3 Multipath Mitigating Extended Kalman Filter

Based on the signal model derived in Section 2.1, a joint estimator is developed in the following. Its purpose is to replace the conventional delay locked loop (DLL) for the code tracking in a GNSS receiver with the advantage of an improved multipath suppression. This approach has been initially proposed by [Ilt90] and was later on taken up again by [Ili+17]; [Ili+18]. [Sie+21b]; [Sie+21c]; [Sie+21a]; [Sie+22b]; [Sie+23a]; [Sie+24] further pursued the development of this algorithm and conducted extensive testing in different multipath environments. The algorithm is referred to as the multipath mitigating EKF (MMEKF) in this work. We begin by introducing the required correlator bank, followed by the actual algorithm description in Subsection 2.3.2.

2.3.1 Correlator Bank

The number of samples N_j in $\mathbf{y}_{j,k}$ that accumulate at each time step k represents a challenge for further processing. Therefore, an efficient representation of the received signal is needed without loss of information. We use banks of signal-matched correlators that project the observed signal onto a much smaller space, so that subsequent computations are significantly simplified. Each correlator bank for each of the $N_{\text{sig},j}$ superimposed signals per satellite band is defined as

$$\mathbf{C}_{j,i} \left(\hat{\tau}_{j,k}^{(0)} \right) = \begin{bmatrix} \mathbf{s}_{j,i}^\top (\hat{\tau}_{j,k}^{(0)} - T_{c,j}^{(L_{c,j})}) \\ \vdots \\ \mathbf{s}_{j,i}^\top (\hat{\tau}_{j,k}^{(0)} - T_{c,j}^{(1)}) \\ \mathbf{s}_{j,i}^\top (\hat{\tau}_{j,k}^{(0)} - T_{c,j}^{(0)}) \\ \vdots \\ \mathbf{s}_{j,i}^\top (\hat{\tau}_{j,k}^{(0)} - T_{c,j}^{(-L_{c,j})}) \end{bmatrix}^\top \in \mathbb{C}^{N_j \times N_{\text{corr},j}} \quad (2.25)$$

with the correlator positions $T_{c,j}^{(l_c)} = \text{sgn}(l_c) \sum_{l=0}^{|l_c|} \Delta_{c,j}^{(l)}$, $l_c = -L_{c,j}, \dots, L_{c,j}$, $\Delta_{c,j}^{(0)} = 0$. In total, $N_{\text{corr},j} = 2L_{c,j} + 1$ signal-matched correlators are placed symmetrically and equidistantly within $\pm W_{\text{bank},j}$ around the prompt with $W_{\text{bank},j} = T_{c,j}^{(L_{c,j})}$. The hat notation indicates here and in the following the estimate of a parameter. The Nyquist condition determines the maximal correlator spacing in the bank with $\max_{1 \leq l \leq L_{c,j}} \Delta_{c,j}^{(l)} \leq 1/(2B_j)$. Going below this threshold, i.e., conducting an oversampling, is not associated with an information gain as the correlator outputs become increasingly correlated. The correlation with the received signal results then in

$$\begin{aligned} \tilde{\mathbf{z}}_{j,i,k} &= \mathbf{C}_{j,i}^H \left(\hat{\tau}_{j,k}^{(0)} \right) \mathbf{y}_{j,k} \in \mathbb{C}^{N_{\text{corr},j} \times 1} \\ &= \sum_{l_h=-L_{h,j}}^{L_{h,j}} h_{j,k}^{(l_h)} \mathbf{C}_{j,i}^H \left(\hat{\tau}_{j,k}^{(0)} \right) \mathbf{s}_{j,i}(\tau_{j,k}^{(0)} + T_{h,j}^{(l_h)}) + \tilde{\boldsymbol{\eta}}_{k,\mathbf{C}_{j,i}}. \end{aligned} \quad (2.26)$$

The conjugate transpose of a matrix is denoted by $[\cdot]^H$. Since the different PRN codes are largely orthogonal to each other, cross-correlation components have been neglected. The correlation colored the originally white noise $\boldsymbol{\eta}_{j,k}$ and led to $\tilde{\boldsymbol{\eta}}_{k,C,j,i} \in \mathbb{C}^{N_{\text{corr},j} \times 1}$ with covariance matrix [Mis+06, Chapter 10]

$$\mathbf{R}_{\tilde{\boldsymbol{\eta}}_{C,j,i}} = \sigma_{\tilde{\eta}_j}^2 \begin{bmatrix} \Phi_{s_{j,i}s_{j,i}}(0) & \cdots & \Phi_{s_{j,i}s_{j,i}}(2T_{c,j}^{(L_{c,j})}) \\ \vdots & \ddots & \vdots \\ \Phi_{s_{j,i}s_{j,i}}(2T_{c,j}^{(L_{c,j})}) & \cdots & \Phi_{s_{j,i}s_{j,i}}(0) \end{bmatrix} \in \mathbb{R}^{N_{\text{corr},j} \times N_{\text{corr},j}}, \quad (2.27)$$

where

$$\Phi_{s_{j,i}s_{j,i}}(\tau) = \int_{T_{\text{int}}} s_{j,i}^*(t) s_{j,i}(t + \tau) dt \quad (2.28)$$

is the autocorrelation function of the i -th PRN code. The asterisk indicates the complex conjugate. Now that the correlation step is fully defined, the actual algorithm can be described.

2.3.2 Joint Estimation of Code Delay and Channel Impulse Response

Based on the signal model derived above, an EKF is developed in the following in order to jointly estimate the code delay $\tau_k^{(0)}$ as well as the channel coefficients $h_k^{(l_h)}$. The consideration of the CIR aims to provide a higher resilience against multipath propagation. Although, the signal model and correlator bank from above are defined in the most general case, including multiple frequencies, the derived EKF in the following operates only on a single frequency. For the multi-frequency case, see Chapter 5. Correspondingly, the band index j has been omitted to improve the readability. A general description of an EKF has been provided already in Section 2.2. We define the state vector as

$$\mathbf{x}_k = \left[\tau_k^{(0)}, \dot{\tau}_k^{(0)}, \text{Re}(\tilde{\mathbf{h}}_k^T), \text{Im}(\tilde{\mathbf{h}}_k^T) \right]^T \in \mathbb{R}^{N_{\text{st}} \times 1} \quad (2.29)$$

with

$$\tilde{\mathbf{h}}_k = \left[h_k^{(-L_h)}, \dots, h_k^{(L_h)} \right]^T \in \mathbb{C}^{N_{\text{tap}} \times 1}, \quad (2.30)$$

holding the $N_{\text{st}} = 4(L_h + 1)$ unknown parameters. The operators $\text{Re}(\cdot)$ and $\text{Im}(\cdot)$ take the real and imaginary part of a complex number, respectively. In contrast to earlier publications like [Ilt90]; [Ili+17], the state vector has been augmented by the code Doppler $\dot{\tau}_k^{(0)}$ as in [Sie+21a]. This enables the operation of the proposed EKF without carrier-aiding – if desired. Moreover, the complex channel coefficients $h_k^{(l_h)}$ were split up into real and imaginary part to keep the state vector real-valued, as initially proposed by [Sie+21b]. This is required to prevent complex values for the real-valued parameters code delay $\tau_k^{(0)}$ and Doppler $\dot{\tau}_k^{(0)}$. In order to ensure the observability of the model, the channel tap spacing must equal the correlator spacing,

thus $\Delta_h^{(l)} = \Delta_c^{(l)}$, $\forall l \in \mathbb{N}$, and the CIR width must not exceed the correlator bank width with $W_{\text{CIR}} \leq W_{\text{bank}}$. We set $W_{\text{CIR}} = W_{\text{bank}}$ to not artificially limit the degrees of freedom of the KF. It follows that $N_{\text{tap}} = N_{\text{corr}}$. For the process model, see Equation (2.14), we set the process matrix to [Bar+01, Chapter 6]

$$\mathbf{A} = \text{diag} \left(\begin{bmatrix} 1 & T_{\text{int}} \\ 0 & 1 \end{bmatrix}, \mathbf{I}_{N_{\text{st}}-2} \right) \in \mathbb{R}^{N_{\text{st}} \times N_{\text{st}}}. \quad (2.31)$$

The process model predicts the code delay and Doppler according to a first order model. Furthermore, we assume that the channel coefficients follow, independent of that, a random walk model. Accordingly, the process noise covariance matrix is given by [Bar+01, Chapter 6]

$$\mathbf{Q} = \text{diag} \left(\sigma_{\dot{Q},\ddot{r}}^2 \begin{bmatrix} T_{\text{int}}^4/4 & T_{\text{int}}^3/2 \\ T_{\text{int}}^3/2 & T_{\text{int}}^2 \end{bmatrix}, \sigma_{\dot{Q},h}^2 \mathbf{I}_{N_{\text{st}}-2} \right) \in \mathbb{R}^{N_{\text{st}} \times N_{\text{st}}}. \quad (2.32)$$

The interdependence of CIR and code delay presents an ambiguity for the EKF. A too small code delay can be compensated by a CIR where the line-of-sight (LOS) path is represented in a later channel tap and vice versa.

Therefore, an additional optimization criterion is required to resolve this ambiguity. Since the LOS path is usually the strongest signal path [Ste+04], this is an obvious tracking criterion. Combining the estimation of the impulse response based on the correlator outputs with the condition that the LOS path is the strongest signal path yields an unambiguous optimization problem. In order to implement this second condition criteria, we developed a constraining measurement for the EKF, as first proposed by the author in [Sie+21b]. The constraining measurement is defined as

$$z_{k,\text{constr}} = \frac{\frac{1}{N_{\text{tap}}-1} \sum_{l_h=-L_h, l_h \neq 0}^{L_h} |h_k^{(l_h)}|^2}{|h_k^{(0)}|^2}. \quad (2.33)$$

The constraining measurement is measured as $z_{k,\text{constr}} = 0$, $\forall k$ and provided to the MMEKF alongside the correlator outputs as a conventional measurement with the measurement noise variance σ_{constr}^2 . For the measurement prediction, the constraining measurement is simply composed of the latest state estimates, as for any other measurement. Setting $z_{k,\text{constr}} = 0$, $\forall k$ imposes the maximization of the signal power at the central channel tap $h_k^{(0)}$ while minimizing the remaining non-line-of-sight (NLOS) taps. The constraining measurement introduces therewith the additional optimization criteria that the LOS is the strongest signal path and inevitably forces, if σ_{constr}^2 is set to a sufficiently small value, the joint estimator to shift the local replicas until the maximal signal power is obtained in the central channel tap $h_k^{(0)}$. Using the absolute value for the maximization, instead of taking, for example, only the real part where one would ideally find the LOS signal power, has the advantage that the carrier tracking does not necessarily need to be in lock. Especially in challenging multipath environments, the carrier tracking, typically implemented with a PLL, can

temporarily loose lock with the LOS signal, leading to cycle slips. Carrier phase errors reflect as an overall phase offset in the estimated CIR taps $h_k^{(l)}$ with an accordingly increasing imaginary part of $h_k^{(0)}$. With the constraint considering only the absolute values of the channel taps, phase offsets have no effect. Moreover, sudden carrier phase changes, as they appear with cycle slips, induce a transient process in which the EKF adjusts its CIR estimate, which might also affect channel tap amplitudes. However, this does not have a lasting effect on the code delay estimate. With the measurement variance σ_{constr}^2 one determines the tightness of the constraint. The choice of σ_{constr}^2 is a tradeoff between distorting the CIR estimate in favor of the LOS amplitude and, with a too loose constraint, letting the LOS drift off the central channel tap $h_k^{(0)}$, potentially causing the EKF to diverge. The measurement model of the EKF, see Equation (2.15), consists of the just now introduced constraining measurement as well as the post-correlation signal model from Equation (2.26) and can then be summarized as

$$\mathbf{z}_k = \left[\mathbf{z}_{1,k}^\top, \dots, \mathbf{z}_{N_{\text{sig}},k}^\top, z_{k,\text{constr}} \right]^\top = \mathbf{f}(\mathbf{x}_k) \in \mathbb{R}^{N_{\text{meas}} \times 1} \quad (2.34)$$

with

$$\mathbf{z}_{i,k} = [\text{Re}(\tilde{\mathbf{z}}_{i,k}^\top), \text{Im}(\tilde{\mathbf{z}}_{i,k}^\top)]^\top \in \mathbb{R}^{2N_{\text{corr}} \times 1}, \quad (2.35)$$

where $N_{\text{meas}} = 2N_{\text{corr}}N_{\text{sig}} + 1$. Similar to the state vector, the complex measurements were also decomposed into their real and imaginary part. This is a necessary measure to keep the whole EKF and with that the state vector \mathbf{x}_k real-valued. The signal model takes the radio propagation channel into account with the help of a CIR. Since in general $W_{\text{CIR}} \ll T_{\text{code},i}/2$ applies, this is only an approximation and multipaths with delays $> W_{\text{CIR}}$ are not considered, see Equation (2.8). In particular the outer correlators point out this shortcoming of the signal model as they pick up the correlation triangles of multipaths with delays $W_{\text{bank}} < \tau < W_{\text{bank}} + T_c$ that still partially extend into the correlator bank, where T_c is the PRN code chip duration. The obtained correlation result cannot be accurately reproduced with the signal model. This modeling mismatch effectively reflects as an increased observed measurement noise level of affected correlators. In order to account for that, the measurement noise covariance matrix of the correlator outputs from Equation (2.27) need to be scaled. While the measurement variance of the central correlator can remain untouched, the variances of outer correlators need to increase with increasing distance to the central correlator. In [Sie+23a], a scaling function has therefore been proposed with

$$\mathbf{R}_{\mathbf{w}\tilde{\eta}_{c_i}} = \mathbf{w}^\top \mathbf{w} \circ \mathbf{R}_{\tilde{\eta}_{c_i}}. \quad (2.36)$$

The notation \circ depicts the Hadamard product. The weighting function \mathbf{w} is defined as a diagonal matrix

$$\mathbf{w} = \text{diag} \left(f_T^{-1}(T_c^{(-L_c)}), \dots, f_T^{-1}(T_c^{(0)}), \dots, f_T^{-1}(T_c^{(L_c)}) \right) \in \mathbb{R}^{N_{\text{corr}} \times N_{\text{corr}}}, \quad (2.37)$$

which relies on the shape of the well-established Tukey window [Pra14, Chapter 3]

$$f_T(\tau) = \begin{cases} 1, & |\tau| < (1 - \alpha)W_T, \\ \frac{1}{2} + \frac{1}{2} \cos\left(\frac{\pi}{\alpha} \left(\frac{|\tau|}{W_T} + \alpha - 1\right)\right), & (1 - \alpha)W_T \leq |\tau| \leq W_T, \\ 0, & |\tau| > W_T. \end{cases} \quad (2.38)$$

We set $W_T = W_{\text{bank}} + \Delta_c^{(1)}$ to ensure that $f_T(\tau) \neq 0$, $\forall \tau \in [T_c^{(-L_c)}, T_c^{(L_c)}]$. The weighting function \mathbf{w} relies on a window function, as it allows for the required scaling, i.e., an increased scaling with increasing distance to the central correlator. The Tukey window is particularly suitable, as it conveniently allows with its tuning parameter $0 \leq \alpha \leq 1$ to choose between no scaling, i.e., $\alpha = 0$, and a Hann window shaped one with $\alpha = 1$. The entire measurement noise covariance matrix of the EKF is then given by the following block diagonal matrix

$$\mathbf{R} = \text{diag}\left(\mathbf{R}_{\mathbf{w}\eta_{C_1}}, \dots, \mathbf{R}_{\mathbf{w}\eta_{C_{N_{\text{sig}}}}}, \sigma_{\text{constr}}^2\right) \in \mathbb{R}^{N_{\text{meas}} \times N_{\text{meas}}}, \quad (2.39)$$

where

$$\mathbf{R}_{\mathbf{w}\eta_{C_i}} = \text{diag}\left(\mathbf{R}_{\mathbf{w}\bar{\eta}_{C_i}}/2, \mathbf{R}_{\mathbf{w}\bar{\eta}_{C_i}}/2\right) \in \mathbb{R}^{2N_{\text{corr}} \times 2N_{\text{corr}}}. \quad (2.40)$$

Having the process and measurement model fully defined, the EKF can be applied by providing an initial state estimate $\hat{\mathbf{x}}_{-1|-1}$ and an initial state covariance matrix

$$\mathbf{P}_{-1|-1} = \text{diag}\left(\sigma_{P,\tau}^2, \sigma_{P,\dot{\tau}}^2, \sigma_{P,h}^2, \mathbf{I}_{N_{\text{st}}-2}\right) \in \mathbb{R}^{N_{\text{st}} \times N_{\text{st}}} \quad (2.41)$$

to iteratively estimate the state vector, as explain in Subsection 2.2.1 and Subsection 2.2.2. For the initial code delay estimate $\hat{\tau}_{-1|-1}^{(0)}$ it is crucial, that it approximately matches the actual LOS delay. Since the constraining measurement expects the LOS on the central channel tap, convergence cannot be guaranteed if an initial code delay estimation would be off by multiple channel tap spacings. The Jacobian matrix from Equation (2.24) for the measurement model from Equation (2.34) results in

$$\begin{aligned} \mathbf{J}_{f,k} &= \left. \frac{d\mathbf{f}(\mathbf{x}_k)}{d\mathbf{x}_k} \right|_{\mathbf{x}_k = \hat{\mathbf{x}}_{k|k-1}} \\ &= \left[\frac{\partial \mathbf{f}(\mathbf{x}_k)}{\partial \tau_k^{(0)}} \quad \frac{\partial \mathbf{f}(\mathbf{x}_k)}{\partial \dot{\tau}_k^{(0)}} \quad \frac{\partial \mathbf{f}(\mathbf{x}_k)}{\partial \text{Re}(\hat{\mathbf{h}}_k)} \quad \frac{\partial \mathbf{f}(\mathbf{x}_k)}{\partial \text{Im}(\hat{\mathbf{h}}_k)} \right] \bigg|_{\mathbf{x}_k = \hat{\mathbf{x}}_{k|k-1}} \in \mathbb{R}^{N_{\text{meas}} \times N_{\text{st}}}. \end{aligned} \quad (2.42)$$

The individual partial derivatives can be found in Appendix A. With the assumption that the code delay estimate $\hat{\tau}_k^{(0)}$ is close to the actual code delay $\tau_k^{(0)}$, the following

approximation to the measurement model from Equation (2.34) can be made

$$\begin{aligned}
 \tilde{\mathbf{z}}_{i,k} &= \sum_{l_h=-L_h}^{L_h} h_k^{(l_h)} \mathbf{C}_i^H(0) \mathbf{s}_i(\tau_k^{(0)} - \hat{\tau}_k^{(0)} + T_h^{(l_h)}) + \tilde{\boldsymbol{\eta}}_{k,\mathbf{C}_i} \\
 &\approx \sum_{l_h=-L_h}^{L_h} h_k^{(l_h)} \mathbf{C}_i^H(0) \mathbf{s}_i(T_h^{(l_h)}) + \boldsymbol{\eta}_{k,\mathbf{C}_i} \\
 &= \sum_{l_h=-L_h}^{L_h} h_k^{(l_h)} \begin{bmatrix} \Phi_{\mathbf{s}_i \mathbf{s}_i}(T_h^{(l_h)} + T_c^{(L_c)}) \\ \vdots \\ \Phi_{\mathbf{s}_i \mathbf{s}_i}(T_h^{(l_h)} + T_c^{(-L_c)}) \end{bmatrix} + \tilde{\boldsymbol{\eta}}_{k,\mathbf{C}_i}. \tag{2.43}
 \end{aligned}$$

The first transformation is possible due to the circularity of the PRN signals \mathbf{s}_i and with that, the correlator bank \mathbf{C}_i . Afterwards, we have approximated $\tau_k^{(0)}$ and $\hat{\tau}_k^{(0)}$ to be equal. The resulting vector of autocorrelation functions in the final expression is time-invariant and thus, can be precomputed in an initialization phase, reducing load during runtime.

Therewith, the proposed MMEKF in its basic form has been described. With the underlying signal model from Section 2.1, minimal assumptions were made regarding the radio propagation channel. It is only assumed, that the LOS is the strongest signal path, which is a valid assumption in most applications. This general approach has the advantage, that no computational demanding model order estimations are required to determine the currently present number of signal paths, as it is the case with structured channel models, as, e.g., the multipath estimating delay locked loop (MEDLL) [vNee92b]. This fulfills the first part of the first research question stated in Section 1.3. The second part of this questions regarding its noise performance will be addressed in the next chapter under Section 3.4. Before that, the complexity of this algorithm will be derived in the following, targeting the second formulated research question.

2.3.3 Analysis of Computational Complexity

Computational complexity is an important factor in basically all applications. Accordingly, the second research question, formulated in Section 1.3, specifically targets this aspect, which will be addressed in the following. Compared to a conventional DLL-based GNSS receiver with a simple early minus late (EML) discriminator, the MMEKF requires the use of correlator banks and a joint estimator such as an EKF to achieve its multipath mitigation. The additional load due to a higher number of correlators is easily determined. It simply scales linearly with the number of correlators. On the other hand, the added complexity introduced by the EKF is less straightforward to assess and is therefore considered separately in the following. In order to quantify the additional computational effort, we rely on the required number of elementary arithmetic operations as a complexity metric. The otherwise frequently used Big O notation would be inappropriate in this context as the dimension of the

problem scales with the number of correlators and is therefore always comparable small. For the EKF derived above, the number of operations required for each step are listed in Table 2.1. It shall be noted that the number of operations in the table are for the case with $N_{\text{sig}} = 1$ tracked signals per satellite band. Moreover, we assumed that the matrix inversion, required for the Kalman gain computation in Equation (2.20), was implemented with the Gauss-Jordan elimination [Far88, Chapter 1]. Appendix D derives the required number of operations for this approach separately. A lower number of operations can be achieved with, for example, a Cholesky decomposition approach [Ben24]. The complexity assessment made here, relying on the more complex Gauss-Jordan elimination, depicts therewith an upper bound.

It is apparent from Table 2.1, that the number of operations, and therewith the overall complexity, is highly dependent on the number of correlator outputs N_{corr} . The more correlators are available, the more measurements N_{meas} need to be processed. In addition to that, a higher number of channel coefficients N_{tap} for the CIR need to be estimated. Both leads to larger vectors and matrices for the prediction and update step, see Subsection 2.2.1 and 2.2.2.

The complexity of the proposed MMEKF has therewith been quantified, answering the first part of the second research question. The second part of this question targeted the performance tradeoffs made when the complexity is reduced. This has been investigated in [Sie+23b] before, who has first mentioned the direct relationship between the computational complexity of the MMEKF and the number of correlators. Earlier publications, such as [Sie+21b]; [Sie+21a], have not considered complexity concerns and simply relied on correlator banks spanning across the entire correlation triangle, uniformly sampling the correlation function, i.e., with an equal correlator spacing $\Delta_c^{(l)} = \Delta_c^{(l+1)}$, $\forall l > 0$. In [Sie+23b], different approaches to lower the number of correlators have been proposed. In [Sie+23b], different approaches to lower the number of correlators have been proposed. They are introduced in the following. The multipath mitigation performance tradeoffs made with these complexity reductions are analyzed in Subsection 3.2.2 of the following Chapter 3. Moreover, Subsection 3.2.1 compares the complexity of the proposed MMEKF with other well-known approaches.

2.3.3.1 Uniform Sampling With Reduced Correlator Bank Width

The most straight forward way to lower the number of correlators is to simply reduce the width of the correlator bank W_{bank} while maintaining the equal spacing between the correlators $\Delta_c^{(l)} = \Delta_c^{(l+1)}$, $\forall l > 0$. This is a reasonable approach, since the goal is to distinguish between the LOS and multipaths. The resolution of far away multipaths is not necessarily of interest. A drawback of this approach is, that a narrower correlator bank intensifies the approximation made in the signal model by assuming finite CIR widths. In the following chapter, Subsection 3.2.2.1 analyses this tradeoff with respect to the multipath mitigation performance.

Table 2.1: Number of elementary arithmetic operations for the MMEKF.

	Addition	Subtraction	Multiplication	Division
State prediction (2.16)	1	0	1	0
State covariance prediction (2.17)	$6N_{\text{corr}} + 6$	0	$4N_{\text{corr}} + 4$	0
Measurement prediction (2.18)	$2N_{\text{corr}}^2 + 2N_{\text{corr}} - 4$	N_{corr}^2	$4N_{\text{corr}}^2 + 2N_{\text{corr}}$	1
Jacobian matrix (2.42)	$2N_{\text{corr}}^2 + 8N_{\text{corr}} - 3$	N_{corr}^2	$4N_{\text{corr}}^2 + 10N_{\text{corr}}$	$2N_{\text{corr}} + 2$
Innovation matrix (2.19)	$16N_{\text{corr}}^3 + 28N_{\text{corr}}^2 + 16N_{\text{corr}} + 3$	0	$16N_{\text{corr}}^3 + 32N_{\text{corr}}^2 + 26N_{\text{corr}} + 6$	0
Kalman gain (2.20)	$16N_{\text{corr}}^3 + 28N_{\text{corr}}^2 + 14N_{\text{corr}} + 2$	$8N_{\text{corr}}^3 + 4N_{\text{corr}}^2 + 2N_{\text{corr}}$	$24N_{\text{corr}}^3 + 38N_{\text{corr}}^2 + 25N_{\text{corr}} + 6$	$8N_{\text{corr}}^2 + 6N_{\text{corr}} + 1$
State update (2.22)	$4N_{\text{corr}}^2 + 8N_{\text{corr}} + 4$	$2N_{\text{corr}} + 2$	$4N_{\text{corr}}^2 + 6N_{\text{corr}} + 2$	0
State covariance update (2.23)	$16N_{\text{corr}}^3 + 36N_{\text{corr}}^2 + 24N_{\text{corr}} + 4$	$4N_{\text{corr}}^2 + 8N_{\text{corr}} + 4$	$8N_{\text{corr}}^2 + 14N_{\text{corr}} + 6$	0
Total	$48N_{\text{corr}}^3 + 100N_{\text{corr}}^2 + 78N_{\text{corr}} + 12$	$8N_{\text{corr}}^3 + 12N_{\text{corr}}^2 + 12N_{\text{corr}} + 6$	$40N_{\text{corr}}^3 + 90N_{\text{corr}}^2 + 87N_{\text{corr}} + 24$	$N_{\text{corr}}^2 + 8N_{\text{corr}} + 4$

2.3.3.2 Nonuniform Sampling

Another approach to reduce the total number of correlators relies on nonuniformly distributed correlators. The underlying idea is that one maintains a high correlator density around the LOS and let the spacing increase for outer correlators. A nonuniform correlator spacing has been parameterized by the author in [Sie+23b] with

$$\Delta_c^{(l)} = \Delta_c^{(l+1)} \leq 1/(2B), \quad l = 1, \dots, (N_{\text{eq}} - 1)/2 - 1 \quad (2.44)$$

$$\Delta_c^{(l)} = \Delta_c^{(1)} \beta^{l - (N_{\text{eq}} - 1)/2}, \quad l = (N_{\text{eq}} - 1)/2, \dots, (N_{\text{corr}} - 1)/2, \quad (2.45)$$

where N_{eq} is the number of equivalently spaced correlators around the LOS and β is the exponential base that determines the increase of the correlator spacing towards the outside. The nonuniform spacing results in a larger correlator bank width W_{bank} without adding additional correlators, alleviating the model approximation of finite CIRs. On the other hand, a correlator spacing exceeding $1/(2B)$ introduces errors itself by violating the Nyquist condition. The tradeoffs will be analyzed in Subsection 3.2.2.2 of the next chapter.

2.3.4 Receiver Architecture

Figure 2.2 schematically illustrates the proposed multi-correlator-based multipath mitigation algorithm integrated into a GNSS receiver architecture. It represents the required components to track all N_{sig} signals of one satellite frequency band and provide the tracking results to the position, velocity, and time (PVT) solution. The radio frequency (RF) signal from the front end is fed into the architecture from the left and is first of all down-converted with a mixer. The carrier replica required for this is generated using a numerically-controlled oscillator (NCO). The baseband signal \mathbf{y}_k , see Equation (2.10), is then passed to the correlator banks \mathbf{C}_i from Equation (2.25), one for each signal component of the tracked satellite. Correspondingly, N_{sig} correlator output vectors $\tilde{\mathbf{z}}_{i,k}$ are obtained, as defined in Equation (2.26). The data bits are estimated and wiped-off from the correlator outputs for the code and carrier tracking. This is possible at sufficiently high carrier-to-noise density ratios (C/N_0 s), which is the case when a reasonable delay estimation can be made. The MMEKF processes all correlator outputs. The estimated code delay and Doppler $\hat{\tau}_k^{(0)}$ and $\hat{\tau}_k^{(0)}$, respectively, are then used to drive the correlator banks, ideally free of multipath errors. Furthermore, $\hat{\tau}_k^{(0)}$ is required for the PVT solution. The carrier phase tracking is implemented with a PLL. It relies on all central correlator outputs, i.e., the prompts. The individual prompts are summed up coherently for the PLL to reduce noise after the data bits were wiped-off. In case the navigation signals are broadcast in different phase positions, all prompts must be rotated accordingly to match the primary signal $i = 1$.

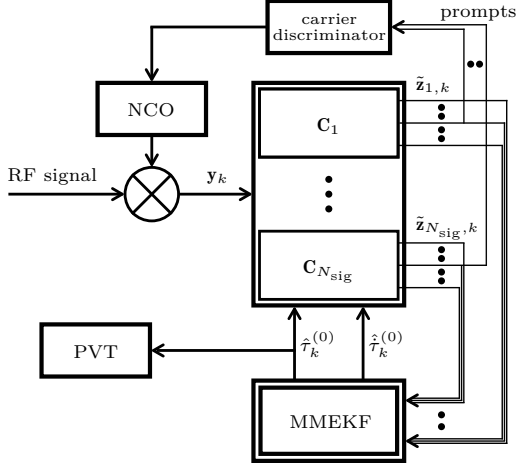


Figure 2.2: Proposed receiver architecture for the MMEKF.

2.3.5 Local Pseudorandom Noise Replicas

Local replicas of the PRN signals s_i are required for all GNSS receivers to conduct the correlation. Our proposed MMEKF does not depict an exception. In fact, it additionally uses them in its measurement model. For our implementation, we determined the local replicas $s_i(t)$ for the correlator banks and the EKF measurement model analytically from the ground up as follows. A pulse shape with a finite spectrum has been used to compose the PRN signal out of the superposition of adjacent sampled pulses. Since band-limited pulses are infinite in time, it is inevitably to neglect the contribution to neighboring pulses at some point to make an implementation feasible. We neglected contributions after $\pm 10T_c$. The resulting residual error was insignificant. Yet, any discrepancies between the local replica and the actually received signal would simply be absorbed by the estimated CIR.

2.3.6 Effect of Doppler

A Doppler shift is introduced to the received signal by the relative velocity between satellite and user. This effect has not been considered by the signal model derived in Section 2.1 and the algorithm description in Section 2.3 for a better readability. Nevertheless, the Doppler frequencies in the received signal require an equivalent shortening and stretching of the local replicas in the correlator banks C_i and the measurement model of the EKF, see Equation (2.34). Since Doppler frequencies are constantly changing over time, a precomputation of the autocorrelation functions for the measurement prediction and the Jacobian with Equations (2.43) and (2.42), respectively, is then no longer that straightforward. The effect of the Doppler is in particular dominant for wideband signals and cannot be disregarded. This work,

however, focuses on narrow band navigation signals. In addition to that, the observed Doppler frequencies are for most GNSS applications in the range of ± 10 kHz. This corresponds to a shortening or stretching of $s_i(t)$ over one code period $T_{\text{code},i}$ of less than $T_c/100$ for the GPS C/A code. The effect on the autocorrelation functions $\Phi_{s_i s_i}$ and the correlation results $\tilde{\mathbf{z}}_{i,k}$ is negligible. We therefore chose to use exclusively local replicas with zero Doppler and not adjust for any Doppler changes in return for a lower computational complexity.

2.3.7 Algorithm Initialization

As the applied EKF is an iterative algorithm, initial values are required. The initial state covariance matrix $\mathbf{P}_{-1|-1}$ has already been defined in Equation (2.41). For the initial state vector $\hat{\mathbf{x}}_{-1|-1}$ a LOS code delay and Doppler estimate is required. It turned out to be a reliable solution to start the tracking with a conventional EML-based DLL. Once it reached a stable tracking state, one switches over to the MMEKF. The initial code delay and code Doppler estimates $\hat{\tau}_{-1|-1}^{(0)}$ and $\hat{\dot{\tau}}_{-1|-1}^{(0)}$, respectively, are then set according to the latest tracking results. The initial CIR estimates are simply set to $\hat{h}_{-1|-1}^{(0)} = 1$ and $\hat{h}_{-1|-1}^{(l)} = 0$, $l \neq 0$.

3 Analysis of Scalar Tracking With Multi-Correlator-Based Multipath Mitigation

This chapter investigates the proposed multipath mitigating EKF (MMEKF) from the previous Chapter 2 with respect to its multipath mitigation capability, its dynamic response, and its code tracking noise performance. Comparisons are drawn to the conventional early minus late (EML)-based delay locked loop (DLL) [Kap+06, Chapter 5] as well as to two well-known representatives for multipath mitigation and estimation techniques, i.e., the high-resolution correlator (HRC) [McG+99] and the multipath estimating delay locked loop (MEDLL) [vNee92b].

3.1 Simulation Parameters

All signals considered in this chapter are generated synthetically, as explained in Subsection 2.3.5, using the first pseudorandom noise (PRN) code of the corresponding signal. A sampling frequency of $f_s = 20$ MHz and a one-sided signal bandwidth of $B = 10$ MHz were used. No navigation data bits were added to the signals. Moreover, all signals have zero Doppler. Correspondingly, we were able to omit the use of a dedicated carrier tracking for the investigations in this chapter and assumed instead an error-free carrier tracking. This allows for an isolated examination of the code tracking performance, independent of carrier tracking effects.

The conventional EML-based DLL uses an early-late spacing of $\Delta_{el} = 0.1T_c$. For the HRC, one additionally has to define the spacing between the very early and very late correlators which is set to $0.2T_c$. The second order loop filter, that is used for the EML- and HRC-based DLL relies on a bandwidth of 0.5 Hz. All correlator outputs are integrated over $T_{\text{int}} = 20$ ms. In case multiple signals per band per satellite are tracked, as it is the case with the Galileo E1 Open Service (OS), the correlator outputs for the DLL-based code tracking are averaged to reduce noise. Table 3.1 summarizes the general parameters.

For the MMEKF, Table 3.2 provides the state and process noise covariances. The measurement noise standard deviation (STD) of the constraining measurement is set depending on the number of correlators in the correlator bank according to the values listed in Table 3.3. Those values will be derived in Subsection 3.3.1. If not otherwise specified, the tuning parameter for the measurement noise scaling from Equation (2.36) is set to $\alpha = 1$. The measurement noise variance σ_η^2 is set to a value suitable for a carrier-to-noise density ratio (C/N_0) of 45 dB Hz. The correlator banks used for the MMEKF, and also the MEDLL, rely on a uniform correlator spacing of

Table 3.1: General simulation parameters.

Parameter	Value
Sampling frequency f_s	20 MHz
One-sided bandwidth B	10 MHz
Correlator integration time T_{int}	20 ms
Early-late spacing	$0.1T_c$
Very early-very late spacing	$0.2T_c$
Code loop filter order	2
Code loop filter bandwidth	0.5 Hz
Correlator spacing $\Delta_c^{(l_c)}$	$0.05T_c$

$\Delta_c^{(l)} = \Delta_c^{(l+1)} = 0.05T_c$, $\forall l > 0$, unless otherwise specified. The initial line-of-sight (LOS) code delay and Doppler estimates $\hat{\tau}_{-1}^{(0)}$ and $\hat{\tau}_{-1}^{(0)}$, respectively, are set to the ground truth values. The channel coefficients $h_{-1}^{(l_h)}$ for the initial channel impulse response (CIR) estimate of the MMEKF are set to $h_{-1}^{(l_h)} = 0$, $l_h \neq 0$ and $h_{-1}^{(0)} = 1$.

3.2 Multipath Error Envelopes

A common metric to compare different code tracking algorithms with respect to their multipath robustness is the multipath error envelope [Bra01]. It visualizes the tracking errors in a two path multipath environment, i.e., an environment where the LOS is superimposed with an additional delayed, attenuated, and phase shifted replica. The access delay of the multipath signal with respect to the LOS is referred to as the multipath delay τ_{mul} defined in seconds. The tracking error $\tau_{\text{err}}^{(0)}$ is the difference between the actual LOS code delay $\tau^{(0)}$ and the estimated one $\hat{\tau}^{(0)}$ with

$$\tau_{\text{err}}^{(0)} = \hat{\tau}^{(0)} - \tau^{(0)}. \quad (3.1)$$

For the envelopes in the following, a sweeping multipath has been simulated with its access delay stepwise increased from 0 up to 650 m. Its LOS to multipath power ratio is set to 3 dB. The envelopes show the range of code tracking errors that are obtained for a specific multipath delay during a full multipath phase cycle. Each delay and phase combination was maintained until a steady tracking state was reached.

For the MMEKF the correlator bank width was set to $W_{\text{bank}} = T_c$, which results

Table 3.2: State and process noise variances of MMEKF.

	Initial state covariance $\mathbf{P}_{-1 -1}$	Process covariance matrix \mathbf{Q}
Code delay τ	$\sigma_{\mathbf{P},\tau} = 0.01T_c$ $\sigma_{\mathbf{P},\dot{\tau}} = 0.01T_c/\text{s}$	$\sigma_{\mathbf{Q},\ddot{\tau}} = 0.02T_c/\text{s}^2$
CIR \mathbf{h}	$\sigma_{\mathbf{P},\mathbf{h}} = 0.05/\text{s}$	$\sigma_{\mathbf{Q},\mathbf{h}} = 10^{-3.3}/\text{s}$

Table 3.3: Measurement noise STD of constraining measurement.

N_{corr}	σ_{constr}	N_{corr}	σ_{constr}
3	$10^{-2.63}$	13	$10^{-4.63}$
5	$10^{-3.44}$	17	$10^{-4.85}$
7	10^{-4}	25	$10^{-5.2}$
9	$10^{-4.28}$	33	$10^{-5.37}$
11	$10^{-4.49}$	41	$10^{-5.88}$

with the correlator spacing of $\Delta_c^{(l)} = 0.05T_c$, $\forall l > 0$ in a total of $N_{\text{corr}} = 41$ correlators. The goal of this large correlator bank is to determine the best possible multipath mitigation performance of the MMEKF. Moreover, the large correlator bank allows to determine the CIR for an equally large range of delays, which facilitates the analysis of different estimation characteristics of the MMEKF. Results with smaller correlator banks can be found in Subsection 3.2.2. The multipath error envelopes with the full $N_{\text{corr}} = 41$ correlators can be found in Figure 3.1a and 3.1b for the Global Positioning System (GPS) coarse/acquisition (C/A) code and for the Galileo E1 OS B ranging code with a simplified BOC(1,1) modulation, respectively. The multipath error envelope of an EML discriminator is well known and have been analyzed for different signals before, see for example [Irs+04]. Regarding the results of the MMEKF, a superposition of in total three different phenomena led to the obtained multipath error envelope shapes. They are discussed in detail in the following.

First of all, the multipath error increases with increasing multipath delay up to errors of 5.4 m, as expected and similar to the EML discriminator. For delays between 5 and 15 m, depending on the phase offset between LOS and multipath, the algorithm begins to differentiate between the two signal replicas. Correspondingly, the error starts to decrease and reaches zero again for multipath delays of approximately 24 m. Afterwards, an oscillating error can be observed. This fluctuation origins from the shape of the estimated CIR, see Figure 3.2. As soon as a multipath does not perfectly align with one of the CIR taps, side peaks arise. In Figure 3.2a, for example, this can be observed as small ripples between the main signal components for multipath delays < 300 m. The superposition of theses side peaks with the LOS cause the global maximum of the CIR to deviate slightly from the LOS delay, alternating to the left and right. With the constraining measurement enforcing the maximum signal power in the central channel tap, the code delay is correspondingly adjusted, leading to oscillating errors. This effect applies equally to both signals considered.

Secondly, another increase in error is obtained around $293 \text{ m} \triangleq T_c$ and $146.5 \text{ m} \triangleq T_c/2$ for the GPS and Galileo signal, respectively. This is caused by the constraining measurement. On the one hand, the MMEKF attempts to replicate the observed correlator outputs as accurately as possible through its measurement model by adjusting the estimated CIR accordingly. On the other hand, the constraining measurement is best satisfied with a CIR that has maximal power in the central channel tap $h_k^{(0)}$ and minimal power in the remaining ones. These generally contradictory optimization

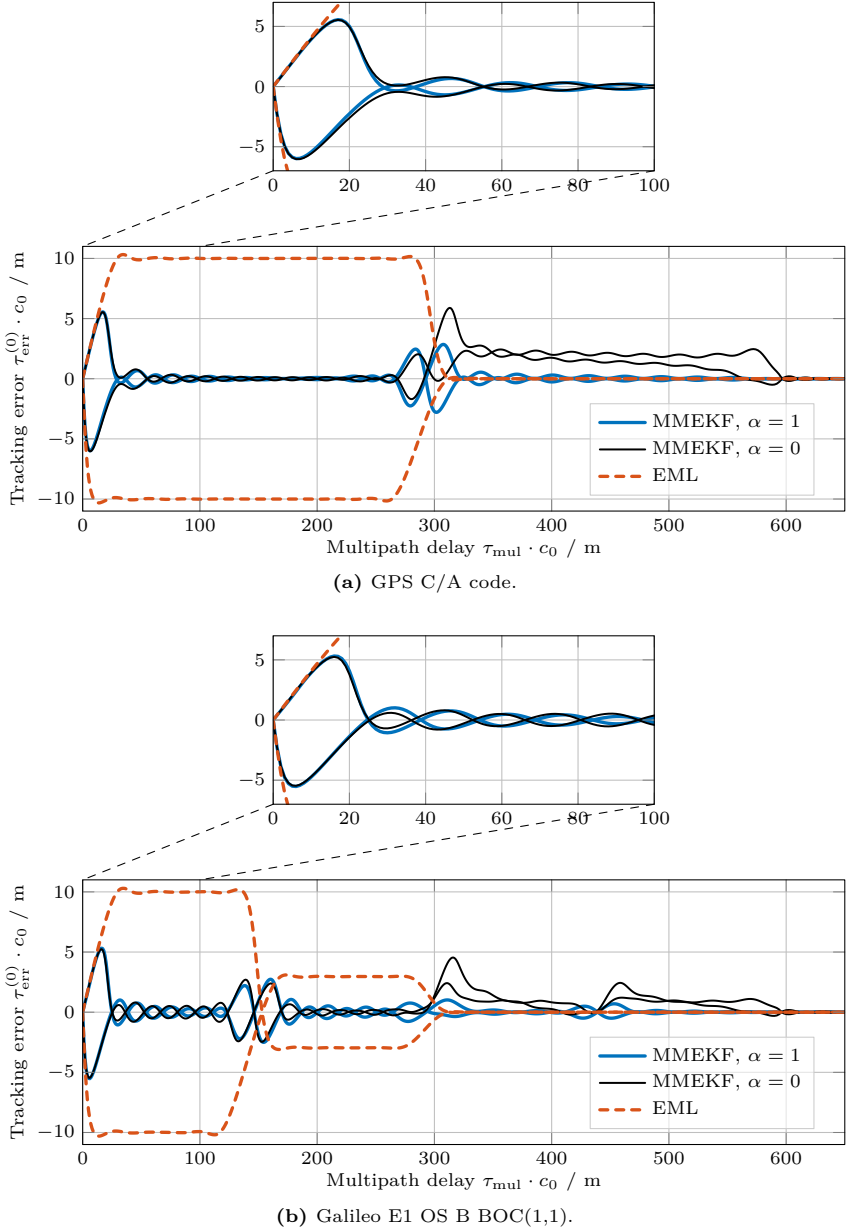


Figure 3.1: Multipath error envelopes. The considered signals have a one-sided bandwidth of $B = 10$ MHz and a LOS to multipath power ratio of 3 dB. For the EML discriminator, the early-late spacing was set to $0.1T_c$. With the tuning parameter set to $\alpha = 1$, the approximation made in the signal model is accounted for, see Subsection 2.3.2, largely eliminating the biased envelopes for delays between T_c and $2T_c$.

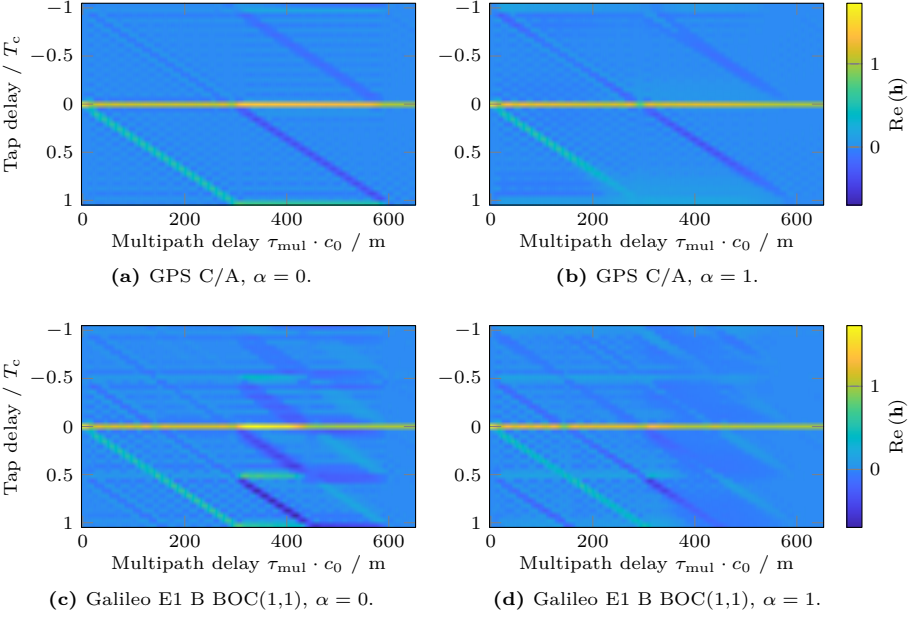


Figure 3.2: CIRs for different multipath delays. The single in-phase multipaths with 3 dB LOS to multipath power ratio sweeps from 0 to 650 m. Only the real parts of the estimated CIRs are shown as the imaginary components are zero with this in-phase multipath.

criteria inevitably lead to a compromise between an accurate CIR estimate and a distorted one. The MMEKF will end up with a CIR estimate with a too high amplitude for the LOS tap and too low amplitudes for the remaining coefficients. The extent of this distortion depends on the chosen measurement noise variances. In addition to that, side peaks arise in the CIR estimate as an attempt to compensate for the overestimation of the LOS amplitude and better match the observed correlator outputs. These can be seen in Figure 3.2. The LOS and multipath is accompanied by additional peaks every T_c for the GPS C/A code. The Galileo signal with its BOC(1,1) modulation shows these peaks every $T_c/2$ due to the doubled post-modulation chip rate. When the side peaks of the sweeping multipath traverse the LOS, it causes a shift of the global maximum of the estimated CIR and with that to tracking errors. The tighter the constraint is set via its measurement noise variance σ_{constr}^2 , the more pronounced is this effect. On the other hand, a too loose constraint might not be able to keep the LOS reliably in place, causing potentially divergence.

Last but not least, a third phenomena can be observed for multipath delays between T_c and $2T_c$ without the correlator output covariance scaling, i.e., $\alpha = 0$. These delays are located outside of the correlator bank but their correlation triangles still extend into the sampled part of the correlation result. Since $W_{\text{CIR}} = W_{\text{bank}}$ applies,

the CIR cannot properly represent such multipaths. Yet, the extended Kalman filter (EKF) attempts to match the observed correlation result best possible with the available CIR taps, which leads to additional side peaks. As for the previous two effects, these additional peaks are superimposed with the LOS leading to tracking errors, see Figures 3.2a and 3.2c. By extending the correlator bank and the CIR width to $T_{\text{code}}/2$ it is ensured that the correlation output is periodic which would resolve these errors. However, the additional computational cost would be disproportionately high and would go beyond the scope of a practicable implementation. Alternatively, one can account for the model approximation by applying a scaling of the correlator output covariance matrix $\mathbf{R}_{\tilde{\mathbf{r}}_{\text{C}_i}}$, as we proposed with Equation (2.36) in Subsection 2.3.2. With $\alpha = 1$, a Hann window shaped scaling is chosen, largely resolving this problem. In Figures 3.2b and 3.2d, the effect of the scaling can be seen by the strongly suppressed side peaks from 300 m onwards and the accordingly improved envelopes in Figures 3.1.

As stated in Section 3.1, we have used the first PRN code for the envelopes in Figure 3.1. While the autocorrelation of different Galileo E1 OS PRNs are basically identical between $-T_c$ and T_c , the GPS L1 C/A code shows slight variations across different PRNs. These minor variations in the autocorrelation function affect the resulting multipath error envelopes. However, in view of the insignificance of this effect, it is not considered further here.

3.2.1 Comparison With Other Multipath Mitigation Techniques

Previously, the proposed solution with its multipath mitigating capability outperformed an EML discriminator. This is expected as this conventional approach does not consider multipath propagation in its estimation process. In the literature many different multipath mitigation techniques have been proposed, see Section 1.2. A comparison is therefore made in the following between the proposed MMEKF, the HRC [McG+99] and the MEDLL [vNee92b].

Figure 3.3 compares the multipath error envelopes of the different solutions. We chose the HRC to cover the category of multipath mitigating algorithms and the MEDLL as an exemplary algorithm for a multipath estimating approach using a structured channel model. For the MEDLL we used the same correlator bank as for the MMEKF with $N_{\text{corr}} = 41$. The comparable simple HRC performs nearly as good as the proposed solution and the MEDLL with respect to the multipath error envelope. This is quite respectable, especially given that only four correlators are used for the code tracking. The catch of the HRC is its inferior noise performance [McG+99], see Section 3.4. On the other hand, the MEDLL manages to slightly outperform the proposed solution regarding its multipath error envelope. This comes at the cost of a higher computational load, at least in our implementation of the MEDLL. It should be noted that, at present, there is no dedicated publication covering our MEDLL implementation. However, it follows closely the original publication from [vNee92b]. See Table 3.4 for a comparison of the required number of operations for the two algorithms. It turned out that the proposed solution required three to four times

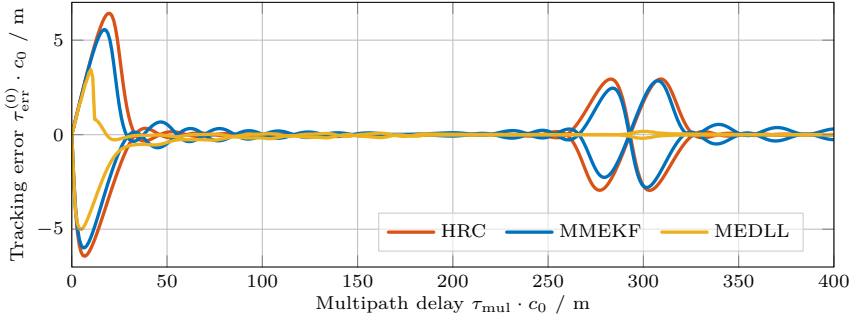


Figure 3.3: Multipath error envelopes of different multipath mitigation techniques. The considered GPS C/A code signals have a 3dB LOS to multipath power ratio, as for the envelopes in Figure 3.1a.

Table 3.4: Number of elementary operations of different multipath mitigation algorithms.

	Addition	Subtraction	Multiplication	Division
MEDLL implementation with $N_{\text{corr}} = 41$	12,405,800	11,443	12,764,367	1,975
MMEKF with $N_{\text{corr}} = 41$	3,479,519	575,399	4,089,494	13,780

less additions and multiplications than the MEDLL. The increase in subtractions and divisions can in this case be neglected as they are at a lower magnitude. Note, Section 2.3.3 provides more details on complexity considerations for the MMEKF.

3.2.2 Low-Complexity Variants

For the multipath error envelopes derived above, the MMEKF relied on a correlator bank with $N_{\text{corr}} = 41$ correlators, uniformly distributed across the entire correlation triangle. Such a large correlator bank allows to conveniently resolve the CIR for a wide range of delays, which facilitates insights into the estimation characteristics of the MMEKF. On the other hand, the large number of correlators does come along with an increased computational load. Subsection 2.3.3 discussed the effect of the number of correlators onto the overall computational burden of the MMEKF. Different correlator bank setups were proposed to lower the total number of correlators N_{corr} . In the following, the multipath mitigation performance tradeoffs made when using these complexity reduction approaches are analyzed. This will address the second research question formulated in Section 1.3 which asked specifically for the performance tradeoffs made, when the complexity of the algorithm is reduced.

In order to easily compare the multipath mitigation performance, two error met-

rics are derived from the multipath error envelopes with

$$E_1 = \max_{\tau, \phi} |E_{\text{trk}}(\tau, \phi)| \quad (3.2)$$

$$E_2 = \text{mean}_{40 \text{ m} \leq \tau \leq 100 \text{ m}} \max_{\phi} |E_{\text{trk}}(\tau, \phi)|, \quad (3.3)$$

where $E_{\text{trk}}(\tau, \phi)$ is the function describing the multipath error envelope depending on the multipath delay and phase τ and ϕ , respectively. E_1 indicates the maximal absolute error that is obtained. This is typically achieved for short delay multipaths. The second error metric E_2 provides information about the maximal average multipath error to which the envelopes converge after the first error peak. For the considered setup here, multipath delays larger than 40 m were considered for this error metric. With this lower bound, the first error peak for short delay multipaths has been excluded for all considered cases. As the envelopes show little variation between this initial error peak and the peaks around T_c , and the increasing loss in importance of multipaths with larger delays [Irs+05], we set an upper bound to 100 m.

3.2.2.1 Uniform Sampling With Reduced Correlator Bank Width

In the following, we will lower the number of correlators by simply reducing the width of the correlator bank W_{bank} while maintaining the uniform correlator spacing $\Delta_c^{(l)} = 0.05T_c$, $\forall l > 0$, as described in Subsection 2.3.3.1. The effect of this complexity measure can be observed in the resulting multipath error envelopes in Figure 3.4, where the width of the correlator bank was stepwise reduced. With the full correlator bank, i.e., $W_{\text{bank}} = T_c$ and correspondingly $N_{\text{corr}} = 41$, the best multipath mitigation performance can be achieved. Narrowing the correlator bank and therewith reducing the number of correlators increases the errors for short and medium delay multipaths. For very low number of correlators, e.g., $N_{\text{corr}} = 7$, an error plateau can be observed for multipath delays between 40 and 260 m meters. This is caused by the enabled measurement noise scaling with $\alpha = 1$. The effect of this noise scaling has been analyzed before for correlator banks with $W_{\text{bank}} = T_c$, see the discussion of Figure 3.1. Figure 3.5 illustrates the effect of this measure onto the error envelopes for two exemplary narrower correlator banks, i.e., $W_{\text{bank}} = 0.15T_c$ and $W_{\text{bank}} = 0.4T_c$. As expected, for $\alpha = 0$, both cases show an error bias for multipath delays between $W_{\text{bank}} \leq \tau \leq W_{\text{bank}} + T_c$, as these multipaths cannot be accurately represented by the estimated CIR. Setting $\alpha = 1$ largely eliminates this bias for the wider case with $W_{\text{bank}} = 0.4T_c$. For the narrower correlator bank with $W_{\text{bank}} = 0.15T_c$, the bias arises before the error reaches zero again. In this case, the measurement noise scaling only manages to trade in the bias with an error plateau.

In order to better illustrate the performance tradeoffs made with this complexity reduction approach, the two error metrics defined in Equations (3.2) and (3.3) are plotted over the number of correlators in Figure 3.6. One can clearly see how both error metrics, E_1 and E_2 , quickly converge towards 6.35 m and 0.27 m, respectively, with increasing N_{corr} . No significant improvement can be achieved when increasing the number of correlators beyond $N_{\text{corr}} > 11$. Therewith, a valid compromise be-

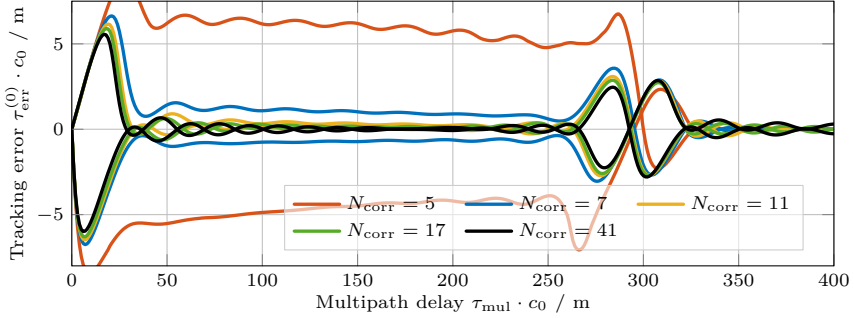


Figure 3.4: Multipath error envelopes of MMEKF for different numbers of correlators N_{corr} and a uniform correlator spacing. The considered GPS C/A code signals have a 3 dB LOS to multipath power ratio, as for the envelopes in Figure 3.1a.

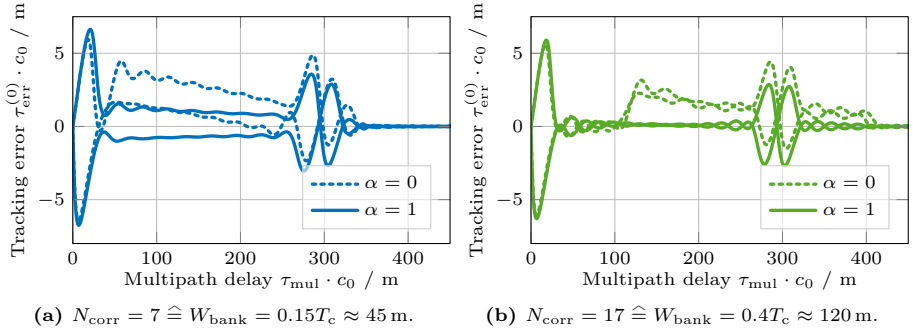


Figure 3.5: Effect of measurement noise scaling on multipath error envelopes. The considered GPS C/A code signals have a 3 dB LOS to multipath power ratio.

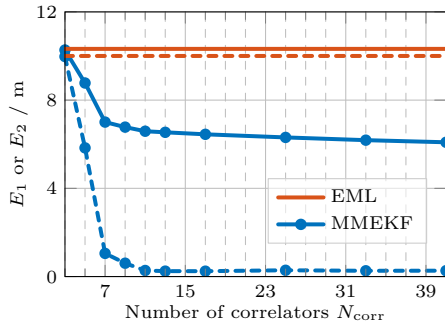


Figure 3.6: Error metrics E_1 of Equation (3.2) and E_2 of Equation (3.3) for different numbers of correlators N_{corr} and a uniform correlator spacing. The metrics were derived from multipath error envelopes using GPS C/A signals, see Figure 3.4. No significant improvements w.r.t. to these error metrics are obtained for $N_{\text{corr}} \geq 11$. E_1 is represented by the solid lines, E_2 by the dashed ones.

tween performance and complexity for the considered signal bandwidth B with this correlator distribution is to not rely on more than $N_{\text{corr}} = 11$ correlators.

When the number of correlators is reduced down to only $N_{\text{corr}} = 3$, the MMEKF error envelope converges towards the one from a conventional EML discriminator. This is expected, as in this edge case, the measurement model of the MMEKF with its constraining measurement is effectively reduced down to a simple EML discriminator, where the early and late correlators are held at an equal level.

It can be concluded, that the computational complexity of the MMEKF can indeed be brought down to a reasonable level without scarifying its multipath mitigation performance significantly. For the considered setup, adding more than $N_{\text{corr}} = 11$ correlators turned out to reach the point of diminishing returns. This answers the second research question formulated in Section 1.3. In an attempt to further reduce the number of correlators, or, achieve a higher multipath resilience with the same number of correlators, a nonuniform correlator placement is analyzed in the following.

3.2.2.2 Nonuniform Sampling

In Subsection 2.3.3.2, a nonuniform correlator placement was described. In contrast to the uniform correlator spacing from before, this allows to increase the total width of the correlator bank, without adding additional correlators. An increased width is desirable, in order to alleviate the signal model approximation made with finite CIR widths. The countermeasure with the measurement noise scaling from Equation (2.36) reaches its limits for very narrow correlator banks, as unveiled in Figure 3.5. On the other hand, a larger correlator spacing violates the Nyquist condition, introducing errors. The tradeoff will be analyzed in the following.

The nonuniform correlator spacing has been parameterized with Equation (2.45). It is determined by N_{eq} equally spaced correlators around the LOS and the exponential factor β , regulating the correlator spacing increase for the remaining outer correlators. In order to find a well working nonuniform correlator distribution, the error metrics E_1 and E_2 were determined for different β and different N_{eq} . Parameter combinations that led to widths $W_{\text{bank}} > T_c$ were discarded. The results are shown in Figure 3.7. The measurement noise scaling remained enabled in all considered cases with $\alpha = 1$. As already discovered by the author in [Sie+23b], $N_{\text{eq}} = 1$ leads to significant error metric increases for both, E_1 and E_2 . In order to allow for a reasonable axis scaling, those results were partially clipped. Moreover, it was found that for $N_{\text{corr}} = 7$ and $N_{\text{corr}} = 9$ with $N_{\text{eq}} = 5$, certain values for β managed to improve the error metrics. The improvement, however, is rather insignificant and applies not always to both of the two defined error metrics at the same time.

Thus, in contrast to [Sie+23b], no clear performance improvement was found for a nonuniform correlator distribution for the chosen σ_{constr} . This is because different measurement noise variances for the constraining measurement were used in [Sie+23b]. The dependency on σ_{constr} will be analyzed in the following Subsection in Figure 3.10.

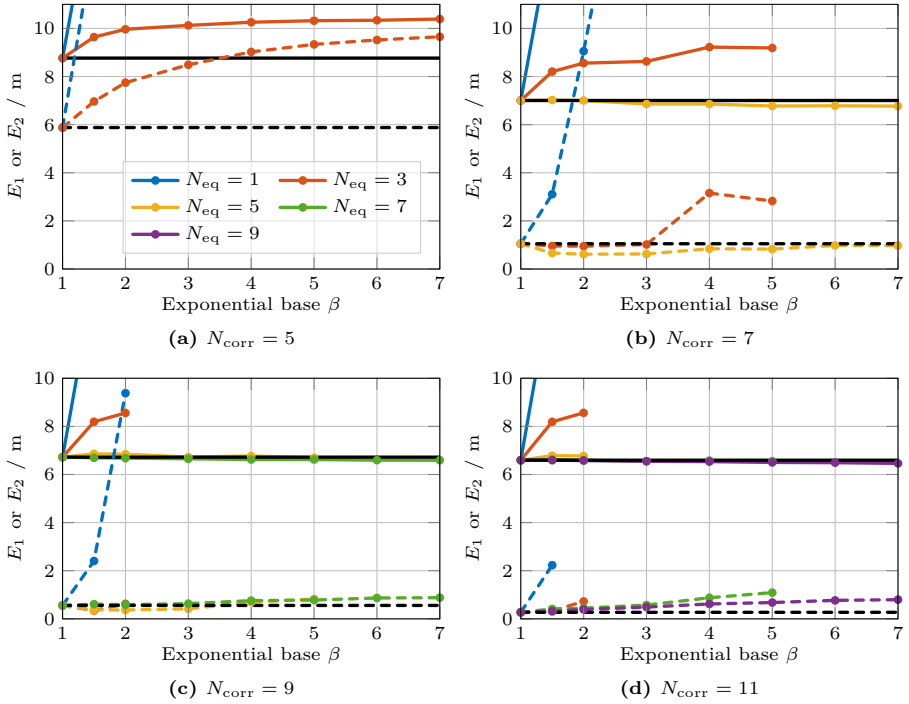


Figure 3.7: Error metrics for different nonuniform correlator distributions over β . The metrics were derived from multipath error envelopes using GPS C/A signals. E_1 is represented by the solid lines, E_2 by the dashed ones. The corresponding uniformly spaced cases are shown by the black curves with $N_{\text{eq}} = N_{\text{corr}}$ and therefore independent of β . The constraint measurement noise variance were set according to Table 3.3.

3.2.3 Effect of Measurement Noise Variance of Constraint

The constraining measurement has been introduced in Section 2.3 in order to ensure a reliable tracking of the LOS signal by enforcing the maximization of the signal power in the central channel tap. Its measurement noise variance σ_{constr}^2 determines the tightness of the constraint and depicts a tradeoff between overly distorting the estimated CIR and the risk to loose lock with the LOS signal. While the first occurs for small σ_{constr} and can worsen the multipath error envelopes, the latter may occur for too large σ_{constr} and lead to biased tracking results, see Subsection 3.3.1. The effect of the constraint onto the multipath error envelopes has been mentioned already during the discussion of the multipath error envelopes in Figure 3.1. In the following, this subject will be addressed in more detail.

Figure 3.8 shows the multipath error envelopes for a selection of constraint variances σ_{constr}^2 and number of correlators. One can clearly see, that with decreasing

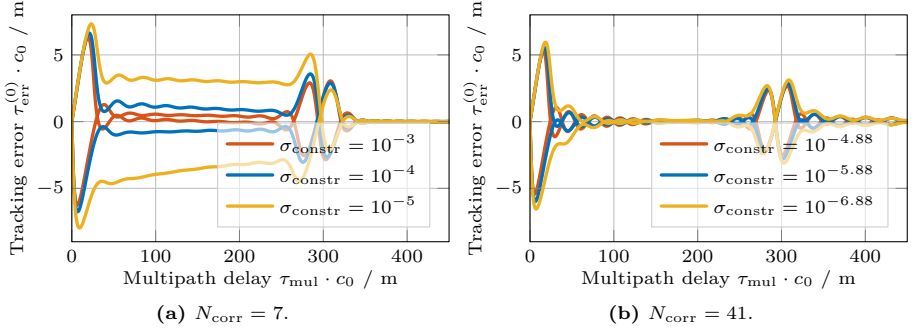


Figure 3.8: Multipath error envelopes for different σ_{constr} . Too small σ_{constr} lead to larger error envelopes.

σ_{constr} , the envelopes tend to be enlarged.

For a more systematic analysis, we have computed the error metrics E_1 and E_2 defined in Equations (3.2) and (3.3), respectively, from the derived envelopes. The result can be found in Figure 3.9. This representation confirms that tighter constraints indeed worsen the envelopes with respect to the defined error metrics, and that this critical value of σ_{constr} decreases as the number of correlators N_{corr} increases. Taking only the multipath error envelope of the MMEKF into account, the best results are in general obtained with the largest possible constraint variance σ_{constr}^2 . Only for low N_{corr} an upper bound for σ_{constr} has been observed beyond which the error metric E_2 increases again.

Figure 3.10 shows the error metrics over σ_{constr} for various nonuniform cases. The analysis of the nonuniform spacing in the previous section, see Figure 3.7, did not reveal any significant performance improvement over the corresponding uniform cases. The results in Figure 3.10 illustrate, that a nonuniform correlator placement can indeed bring a noteworthy advantage for smaller σ_{constr} . However, as for the uniformly distributed cases in Figure 3.9, the multipath mitigation performance with nonuniformly distributed correlators benefits in general from a larger constraint variance σ_{constr}^2 . Accordingly, for σ_{constr} for which the nonuniform correlator placement brings an improvement, the overall performance is still worse than with the uniform spacing and the chosen σ_{constr} . It can be concluded, that a nonuniform correlator spacing does not bring a mentionable improvement for the multipath error envelopes with respect to the defined metrics E_1 and E_2 for the chosen σ_{constr} .

For a reliable code tracking algorithm, however, other aspects are also of importance, such as its dynamic behavior. This will be analyzed in the following section. In doing so, the effect of the measurement noise variance of the constraint σ_{constr}^2 will be revisited in order to determine an upper bound for σ_{constr} for a reliable code tracking.

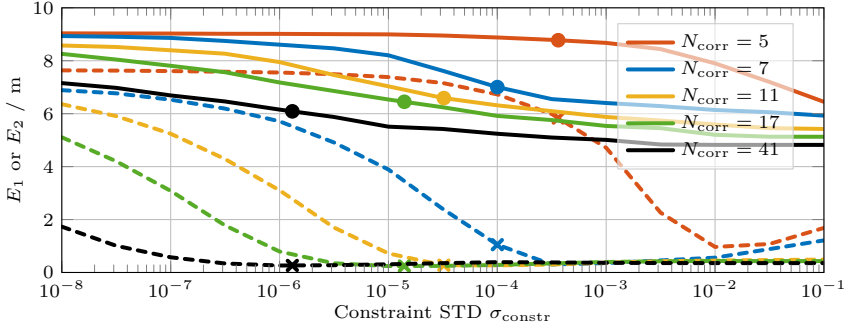


Figure 3.9: Error metrics E_1 of Equation (3.2) and E_2 of Equation (3.3) over different σ_{constr} . E_1 is represented by the solid lines, E_2 by the dashed ones. The chosen σ_{constr} are highlighted by circles and crosses. In general, larger σ_{constr} are favorable with respect to the multipath error envelopes.

3.3 Dynamic Response

So far, the chapter has focused on the multipath error of the proposed MMEKF in static environments. However, a real-world scenario is highly dynamic. This is not only due to the movement of the user and the satellites, which constantly affects the LOS code delay. The closer environment of the receiver as well as atmospheric conditions also have an effect on the signal propagation. Both can be subject to high fluctuations over time. The code tracking loop of a global navigation satellite system (GNSS) receiver has to cope with these temporal changes. Thus, the proposed MMEKF also needs to be validated in such dynamic environments. Before this is demonstrated with actual real-world data in Chapter 6, this is first investigated with synthetic signals below. In [Sie+23a], this topic has been briefly covered before. The analysis in the following is more in-depth and also demonstrates the effect of process and measurement model noise variances onto the dynamic response of the MMEKF.

The well-established DLL with an EML discriminator has proven to be a reliable solution under nominal conditions and is therefore used as a benchmark in the following. The DLL setup is described in Section 3.1. Since we use this DLL also as a reference in analyses later on, it is important to ensure that both code tracking algorithms have comparable dynamic responses. Otherwise, it cannot be unequivocally concluded that a superior noise performance or a more robust behavior in multipath environments is actually due to desirable algorithm characteristics. A slower step response, for example, also tends to reduce the variance of the code delay estimates and lower multipath errors due to the more pronounced averaging property.

The MMEKF used in the following relied on a correlator bank with $N_{\text{corr}} = 7$ correlators, if not otherwise specified. Considered are only GPS C/A signals. Noise is added to the synthetically generated GNSS signals so that a C/N_0 of 45 dBHz is achieved. The results shown were averaged over 5 Monte Carlo runs.

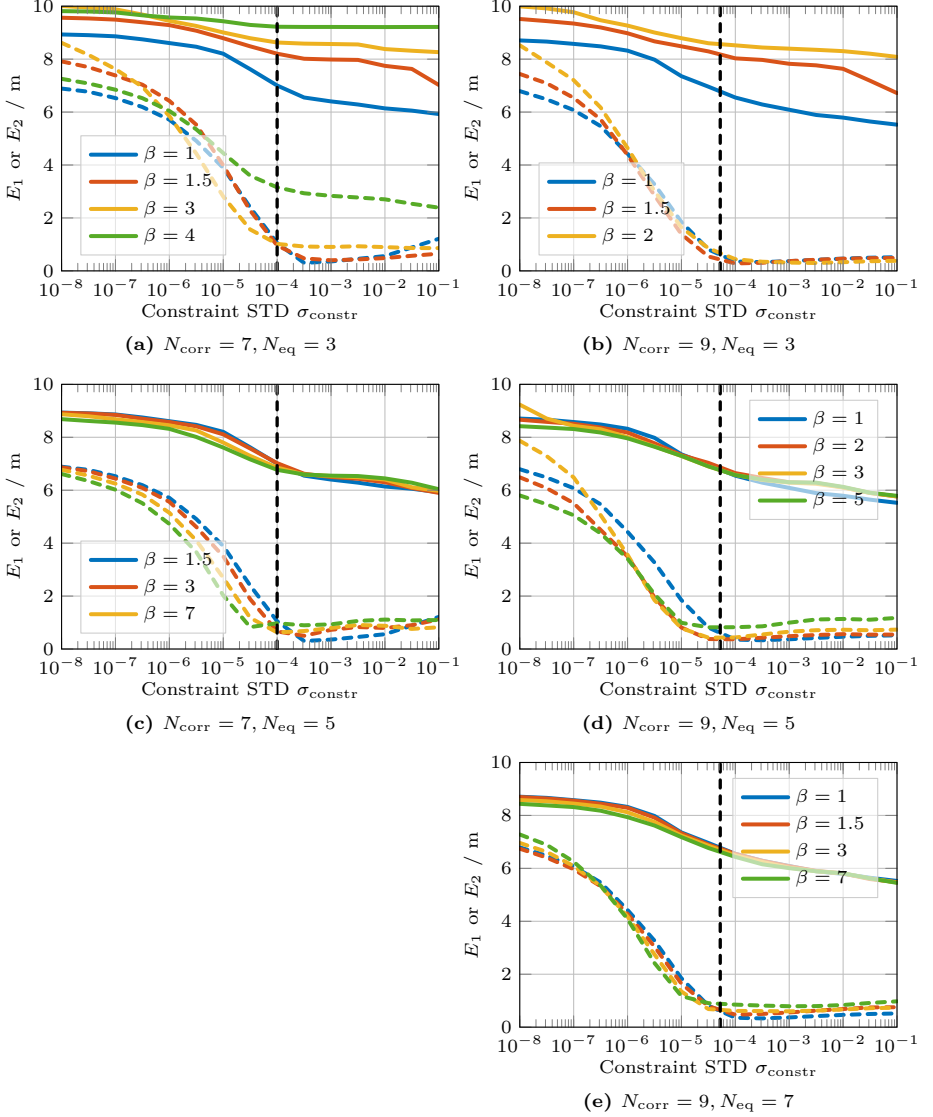


Figure 3.10: Error metrics E_1 of Equation (3.2) and E_2 of Equation (3.3) for different nonuniform correlator distributions and σ_{constr} . The metrics were derived from multipath error envelopes using GPS C/A signals. E_1 is represented by the solid lines, E_2 by the dashed ones. With $\beta = 1$, the correlators are spaced apart equidistantly. The black dashed line indicates the chosen value of $\sigma_{Q,h}$ for the corresponding number of correlators, see Table 3.3. The nonuniform correlator spacing can bring a mentionable performance improvement for smaller σ_{constr} than the chosen ones.

3.3.1 Step Response

In a first dynamic scenario, the sudden jump of the LOS code delay is simulated to investigate the step response. While this is not a scenario one typically faces in real-world environments, it depicts a good test to ensure, that the constraining measurement of the MMEKF is able to keep the LOS signal in lock. Moreover, it allows to compare the step response behavior of the MMEKF with a conventional DLL. Therefore, a LOS only scenario with zero Doppler is simulated, where after 5s the LOS code delay conducts a sudden jump. Figure 3.11 shows the resulting step responses for different jump heights and measurement noise variances of the constraint σ_{constr}^2 .

In Figure 3.11a, one can clearly see how both, the proposed MMEKF and the conventional EML-based DLL, manage to lock back in with the LOS code delay after approximately the same duration. In doing so, the MMEKF tends to show less overshooting with a correspondingly longer rise time than the DLL results. When σ_{constr} is set too large, in this case $\sigma_{\text{constr}} = 10^{-3}$, the MMEKF tends to track the LOS with a small offset after the jump, see the 10 m and 15 m jumps in Figure 3.11b. This causes biased tracking results. It is therefore crucial, to set the measurement noise variance of the constraint σ_{constr}^2 to a sufficiently small value in order to ensure a reliable tracking of the LOS signal.

The step response results of the MMEKF are therefore evaluated in Figure 3.12 with respect to the average tracking error between 10s and 20s after the LOS jump for different σ_{constr} and jump heights. For the here considered case of $N_{\text{corr}} = 7$, a STD not exceeding 10^{-4} is required in order to ensure a reliable tracking of the LOS signal after the jump. Smaller values are also possible. However, as discovered in Subsection 3.2.3, a possibly large σ_{constr} is preferable with respect to the multipath rejection capability.

In order to further generalize the results, the analysis is extended to different number of correlators N_{corr} . Therefore, the average tracking errors between 10s and 20s after a LOS jump were averaged over the jump heights 10m to 50m in 5m steps. Jump heights of 5m and below were neglected, as the measurement noise STD of the constraining measurement σ_{constr} showed only negligible effects for such small jumps, see the results above in Figure 3.12. For meaningful averaging across jump heights, we average the tracking errors as a percentage of their actual jump height rather than the absolute error. The result is shown in Figure 3.13. It clearly illustrates, that the maximal possible σ_{constr} depends on the number of correlators. This is due to the ratio between the number of measurements from correlator outputs and the single constraining measurement in the EKF. With more correlator outputs, the constraining measurement must be tighter to be weighted equally in the filter. In order to find suitable and comparable values for σ_{constr} for the different number of correlators N_{corr} , the break-off edge is first located. This is defined at a percentage tracking error of -1.5% , see the black dashed line in Figure 3.13. Then, by taking the chosen $\sigma_{\text{constr}} = 10^{-4}$ as a reference value for $N_{\text{corr}} = 7$, this line is shifted accordingly, resulting in the red dashed line. This provides us with measurement noise variances

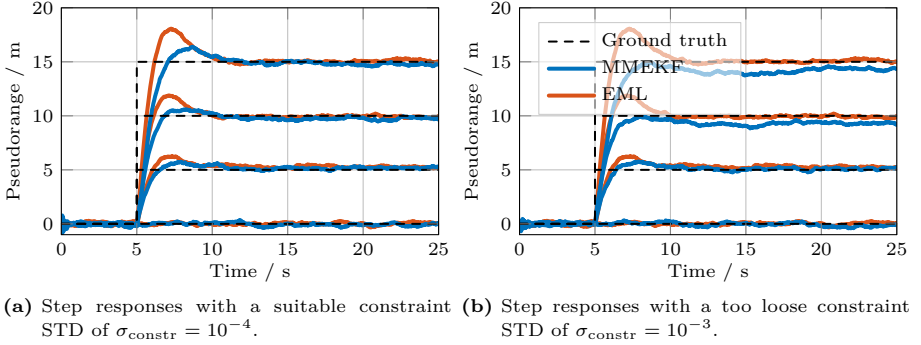


Figure 3.11: Step response of the proposed MMEKF compared with a conventional EML-based DLL. After an initial 5 s of static zero Doppler LOS only conditions, the LOS code delay jumps by a certain amount. The plots show four different jump heights of 0, 5, and 10 m. A too large measurement noise variance of the constraint σ_{constr}^2 can cause the MMEKF to no longer be able to track the LOS free of biases, see the 10 and 15 m jumps in Figure 3.11b.

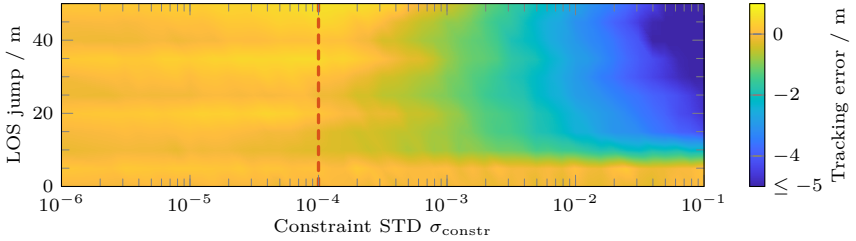


Figure 3.12: Illustrated is the average tracking error between 10 s and 20 s after a LOS code delay jump. The plot unveils that the measurement noise STD of the constraint should be $\sigma_{\text{constr}} \leq 10^{-4}$ in order to ensure a reliable LOS tracking when using $N_{\text{corr}} = 7$. The chosen value of $\sigma_{\text{Q,h}} = 10^{-4}$ is highlighted with the red dashed line.

of the constraining measurements for all considered N_{corr} , as listed in Table 3.3.

Section 3.2.2.2 investigated an alternative nonuniform correlator placement with the attempt to improve the multipath mitigation performance without increasing complexity. It turned out that for the chosen σ_{constr} , a nonuniform correlator placement cannot achieve a noteworthy performance improvement. For the analysis we assumed that the same σ_{constr} suitable for the corresponding uniformly distributed case would be appropriate for the nonuniform cases as well. In order to demonstrate, that this was a valid assumption, Figure 3.14 shows the corresponding step response results exemplary for $N_{\text{corr}} = 7$ and $N_{\text{eq}} = 5$. It can be seen that the percental tracking error is largely independent of β . Thus, the value for σ_{constr} for uniformly distributed correlators, i.e., $\beta = 1$, can be equally applied to nonuniform correlator distributions.

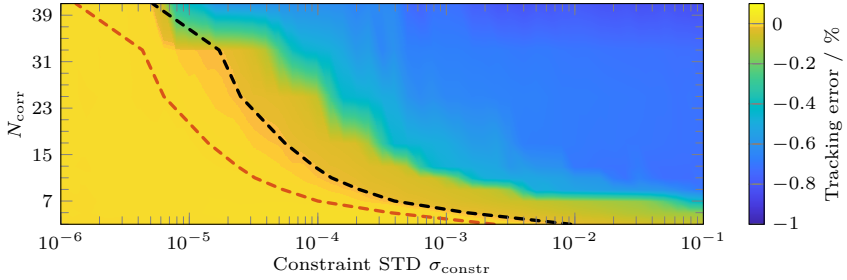


Figure 3.13: Illustrated is the average tracking error between 10 s and 20 s after a LOS code delay jump. Jump heights between 10 m and 50 m in 5 m steps were considered. For a meaningful averaging across different jump heights, the resulting tracking errors were averaged as their percentage of their actual jump height. The plot unveils the maximal possible measurement noise STD of the constraint for different N_{corr} . In general, the more correlators are used, the smaller σ_{constr} must be. The black dashed line marks the break-off edge. Taking the σ_{constr} chosen for $N_{\text{corr}} = 7$ as a reference, this line is accordingly shifted, providing suitable σ_{constr} for all possible N_{corr} .

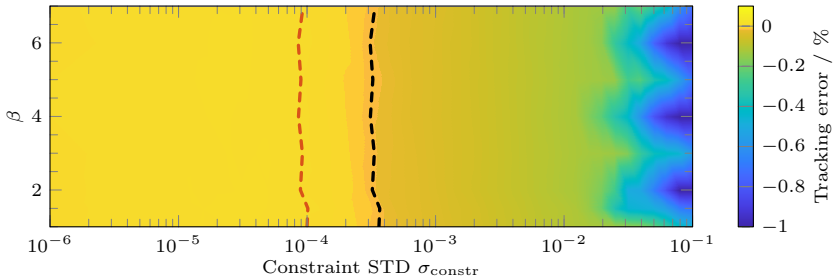


Figure 3.14: Illustrated is the average tracking error between 10 s and 20 s after a LOS code delay jump for nonuniform correlator distributions with $N_{\text{corr}} = 7$ and $N_{\text{eq}} = 5$. Jump heights between 10 m and 50 m in 5 m steps were considered. For a meaningful averaging across different jump heights, the resulting tracking errors were averaged as their percentage of their actual jump height. The plot unveils the maximal possible measurement noise STD of the constraint for different β . The black dashed line marks the break-off edge. Taking the σ_{constr} chosen for $\beta = 1$, i.e., the uniform case, as a reference, this line is accordingly shifted, providing suitable σ_{constr} for the nonuniform cases with $\beta > 1$. A nonuniform correlator distribution does not affect the maximal possible σ_{constr} .

3.3.2 Convergence Behavior

In a second dynamic scenario, the convergence behavior of the proposed MMEKF to a change in the propagation path has been investigated. Therefore, a single in-phase multipath with a 3 dB power attenuation with respect to the LOS appears after 5 s static zero Doppler LOS only conditions.

Figure 3.15a and 3.15b show the results for an arising multipath with an additional path delay of 10 and 30 m, respectively. Both code tracking algorithms, the proposed MMEKF as well as the conventional EML-based DLL, adjust accordingly to the new propagation path characteristics. For the DLL, this simply means that its code delay estimate adjusts according to the steady-state tracking error of the underlying EML discriminator, see Figure 3.1a for the corresponding multipath error envelope. The larger the final tracking error is, the longer it takes to converge to this new state.

The MMEKF, on the other hand, also has to adapt its CIR estimate to consider for the additional signal path. Figure 3.16a shows the estimated CIRs over time. As already discussed in Section 3.2, the consideration of the multipath in the CIR does not eliminate the effect of the multipath onto the code delay estimate entirely. Instead, the MMEKF converges to a slightly erroneous code delay estimate. This convergence test demonstrated that the MMEKF can quickly adjust to changes in the radio propagation path.

A crucial parameter for this convergence behavior is the process noise variance $\sigma_{Q,h}^2$ of the channel coefficients $h^{(l_h)}$, $l_h = -L_h, \dots, L_h$. In order to visualize that, Figure 3.16b illustrates the estimates of $h^{(2)}$, i.e., the channel coefficient that is closest to the appearing multipath with 30 m additional path delay, over different $\sigma_{Q,h}$. One can clearly see how too small values for $\sigma_{Q,h}$ slow down the convergence process while too large $\sigma_{Q,h}$ increase the estimation noise. The choice of $\sigma_{Q,h}$ effectively depends on the time variance of the radio propagation channel. For slower changing channel characteristics, $\sigma_{Q,h}$ can be reduced in order to take advantage of the better noise performance. For rapidly changing channels, higher $\sigma_{Q,h}$ are needed to quickly adapt to the new conditions.

These CIR estimation characteristics propagate to the code delay estimates. Figure 3.17a shows therefore the effect of different $\sigma_{Q,h}$ onto the tracking errors. Too small values for $\sigma_{Q,h}$, which prevent an immediate adjustment of the CIR, cause an increased overshooting, see Figure 3.17c. This is because the code delay estimates attempts to match the observed correlator outputs to the CIR which still represents the single-path case. The more the multipath is already accommodated for in the CIR, the more returns the code delay estimate to its steady-state value. With too large $\sigma_{Q,h}$, the noisier channel coefficient estimates propagate likewise to the code delay estimates. Figure 3.17b shows therefore the variance of the code delay estimates over $\sigma_{Q,h}$. The chosen value for $\sigma_{Q,h}$ of $10^{-3.3}$ depicts a good tradeoff between overshooting after propagation path changes and increasingly noisy estimates.

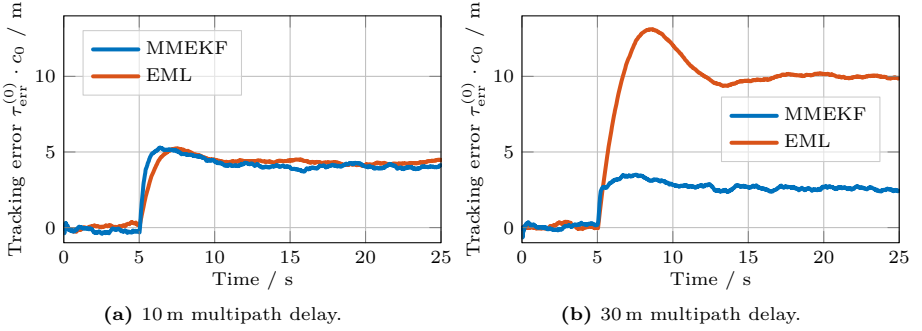


Figure 3.15: Illustration of the convergence behavior. After an initial 5 s of static zero Doppler LOS only conditions, a multipath with a 3 dB LOS to multipath to power ratio appears. The results illustrate how the code tracking algorithms adjust to the new propagation path conditions with respect to their code delay estimates.

3.4 Noise Performance

Besides the multipath performance and the dynamic response, the noise performance is another important criteria for a code tracking algorithm. Correspondingly, the competitiveness of the noise performance has been explicitly addressed by the first research question formulated in Section 1.3. In the following, we compare the proposed MMEKF with and a conventional DLL. The latter is implemented once with an EML discriminator and once with the multipath mitigating HRC. Therefore, a GNSS signal with a certain C/N_0 is tracked for 60 s. The STD of the resulting code delay estimates, under exclusion of the first 5 s as an initial convergence period, is determined and averaged over 20 Monte Carlo runs.

Figure 3.18 displays the results, which confirm the slightly inferior noise performance of the HRC, as already shown in [McG+99]. For the GPS C/A case, the STD curve has no values for C/N_0 s lower than 23 dB Hz, as the HRC-based DLL was unable to reliably track those signals below that threshold. The strong disturbances brought the tracking loop out of the operating range of the narrow S-curve of the HRC causing it to diverge. Consequently, the resulting STDs became excessively high. As those values would be misleading, diverged Monte Carlo runs were excluded. A run is considered diverged when the average tracking error exceeds 15 m. When the majority of Monte Carlo runs for a single C/N_0 value diverged, no code delay STD has been plotted.

For the MMEKF it turned out, that the noise performance is for high C/N_0 comparable to a conventional EML-based DLL. For low C/N_0 s, the MMEKF managed to outperform the conventional solution. This is because the EKF naturally relies more on its process model when the measurements are increasingly affected by noise. This leads to a stronger smoothing of the code delay estimates and therewith a lower STD. It is also expected to result in a slower step response. It can be concluded

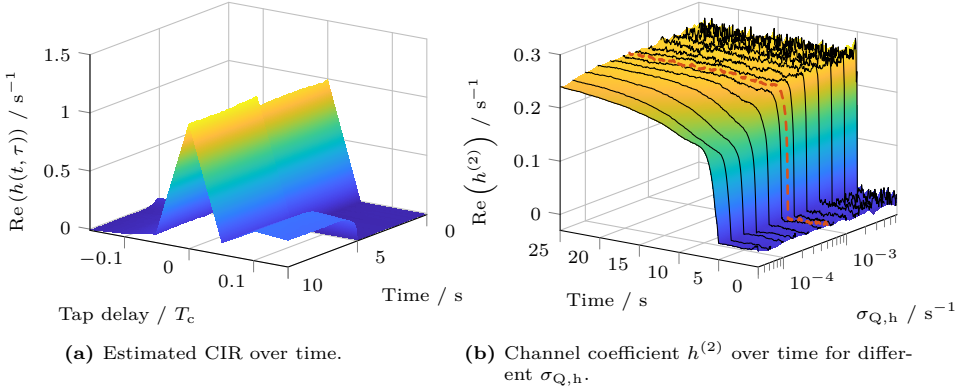


Figure 3.16: CIR estimate over time during arising multipath with 30 m delay. The estimates quickly adjust to the new conditions. The channel coefficient $h^{(2)}$, i.e., the closest one to the considered multipath delay, is shown separately for different process noise STDs $\sigma_{Q,h}$ in Figure 3.16b. While too small $\sigma_{Q,h}$ slow down the convergence process, too large $\sigma_{Q,h}$ increase the estimate noise. The chosen $\sigma_{Q,h}$ of $10^{-3.3}$ is highlighted by the dashed red line.

that the noise performance of the proposed MMEKF is indeed competitive and even outperforms other conventional approaches for low C/N_0 s, answering the first research question formulated in Section 1.3.

3.5 Initialization Robustness

An interesting aspect for an actual implementation is the robustness of the code tracking algorithm against initialization errors. This is especially crucial for the first tracking after a successful acquisition. Due to strict timing and processing constraints of real-time systems, the accuracy of the initial code delay estimate from the acquisition may be limited. The code tracking should ideally be able to handle such initial estimate errors by quickly converging to the actual value without losing the satellite again. In the following, we demonstrate that the proposed MMEKF is comparable to a conventional EML-based DLL in a simplified scenario with zero Doppler. Therefore, the code tracking algorithms are initialized on purpose with an erroneous code delay estimate. It is then observed how long it takes for the estimate to reach the ground truth. Convergence is assumed as soon as the code delay estimate remains below 2 m of error. The considered GPS C/A signals have a C/N_0 of 45 dB Hz. The MMEKF relied on a correlator bank with $N_{\text{corr}} = 7$ correlators. The results are illustrated in Figure 3.19 averaged over 20 Monte Carlo runs. If any of the Monte Carlo runs did not achieve to converge for a specific delay, no convergence time is shown for this value.

It turned out, that the proposed MMEKF is able to converge to the ground truth, even for very large initial errors, just like the EML-based solution. For completeness

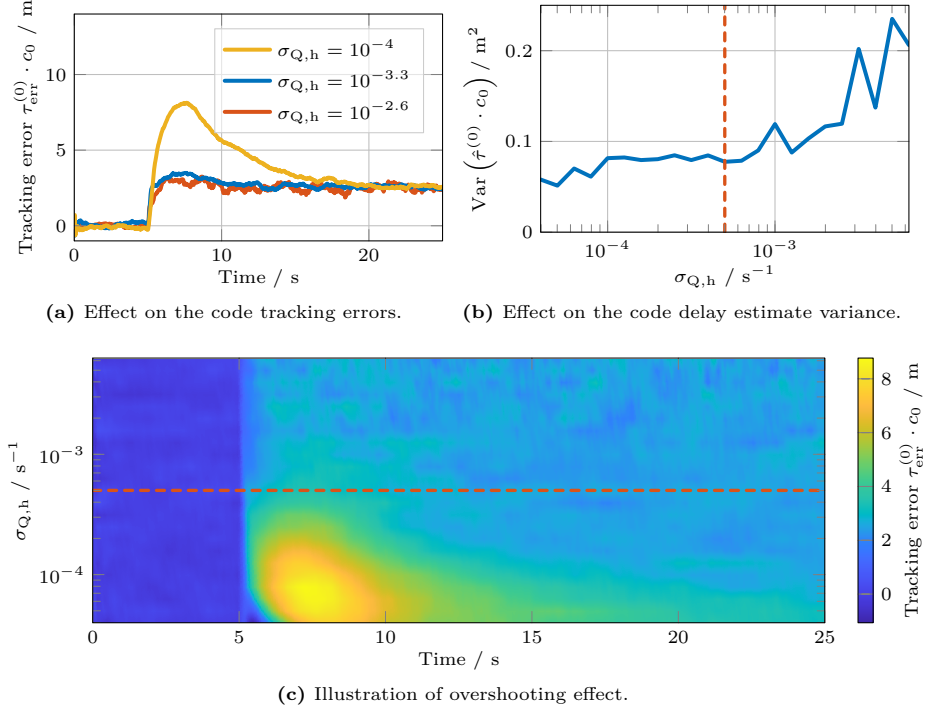


Figure 3.17: Effect of the process noise STD $\sigma_{Q,h}$ onto the code delay estimates. The shown results are for a multipath delay of 30 m. The choice of $\sigma_{Q,h}$ is a tradeoff between overshooting and increasingly noisy code delay estimates. The chosen $\sigma_{Q,h}$ is highlighted by the red dashed line in Figure 3.17b and 3.17c.

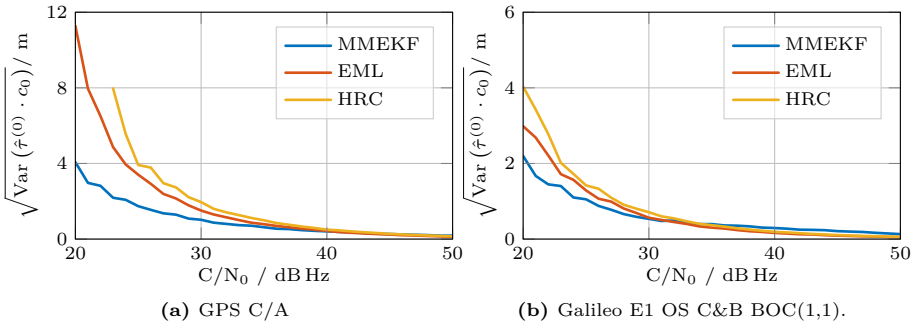


Figure 3.18: Noise performance of the proposed MMEKF against a conventional DLL with an EML discriminator and the HRC.

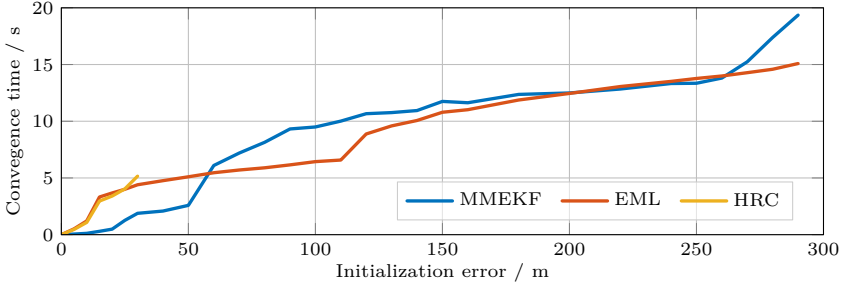


Figure 3.19: The robustness against initial code delay estimate errors is demonstrated. Illustrated is the convergence time of different code tracking algorithms for a certain initial code delay estimate error. Considered are GPS C/A signals.

the results with the HRC are also shown. For small initial code delay errors, it behaves similar to the EML discriminator. However, it has a narrower S-curve since its discriminator function is zero for delay errors larger than approximately 30 m with the selected correlator spacing. The HRC has therefore no chance to reliably converge to the ground truth with initial delay errors outside this range. In an actual implementation, one would typically rely on an EML discriminator with a larger bandwidth for the code loop filter to quickly converge during an initialization period. Once convergence is reached, one can then switch over to the HRC, avoiding its inferior initialization error robustness. Alternatively, one could also increase the correlator spacing for the HRC to obtain a larger operational range. For the MMEKF, a faster convergence can for example be achieved with higher process noise variances.

4 Vector Tracking Enhanced Multipath Mitigation

In Chapter 2, a multipath mitigation technique has been introduced, referred to as the multipath mitigating EKF (MMEKF). This technique has proven to be robust against multipath propagation, as shown with synthetic signals in the previous Chapter 3 and confirmed with more sophisticated simulations and actual measurements in Chapter 6. However, in real-world environments, multipaths are not the only threat for global navigation satellite system (GNSS) receivers. Especially in dense urban environments, the frequent blockage of line-of-sight (LOS) signals due to buildings, bridges, or other obstacles is common. It can lead to a shortage of available satellites and thus to a reduced position, velocity, and time (PVT) accuracy and availability [Bal+00]. Moreover, with a dominant multipath present during a LOS blockage, a conventional receiver might end up tracking said multipath instead of losing the satellite entirely. The same applies to the proposed MMEKF as it assumes that the LOS is the strongest signal path. This can cause large PVT errors if not detected by the receiver. A powerful approach to increase robustness in such environments is the use of vector tracking (VT) processing architectures [Spi+96, Chapter 7]. With VT approaches, satellites are not tracked individually followed by a separate PVT solution as with a conventional scalar tracking (ST) receiver. Instead, a central Kalman filter (KF) handles both jointly. Since the measurements derived from the satellite signals, i.e., code and carrier phase and Doppler, are interdependent and linked by the position solution, the joint processing of a VT architecture exploits this mutual information. Doing so also allows to keep blocked satellites in lock until they reappear using the measurements from the remaining visible satellites. In addition to that, this processing structure reduces the effect of individual multipaths. However, the more satellites are affected by multipath propagation, the larger becomes the final position error [Luo+14]. Thus, there is still need for a dedicated multipath mitigation, especially in urban canyons, as it has been done by, e.g., [Hsu13] before.

The third research question, formulated in Section 1.3, aims at the possible multipath mitigation improvements that can be achieved by such a joint processing. The author proposes in this chapter therefore the integration of the MMEKF into VT processing architectures. First of all, the general VT algorithm is described. Then, in Section 4.2, the integration of the proposed MMEKF is shown followed by a few notes on implementation related aspects in Section 4.3. In order to finally answer the third research question, Section 6.3 of the performance analysis Chapter 6 examines this proposed architecture with authentic simulations and actual measurement data in urban environments.

4.1 Vector Delay/Frequency Locked Loop Algorithm

In the following, the investigated VT structure is introduced. It is a vector delay/frequency locked loop (VDFLL) approach relying on a frequency locked loop (FLL)-assisted phase locked loop (PLL) [War98] for the carrier tracking. Therewith, not only the code tracking, but also the carrier frequency tracking is controlled centrally by the VT loop. Only the carrier phase is tracked individually using the PLL discriminator. The VT loop relies on an extended Kalman filter (EKF) to estimate the unknown user position and clock biases. Many implementations define for that the parameters as error states in the state vector [Cun+16]. However, the author estimates the absolute values as it has been done by [Shy+16] in order to be able to directly read out the user position and user clock errors. A general EKF description can be found in Section 2.2. In the following, only the VDFLL specific aspects are covered.

4.1.1 Process Model

For the process model, the state vector holding the parameters to be estimated must be first derived. For our purpose, it is set as follow

$$\mathbf{x}_k = [x_u, \dot{x}_u, y_u, \dot{y}_u, z_u, \dot{z}_u, \mathbf{t}_u, \dot{\mathbf{t}}_u]^\top \in \mathbb{R}^{N_{\text{st}} \times 1} \quad (4.1)$$

with $\vec{r}_u = [x_u, y_u, z_u]^\top$ and $\vec{v}_u = [\dot{x}_u, \dot{y}_u, \dot{z}_u]^\top$ being the user position and velocity defined in the Earth-centered, Earth-fixed (ECEF) coordinate system, respectively. Only the user's position and velocity are tracked by the state vector, as this is sufficient for most applications. For highly dynamic applications such as rocket launches, the inclusion of the user's acceleration may be considered. Such an extension is straightforward and is therefore not shown here. The user clock is parameterized with a clock bias and clock drift \mathbf{t}_u and $\dot{\mathbf{t}}_u$, respectively, as in [Bro+12, Chapter 9]. In order to consider for inter-system time offsets, one user clock bias per used GNSS is being tracked, thus, $\mathbf{t}_u = [t_{u,1}, \dots, t_{u,N_{\text{sys}}}] \in \mathbb{R}^{1 \times N_{\text{sys}}}$, where N_{sys} is the number of GNSSs that are being used. The process matrix, which describes the temporal evolution of the state vector in the process model from Equation (2.14), can be expressed as [Bar+01, Chapter 6]

$$\mathbf{A} = \text{diag}(\mathbf{A}_x, \mathbf{A}_y, \mathbf{A}_z, \mathbf{A}_{\text{clk}}) \quad , \quad \mathbf{A}_x = \mathbf{A}_y = \mathbf{A}_z = \begin{bmatrix} 1 & T_{\text{PVT}} \\ 0 & 1 \end{bmatrix} \quad (4.2)$$

with T_{PVT} being the PVT interval time and

$$\mathbf{A}_{\text{clk}} = \begin{bmatrix} \mathbf{I}_{N_{\text{sys}}} & T_{\text{PVT}} \mathbf{1}_{N_{\text{sys}}} \\ \mathbf{0}_{N_{\text{sys}}}^\top & 1 \end{bmatrix} \quad , \quad (4.3)$$

where $\mathbf{1}_q \in \mathbb{R}^{q \times 1}$ denotes a column vector of ones. The covariance matrix of the process noise is then given by [Bar+01, Chapter 6]

$$\mathbf{Q} = \text{diag}(\mathbf{Q}_x, \mathbf{Q}_y, \mathbf{Q}_z, \mathbf{Q}_{\text{clk}}), \quad (4.4)$$

$$\mathbf{Q}_x = \mathbf{Q}_y = \mathbf{Q}_z = \begin{bmatrix} T_{\text{PVT}}^4/4 & T_{\text{PVT}}^3/2 \\ T_{\text{PVT}}^3/2 & T_{\text{PVT}}^2 \end{bmatrix} \sigma_{\text{acc}}^2, \quad (4.5)$$

$$\mathbf{Q}_{\text{clk}} = \begin{bmatrix} (S_f T_{\text{PVT}} + S_g T_{\text{PVT}}^3/3) \mathbf{I}_{N_{\text{sys}}} & (S_g T_{\text{PVT}}^2/2) \mathbf{1}_{N_{\text{sys}}} \\ (S_g T_{\text{PVT}}^2/2) \mathbf{1}_{N_{\text{sys}}}^T & S_g T_{\text{PVT}} \end{bmatrix} \quad (4.6)$$

with $S_f = h_0/2$ and $S_g = 2\pi^2 h_{-2}$, where h_0 and h_{-2} are the Allan variance coefficients of the receiver's clock for clock errors in seconds [Bro+12, Chapter 9]. σ_{acc} is the process noise standard deviation (STD) for the user position. The initial state covariance matrix is given by

$$\mathbf{P}_{-1|-1} = \text{diag} \left(\sigma_{\text{P,pos}}^2, \sigma_{\text{P,vel}}^2, \sigma_{\text{P,pos}}^2, \sigma_{\text{P,vel}}^2, \sigma_{\text{P,pos}}^2, \sigma_{\text{P,vel}}^2, \sigma_{\text{P},t_u}^2, \mathbf{1}_{N_{\text{sys}}}^T, \sigma_{\text{P},t_u}^2 \right). \quad (4.7)$$

4.1.2 Measurement Model

The relationship between the measurements and the state parameters in \mathbf{x}_k is described with the measurement model, see Equation (2.15). For the considered VT EKF used here, which estimates the absolute position and velocity solution instead of relying on error states, the measurements are the sum of the pseudorange or pseudorange rate and the corresponding discriminator output. It can be expressed as

$$\mathbf{z}_{\rho,k} = \begin{bmatrix} \rho_k \\ \dot{\rho}_k \end{bmatrix} + \begin{bmatrix} \Delta \rho_k \\ \lambda \Delta \mathbf{f}_k \end{bmatrix} + \mathbf{u}_{\text{trk}} \in \mathbb{R}^{2N_{\text{sat}} \times 1}, \quad (4.8)$$

where

$$\rho_k = [\rho_{1,k}, \dots, \rho_{N_{\text{sat}},k}]^T, \quad \Delta \rho_k = [\Delta \rho_{1,k}, \dots, \Delta \rho_{N_{\text{sat}},k}]^T, \quad (4.9)$$

$$\dot{\rho}_k = [\dot{\rho}_{1,k}, \dots, \dot{\rho}_{N_{\text{sat}},k}]^T, \quad \Delta \mathbf{f}_k = [\Delta f_{1,k}, \dots, \Delta f_{N_{\text{sat}},k}]^T. \quad (4.10)$$

ρ_{l_s} and $\dot{\rho}_{l_s}$ are the pseudoranges and pseudorange rates and $l_s = 1, \dots, N_{\text{sat}}$ is the satellite index. $\lambda = c_0/f_c$ is the carrier wavelength. The code and carrier frequency discriminator outputs $\Delta \rho_{l_s,k}$ and $\Delta f_{l_s,k}$ are defined in meters and Hz, respectively. The measurement noise is modeled as a zero mean Gaussian random process $\mathbf{u}_{\text{trk}} \sim \mathcal{N}(\mathbf{0}_{2N_{\text{sat}}}, \mathbf{R}_k)$.

When combining different GNSS, the inter-system time offsets must be taken into account. The state vector in Equation (4.1) therefore contains one user clock bias for each GNSS. The minimal number of satellites in view required in order to ensure observability of the state parameters increases accordingly by one for each additional GNSS. When combining measurements from Global Positioning System (GPS) and Galileo satellites, an estimate of the inter-system time offset is provided by the Galileo navigation messages with the Galileo-GPS time offset (GGTO) [Eur21b, Chapter 5.1.8]. This parameter can be used as an additional measurement in the VT

EKF in order to aid the user clock bias estimation and reduce the number of required satellites in sight for an observable system down to only four again. According to [Eur21a, Chapter 3.5], the 95th percentile of the broadcast GGTO is specified to be below 20 ns. In practice, it turned out to fulfill the specification with 7.2 ns for the 95th percentile [Hah17]. Nevertheless, for a precise positioning, this is still a rather inaccurate estimate. In [Mel+20] it was shown that the use of the broadcast GGTO did not improve the position solution under open sky conditions, or even degraded it. On the other hand, with limited sky visibility, the additional measurement has a greater positive impact on the dilution of precision (DOP), so that it can, even with its limited accuracy, improve the position solution [Mel+20]. As this VT architecture has been developed with the motivation to improve positioning in challenging environments with limited sky visibility, the use of the broadcast GGTO can therefore be beneficial. For this reason, the broadcast GGTO is used as an additional measurement which is given by [Eur21b, Chapter 5.1.8]

$$z_{\text{to},k} = t_{\text{u},2} - t_{\text{u},1} + u_{\text{to}}, \quad (4.11)$$

assuming that $t_{\text{u},1,k}$ and $t_{\text{u},2,k}$ correspond to the user clock bias with respect to GPS and Galileo system time, respectively, at time step k . With $u_{\text{to}} \sim \mathcal{N}(0, \sigma_{\text{to}})$, the GGTO has been modeled to be zero mean and follow a Gaussian measurement noise with variance $\sigma_{\text{to}} = 3.67$ ns. The latter has been derived from the measured 7.2 ns 95th percentile by [Hah17]. z_{to} is provided alongside with $\mathbf{z}_{\rho,k}$ from Equation (4.8), leading to the full measurement vector

$$\mathbf{z}_k = \begin{bmatrix} \mathbf{z}_{\rho,k} \\ z_{\text{to},k} \end{bmatrix} = \mathbf{f}(\mathbf{x}_k) \in \mathbb{R}^{2N_{\text{sat}}+1 \times 1} \quad (4.12)$$

for the case where GPS and Galileo satellites are being combined. It should be noted, that $z_{\text{to},k}$ is an optional parameter that is only available from the navigation messages when using Galileo signals and only adds value when applied in combination with GPS signals. The covariance matrix of the measurement noise is then given by

$$\mathbf{R}_k = \text{diag}(\mathbf{R}_{\text{code},k}, \mathbf{R}_{\text{carr},k}, \sigma_{\text{to}}), \quad (4.13)$$

$$\mathbf{R}_{\text{code},k} = \text{diag}(\sigma_{\text{code},1,k}^2, \dots, \sigma_{\text{code},N_{\text{sat}},k}^2), \quad (4.14)$$

$$\mathbf{R}_{\text{carr},k} = \lambda^2 \text{diag}(\sigma_{\text{carr},1,k}^2, \dots, \sigma_{\text{carr},N_{\text{sat}},k}^2), \quad (4.15)$$

where $\sigma_{\text{code},l_s,k}^2$ and $\sigma_{\text{carr},l_s,k}^2$ are the noise variances of the code and carrier frequency discriminators, respectively. For $\sigma_{\text{code},l_s,k}^2$, one can rely on the open loop noise STD from [Mis+06, Chapter 10] for an early minus late (EML) discriminator which is given by

$$\sigma_{\text{code},l_s,k} = c_0 T_c \sqrt{\frac{\Delta_{\text{el}} T_c}{4 T_{\text{PVT}} C / N_0}} \quad (4.16)$$

for binary phase-shift keying (BPSK) signals, such as the GPS coarse/acquisition (C/A) code, where c_0 denotes the speed of light, Δ_{el} is the early-late correlator

spacing, and C/N_0 is the carrier-to-noise density ratio (C/N_0). For other signal modulations, such as the binary offset carrier (BOC) modulation of Galileo signals, the STD is inversely scaled according to the slope of the correlation triangle. Δ_{el} is the early-late correlator spacing in seconds. The pseudorange and pseudorange rates are related to the state parameters through [Kap+06, Chapter 2]

$$\rho_{l_s} = \|\vec{r}_{\text{sat}_{l_s}} - \vec{r}_u\| + c_0 t_{u,l_g}, \quad (4.17)$$

$$\dot{\rho}_{l_s} = \langle \vec{v}_{\text{sat}_{l_s}} - \vec{v}_u, \vec{a}_{l_s} \rangle + c_0 \dot{t}_u, \quad \vec{a}_{l_s} = \frac{\vec{r}_{\text{sat}_{l_s}} - \vec{r}_u}{\|\vec{r}_{\text{sat}_{l_s}} - \vec{r}_u\|}, \quad (4.18)$$

where $\vec{r}_{\text{sat}_{l_s}}$ and $\vec{v}_{\text{sat}_{l_s}}$ are the position and velocity vectors of the l_s -th satellite, respectively, \vec{a}_{l_s} is the unit LOS vector, and $l_g = 1, \dots, N_{\text{sys}}$ is the GNSS index. $\|\cdot\|$ depicts the Euclidean norm and $\langle \cdot, \cdot \rangle$ takes the inner product of two vectors. For a better readability, the time step indices k have been omitted in Equation (4.17) and Equation (4.18). The measurement model from Equation (4.12) must be linearized in order to apply the EKF equations, see Section 2.2.2. Therefore, the Jacobian matrix, see Equation (2.24), needs to be computed

$$\mathbf{J}_{f,k} = \left. \frac{d\mathbf{f}(\mathbf{x}_k)}{d\mathbf{x}_k} \right|_{\mathbf{x}_k = \hat{\mathbf{x}}_{k|k-1}} \in \mathbb{R}^{2N_{\text{sat}}+1 \times N_{\text{st}}} \quad (4.19)$$

with the required partial derivatives

$$\frac{d\rho_{l_s}}{d\vec{r}_u} = \frac{d\dot{\rho}_{l_s}}{d\vec{v}_u} = -\vec{a}_{l_s} \quad (4.20)$$

$$\frac{d\dot{\rho}_{l_s}}{dt_u} = c_0 \quad (4.21)$$

$$\frac{d\rho_{l_s}}{dt_{u,l_g}} = \begin{cases} c_0 & \text{when satellite } l_s \text{ is part of the } l_g\text{-th GNSS} \\ 0 & \text{when satellite } l_s \text{ is not part of the } l_g\text{-th GNSS} \end{cases} \quad (4.22)$$

$$\frac{dz_{\text{to},k}}{dt_{u,1}} = -\frac{dz_{\text{to},k}}{dt_{u,2}} = -1. \quad (4.23)$$

All remaining partial derivatives, that were not explicitly mentioned, are simply zero. This completes the description of the measurement model for the VT structure. Therewith, the EKF iteration can be conducted, as explained in Subsection 2.2.1 and Subsection 2.2.2.

4.1.3 Tracking Loop Closure

The algorithm described to this point determines a PVT solution based on pseudorange and pseudorange rate measurements using an EKF. In order to perform the transition from such a ST architecture to a VT one, the tracking loop needs to be closed from the position estimate all the way back to the satellite tracking. Therefore, the following correction parameters need to be calculated after each filter iteration

[Cun+16]

$$\Delta \mathbf{f}_{\text{code},k} = (\tilde{\rho}_{k|k} - (\rho_k - \hat{\rho}_{k|k})) \frac{1}{T_{\text{PVT}}} \quad (4.24)$$

$$\Delta \mathbf{f}_{\text{carr},k} = (\tilde{\dot{\rho}}_{k|k} - (\dot{\rho}_k - \hat{\dot{\rho}}_{k|k})) \frac{1}{\lambda}. \quad (4.25)$$

$\tilde{\rho}_{k|k}$ and $\tilde{\dot{\rho}}_{k|k}$ depict the pseudorange and pseudorange rate corrections corresponding to the state correction $\tilde{\mathbf{x}}_{k|k}$ determined with Equation (2.21). Equally, $\hat{\rho}_{k|k}$ and $\hat{\dot{\rho}}_{k|k}$ are the range and range rates corresponding to the updated state estimate $\hat{\mathbf{x}}_{k|k}$, see Equation (2.22). These values can be computed with

$$\begin{bmatrix} \tilde{\rho}_{k|k} \\ \tilde{\dot{\rho}}_{k|k} \end{bmatrix} = \mathbf{J}_{f,k} \tilde{\mathbf{x}}_{k|k}, \quad \begin{bmatrix} \hat{\rho}_{k|k} \\ \hat{\dot{\rho}}_{k|k} \end{bmatrix} = \mathbf{J}_{f,k} \hat{\mathbf{x}}_{k|k}. \quad (4.26)$$

The determined values for the code tracking $\Delta \mathbf{f}_{\text{code},k}$ can be used to directly update the code numerically-controlled oscillators (NCOs), no further filtering required. The code Doppler required for this can be computed from the VT filter results with

$$f_{\text{D,carr},l_s,k} = f_c \left(\sqrt{\frac{c_0 + \hat{\rho}_{l_s,k|k}}{c_0 - \hat{\rho}_{l_s,k|k}}} - 1 \right), \quad (4.27)$$

where f_c is the carrier frequency. $\Delta \mathbf{f}_{\text{carr},k}$ is used to replace the FLL discriminator output in the FLL-assisted PLL carrier tracking loop filters and controls with that the carrier NCOs.

4.1.4 Receiver Architecture

In Figure 4.1, the architecture of a VDFLL receiver is schematically illustrated as a block diagram. The radio frequency (RF) signal is fed into the structure from the left. A mixer down-converts the signal for each satellite using the carrier replicas provided by the carrier NCOs. The baseband signal undergoes then the correlation process to determine early, prompt, and late. The correlation is performed over T_{int} . Its outputs are used to determine the delay locked loop (DLL), FLL, and PLL discriminators. While the PLL discriminator output is directly fed into the FLL-assisted PLL loop filter, $\Delta f_{l_s,k}$ goes, as for $\Delta \rho_{l_s,k}$, to the VT filter. Due to the lower update rate of the VT filter which is $1/T_{\text{PVT}}$, the DLL and FLL discriminator outputs $\Delta \rho_k$ and $\Delta \mathbf{f}_k$ are integrated until the subsequent VT filter iteration. The navigation data processor uses the prompt correlator outputs as well as the code and carrier tracking results from the NCOs to decode the navigation data and determine the pseudorange and pseudorange rate estimates. These are then corrected by various correction parameters read from the navigation messages and provided to the VT filter as ρ and $\dot{\rho}$. The VT loop performs then one filter iteration and determines the control values $\Delta \mathbf{f}_{\text{DLL},k}$ and $\Delta \mathbf{f}_{\text{FLL},k}$. The latter is fed into the FLL-assisted PLL loop filter as a FLL discriminator output. The code correction parameters $\Delta \mathbf{f}_{\text{DLL},k}$ adjust the code NCOs, closing the tracking loops.

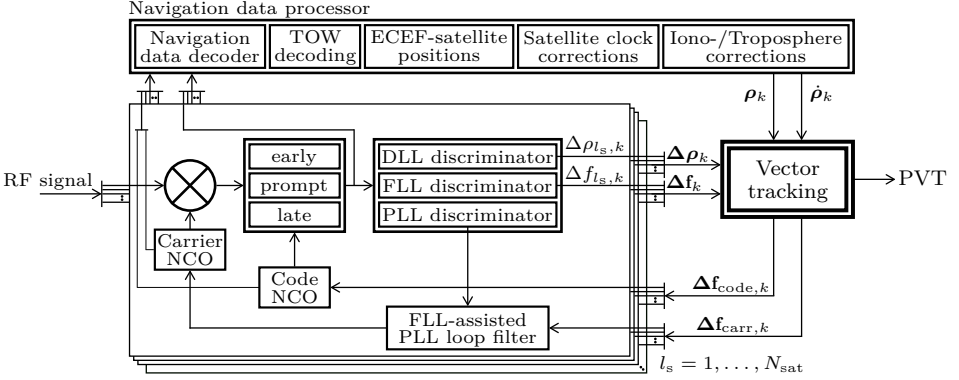


Figure 4.1: VDFLL receiver architecture.

4.2 Integration of Multipath Mitigating EKF

The above introduced VDFLL structure is extended in the following by a multipath mitigation component. We therefore use the by the author proposed MMEKF algorithm from Section 2.3. This has been initially proposed by the author in [Sie+22a]. By integrating this multipath mitigation technique into the VDFLL from above, an increased position accuracy in harsh multipath environments is aimed for. The required adjusted receiver architecture is explained in the following.

4.2.1 Receiver Architecture

In order to integrate the MMEKF into the VDFLL architecture from Figure 4.1, only a few adjustments are required. First of all, the early, prompt, and late correlators are replaced by the correlator bank $\mathbf{C}_{l_s, k}$ for the l_s -th satellite. Then, the DLL discriminator is substituted by the MMEKF. It is internally estimating the channel impulse response (CIR) as well as the code delay and Doppler $\tau_k^{(0)}$ and $\dot{\tau}_k^{(0)}$, respectively. However, to the VT loop, it only provides the state correction of the code delay $\tilde{\tau}_{l_s, k|k} = \hat{\tau}_{l_s, k|k}^{(0)} - \hat{\tau}_{l_s, k|k-1}^{(0)}$. It is treated by the VT filter as if it were the DLL discriminator output $\Delta \rho_{l_s, k}$. Thus, there is no adjustment required. While the MMEKF's prediction step is performed every T_{int} , the update step is only conducted every $T_{PVT} \geq T_{int}$ to match the VT interval. Correspondingly, the correlator bank outputs are integrated over T_{PVT} . The code correction parameters $\Delta \mathbf{f}_{DLL, k}$ do not only adjust the code NCOs, but are also returned to the individual MMEKFs, which use them to correct their internal code delay estimates $\hat{\tau}_{l_s, k|k}^{(0)}$. If no carrier-aiding is used, the internal code Doppler estimates are also adjusted according to the Doppler values obtained with the Equation (4.27).

skipped entirely and one only relies on the process model to propagate the state vector with the prediction step. With an insufficient number of measurements over an extended period of time, the VT filter may diverge with little chance of converging back to the ground truth. This results in excessive position errors and may lead to the effective loss of lock of all satellites, including the remaining visible ones. In order to avoid that, one should disable VT and revert to a conventional ST. This will result in the immediate loss of currently blocked satellites and likely no position solution at all. However, it allows to return to a reasonable PVT solution once enough satellites have been acquired again so that the VT filter can be reactivated. In order to detect the VT filter divergence in good time, we implemented a counter that is increased by one if no measurements were available and is decreased by one when there are enough valid measurements for an update step until it is zero again. When the counter reaches $N_{VT, \text{off}}$, the VT loop is disabled. The estimated inter-system time offset between GPS and Galileo, i.e., $\hat{t}_2 - \hat{t}_1$, has been used as an additional indicator for a diverged VT filter. If it deviates by more than 20 ns from the broadcast GGTO, the counter is also increased by one, even if enough measurements are available. Moreover, a large geometric dilution of precision (GDOP) over an extended period of time can also lead to a filter divergence despite a sufficient number of measurements. Therefore, the counter is also increased when the GDOP is larger than 20.

5 Estimation and Mitigation of Ionospheric Propagation Error

The Chapters 2 and 3 discussed a global navigation satellite system (GNSS) receiver with respect to its performance against multipath propagation as a major threat. Then, Chapter 4 aimed at resolving the arising difficulties with frequent line-of-sight (LOS) blockages under said threat of multipath propagation. However, there exists a second environmental condition that determines the accuracy of a position, velocity, and time (PVT) solution, namely the ionospheric total electron content (TEC). The ionosphere is a region in the Earth's upper atmosphere, located between about 50 km and 1000 km above sea level [Hof+01, Chapter 6]. There, particles are ionized by solar radiation. The free electrons of the resulting plasma depict a dispersive medium and affect the radio propagation of electromagnetic waves such as that of a GNSS signal, introducing a time of day, geographic location, solar activity, and direction of arrival (DOA) dependent carrier phase advance and group delay [Mis+06, Chapter 5]. Conventional single-frequency receivers, as they have been investigated in previous chapters, rely on ionospheric models to compensate for the latter, i.e., the additional code delay. Yet, with the most widely used Klobuchar model, the error is reduced only by 50% on average [Klo87]. In order to be able to actively estimate the ionospheric delays, a multi-frequency receiver is required. Therewith, the dispersive property can be exploited by observing the effect simultaneously on several frequencies. A common technique is the ionosphere-free combination [Hof+01, Chapter 6] to eliminate the dominating first order effect. However, this method has the drawback that other errors, such as multipath errors, tend to be amplified. The suppression of both sources of error must therefore be considered together in order to ensure optimum combined suppression.

The fourth research question formulated in Section 1.3 is aimed precisely at this difficulty. In order to address this question, this chapter extends the algorithm previously conceived only for multipath mitigation to include ionosphere estimation and correction.

5.1 Ionospheric Multipath Mitigating EKF

The algorithm for mitigating multipath effects from [Ili+17], on which the multipath mitigating EKF (MMEKF) is based, has already been extended to estimate the first order ionospheric effects in a previous publication, see [Ili+18]. In the following, the multi-frequency extension is derived for the MMEKF with an additional carrier range rate aiding for an increased robustness, as in [Sie+22b]. The derivation is based

on the multi-frequency signal model from Section 2.1. The ionospheric MMEKF (IMMEKF) depicts an extension to the single-frequency MMEKF from Section 2.3 with the major difference to operate now simultaneously on $N_{\text{band}} > 1$ frequencies per satellite in order to estimate the ionospheric TEC. While the correlator bank defined in Subsection 2.3.1 does not need to be adapted, the extended Kalman filter (EKF) state and measurement model must be partially reformulated.

5.1.1 Process Model

First of all, the state vector has to be extended to

$$\mathbf{x}_k = [\tau_{g,k}, \dot{\tau}_{g,k}, n_{e,k}, \dot{n}_{e,k}, \mathbf{h}_{1,k}^T, \dots, \mathbf{h}_{N_{\text{band}},k}^T]^T \in \mathbb{R}^{N_{\text{st}} \times 1} \quad (5.1)$$

with

$$\mathbf{h}_{j,k} = [\text{Re}(\tilde{\mathbf{h}}_{j,k}^T), \text{Im}(\tilde{\mathbf{h}}_{j,k}^T)]^T \in \mathbb{R}^{2N_{\text{tap},j} \times 1} \quad (5.2)$$

$$\tilde{\mathbf{h}}_{j,k} = [h_{j,k}^{(-L_{h,j})}, \dots, h_{j,k}^{(L_{h,j})}]^T \in \mathbb{C}^{N_{\text{tap},j} \times 1}, \quad (5.3)$$

where $N_{\text{st}} = 4 + 2 \sum_{j=1}^{N_{\text{band}}} N_{\text{tap},j}$ and $N_{\text{tap},j} = 2L_{c,j} + 1$. $\tau_{g,k}$ represents the geometric code delay in seconds between satellite and user with the geometric code Doppler $\dot{\tau}_{g,k}$. The state $n_{e,k}$ denotes the ionospheric TEC at time step k with its first derivative $\dot{n}_{e,k}$. It is given in TEC units (TECUs) with $1 \text{ TECU} = 10^{16} \text{ electrons/m}^2$. The TEC denotes the number of electrons integrated across a tube with one square meter cross section along the signal path. In contrast to [Ili+18], where the state vector holds the code delay of the first frequency band which allows to compute the delay of the second band, our approach has the advantage that defining appropriate process noise variances is more intuitive as LOS code delay dynamics and ionospheric dynamics are separated. Under consideration of the first order ionospheric model, see for example [Hof+01, Chapter 6], one can compose the effective code delay and Doppler for the j -th frequency band with

$$\tau_{j,k}^{(0)} = \tau_{g,k} + \frac{\alpha_I}{c_0 f_{c,j}^2} n_{e,k}, \quad \dot{\tau}_{j,k}^{(0)} = \dot{\tau}_{g,k}, \quad (5.4)$$

where c_0 is the speed of light. See [Har+84] for a detailed derivation of the conversion factor $\alpha_I = 40.3 \text{ m}^3/\text{s}^2$. The process matrix needs to be adjusted according to the new state vector to [Bar+01, Chapter 6]

$$\mathbf{A} = \text{diag} \left(\begin{bmatrix} 1 & T_{\text{int}} \\ 0 & 1 \end{bmatrix}, \begin{bmatrix} 1 & T_{\text{int}} \\ 0 & 1 \end{bmatrix}, \mathbf{I}_{N_{\text{st}}-4} \right) \in \mathbb{R}^{N_{\text{st}} \times N_{\text{st}}}, \quad (5.5)$$

which implements a constant velocity model for the geometric code delay and the ionospheric TEC. For the channel coefficients, the random walk model is maintained. The covariance matrix of the process noise is then obtained by extending Equation

(2.32), yielding the following block diagonal matrix

$$\mathbf{Q} = \text{diag}(\sigma_{\mathbf{Q},\tilde{\tau}_g}^2, \mathbf{Q}_{\tau_g}, \sigma_{\mathbf{Q},\tilde{n}_e}^2, \mathbf{Q}_{n_e}, \sigma_{\mathbf{Q},\tilde{h}}^2, \mathbf{I}_{N_{\text{st}}-4}) \in \mathbb{R}^{N_{\text{st}} \times N_{\text{st}}}, \quad (5.6)$$

$$\mathbf{Q}_{\tau_g} = \mathbf{Q}_{n_e} = \begin{bmatrix} T_{\text{int}}^4/4 & T_{\text{int}}^3/2 \\ T_{\text{int}}^3/2 & T_{\text{int}}^2 \end{bmatrix}. \quad (5.7)$$

The initial state estimate covariance matrix for the EKF initialization is then defined as

$$\mathbf{P}_{-1|-1} = \text{diag}(\sigma_{\mathbf{P},\tau_g}^2, \sigma_{\mathbf{P},\dot{\tau}_g}^2, \sigma_{\mathbf{P},n_e}^2, \sigma_{\mathbf{P},\dot{n}_e}^2, \sigma_{\mathbf{P},h}^2, \mathbf{I}_{N_{\text{st}}-4}) \in \mathbb{R}^{N_{\text{st}} \times N_{\text{st}}}. \quad (5.8)$$

5.1.2 Measurement Model

In contrast to the single-frequency MMEKF, an additional carrier range rate aiding has been proposed by the author in [Sie+22b]. Its purpose is to assist the EKF in its estimation process, reduce noise, and increase robustness. Therefore, the carrier Doppler estimates are used, provided by phase locked loop (PLL), to generate several additional measurements. The carrier range observable can be modeled as [Mis+06, Chapter 5]

$$\phi_{j,k} = \phi_{g,k} - \frac{\alpha_1}{c_0 f_{c,j}^2} n_{e,k} + \phi_{j,k,\text{err}} \quad (5.9)$$

with the geometric carrier range $\phi_{g,k}$ and different unknown error sources $\phi_{j,k,\text{err}}$ including constant integer ambiguities and multipath errors. While the latter can change rapidly with time, it is limited in amplitude to the carrier wavelength $c_0/f_{c,j}$. Correspondingly, for the carrier range rate $\dot{\phi}_{j,k}$, which is proportional to the carrier Doppler, $\phi_{j,k,\text{err}}$ it is negligible for most applications. The same applies for all static or quasi-static error contributions. Cycle slips, on the other hand, which lead to sudden jumps in the carrier ranges, must be monitored in order to exclude affected measurements. Following the ionosphere-free and geometric-free combination, the following additional measurements can be formed out of the carrier range rates [Mis+06, Chapter 5]

$$z_{j_1,j_2,k,\text{i-free}} = \frac{f_{c,j_1}^2 \dot{\phi}_{j_1,k} - f_{c,j_2}^2 \dot{\phi}_{j_2,k}}{f_{c,j_1}^2 - f_{c,j_2}^2} = \dot{\phi}_{g,k} = \dot{\tau}_{g,k}, \quad (5.10)$$

$$z_{j_1,j_2,k,\text{g-free}} = \frac{\frac{\dot{\phi}_{j_1,k}}{\alpha_1} - \frac{\dot{\phi}_{j_2,k}}{\alpha_1}}{\frac{1}{c_0 f_{c,j_2}^2} - \frac{1}{c_0 f_{c,j_1}^2}} = \dot{n}_{e,k}, \quad j_1, j_2 = 1, \dots, N_{\text{band}}, \quad j_1 \neq j_2. \quad (5.11)$$

Therewith, a direct measurement for the geometric code Doppler and the first derivative of the ionospheric TEC is obtained. The measurement variances of these new measurements can simply be derived from the measurement variance of the carrier

range rate $\sigma_{\phi_j}^2$ with

$$\sigma_{z_{j_1, j_2, \text{i-free}}}^2 = \frac{\sigma_{\phi_{j_1}}^2 f_{c, j_1}^4 + \sigma_{\phi_{j_2}}^2 f_{c, j_2}^4}{(f_{c, j_1}^2 - f_{c, j_2}^2)^2}, \quad \sigma_{z_{j_1, j_2, \text{g-free}}}^2 = \frac{\sigma_{\phi_{j_1}}^2 + \sigma_{\phi_{j_2}}^2}{\left(\frac{\alpha_{\text{I}}}{c_0 f_{c, j_1}^2} - \frac{\alpha_{\text{I}}}{c_0 f_{c, j_2}^2}\right)^2}. \quad (5.12)$$

The $N_{\text{comb}} = N_{\text{band}}(N_{\text{band}} - 1)/2$ new measurements and their measurement noise variances can be summarized as follows.

$$\mathbf{z}_{k, \text{i-free}} = [\dots, z_{j_1, j_2, k, \text{i-free}}, \dots]^T \in \mathbb{R}^{N_{\text{comb}} \times 1} \quad (5.13)$$

$$\mathbf{z}_{k, \text{g-free}} = [\dots, z_{j_1, j_2, k, \text{g-free}}, \dots]^T \in \mathbb{R}^{N_{\text{comb}} \times 1} \quad (5.14)$$

$$\mathbf{R}_{\text{i-free}} = \text{diag}(\dots, \sigma_{z_{j_1, j_2, \text{i-free}}}^2, \dots) \in \mathbb{R}^{N_{\text{comb}} \times N_{\text{comb}}} \quad (5.15)$$

$$\mathbf{R}_{\text{g-free}} = \text{diag}(\dots, \sigma_{z_{j_1, j_2, \text{g-free}}}^2, \dots) \in \mathbb{R}^{N_{\text{comb}} \times N_{\text{comb}}} \quad (5.16)$$

In order to embed the carrier range rate aiding into the MMEKF, the measurement model from Equation (2.34) must be augmented. This is done by simply appending the new measurements onto the measurement vector with

$$\mathbf{z}_k = [\mathbf{z}_{1, k}^T, \dots, \mathbf{z}_{N_{\text{band}}, k}^T, \mathbf{z}_{k, \text{i-free}}^T, \mathbf{z}_{k, \text{g-free}}^T]^T \in \mathbb{R}^{N_{\text{meas}} \times 1}, \quad (5.17)$$

where

$$\mathbf{z}_{j, k} = [\mathbf{z}_{j, 1, k}^T, \dots, \mathbf{z}_{j, N_{\text{sig}}, k}^T, z_{j, k, \text{constr}}]^T \in \mathbb{R}^{2N_{\text{corr}, j} N_{\text{sig}, j} + 1 \times 1}, \quad (5.18)$$

$$z_{j, i, k} = [\text{Re}(\tilde{\mathbf{z}}_{j, i, k}^T), \text{Im}(\tilde{\mathbf{z}}_{j, i, k}^T)]^T \in \mathbb{R}^{2N_{\text{corr}, j} \times 1}, \quad (5.19)$$

$N_{\text{meas}} = 2N_{\text{comb}} + \sum_{j=1}^{N_{\text{band}}} (2N_{\text{corr}, j} N_{\text{sig}, j} + 1)$ is the total number of measurements. The constraining measurement is now correspondingly defined for each band individually with

$$z_{j, k, \text{constr}} = \frac{\frac{1}{N_{\text{tap}, j} - 1} \sum_{l_{\text{h}}=-L_{\text{h}, j}}^{L_{\text{h}, j}} l_{\text{h}} \neq 0 \left| h_{j, k}^{(l_{\text{h}})} \right|^2}{\left| h_{j, k}^{(0)} \right|^2} \quad (5.20)$$

and remains therewith identical to the one from the single-frequency case in Equation (2.33). The measurement noise matrix is defined equally as

$$\mathbf{R} = \text{diag}(\mathbf{R}_{\mathbf{w}\eta_{C_1}}, \dots, \mathbf{R}_{\mathbf{w}\eta_{C_{N_{\text{band}}}}}, \mathbf{R}_{\text{i-free}}, \mathbf{R}_{\text{g-free}}) \in \mathbb{R}^{N_{\text{meas}} \times N_{\text{meas}}}, \quad (5.21)$$

$$\mathbf{R}_{\mathbf{w}\eta_{C_j}} = \text{diag}(\mathbf{R}_{\mathbf{w}\eta_{C_{j, 1}}}, \dots, \mathbf{R}_{\mathbf{w}\eta_{C_{j, N_{\text{sig}, j}}}}, \sigma_{\text{constr}}^2) \in \mathbb{R}^{2N_{\text{corr}, j} N_{\text{sig}, j} + 1 \times 2N_{\text{corr}, j} N_{\text{sig}, j} + 1} \quad (5.22)$$

$$\mathbf{R}_{\mathbf{w}\eta_{C_{j, i}}} = \text{diag}(\mathbf{R}_{\mathbf{w}\tilde{\eta}_{C_{j, i}}}/2, \mathbf{R}_{\mathbf{w}\tilde{\eta}_{C_{j, i}}}/2) \in \mathbb{R}^{2N_{\text{corr}, j} \times 2N_{\text{corr}, j}}. \quad (5.23)$$

The Jacobian matrix for the measurement model linearization, see Equation (2.24), is correspondingly given by

$$\begin{aligned} \mathbf{J}_{f,k} &= \left. \frac{d\mathbf{f}(\mathbf{x}_k)}{d\mathbf{x}_k} \right|_{\mathbf{x}_k=\hat{\mathbf{x}}_{k|k-1}} \in \mathbb{R}^{N_{\text{meas}} \times N_{\text{st}}} \\ &= \left[\frac{\partial \mathbf{f}(\mathbf{x}_k)}{\partial \tau_{g,k}} \quad \frac{\partial \mathbf{f}(\mathbf{x}_k)}{\partial \hat{\tau}_{g,k}} \quad \frac{\partial \mathbf{f}(\mathbf{x}_k)}{\partial n_{e,k}} \quad \frac{\partial \mathbf{f}(\mathbf{x}_k)}{\partial \hat{n}_{e,k}} \quad \frac{\partial \mathbf{f}(\mathbf{x}_k)}{\partial \mathbf{h}_{1,k}} \quad \cdots \quad \frac{\partial \mathbf{f}(\mathbf{x}_k)}{\partial \mathbf{h}_{N_{\text{band}},k}} \right] \bigg|_{\mathbf{x}_k=\hat{\mathbf{x}}_{k|k-1}}. \end{aligned} \quad (5.24)$$

The individual partial derivatives are shown in detail in Appendix B.

5.1.3 Receiver Architecture

In Figure 5.1 a multi-frequency GNSS receiver is illustrated with the proposed IMMEKF. From the left, the radio frequency (RF) signal is fed into the structure and for each band individually first of all down-converted. The therefore required carrier replicas are generated by the numerically-controlled oscillators (NCOs). The base-band signals $\mathbf{y}_{j,k}$ are then passed to the correlator banks $\mathbf{C}_{j,i}$, $i = 1, \dots, N_{\text{sig},j}$. The correlator outputs $\mathbf{z}_{j,i,k}$ as well as the carrier range rates from the PLLs across all N_{band} bands are fed provided to the IMMEKF to perform the code tracking and ionosphere estimation. In addition to that, the central correlator outputs, i.e., the prompts, are used by the PLL. In case of multiple signals per band, i.e., $N_{\text{sig},j} > 1$, the individual prompts are bit and phase corrected and subsequently averaged to reduce noise. The PVT solution is determined based on the geometric code delay estimate $\hat{\tau}_{g,k}$ without the need for an ionospheric correction. Last but not least, the IMMEKF state estimates are also used to adjust the correlator banks accordingly in order to close the tracking loops.

5.1.4 Hardware Imperfections

With the simultaneous processing of multiple frequencies, hardware imperfections regarding the signal transit times become relevant, more precisely their differences across different bands. Differences in signal transit times can emerge already at the transmitter side. Due to frequency-dependent antenna characteristics as well as different cables and filters implemented on the individual signal paths, signals may be broadcast with minor misalignments. These instrumental delays are referred to as the timing group delay (TGD) [Ant+22b]; [Ant+22a] or the broadcast group delay (BGD) for Galileo [Eur21b]. A correction parameter is broadcast in the navigation message to compensate for this effect [Ant+22b]; [Ant+22a]; [Eur21b]. Multi-frequency receivers relying on the ionosphere-free combination automatically cancel out these errors [Eur21b]. This is because the provided satellite clock correction parameters ensure that the BGD errors scale with frequency the same way the ionospheric delays scale. The same applies to the IMMEKF with its geometric code delay estimate $\tau_{g,k}$. Thus, no further considerations are required for the PVT solution. The ionospheric TEC estimate $\hat{n}_{e,k}$, on the other hand, will be offset. If one is interested in the actual

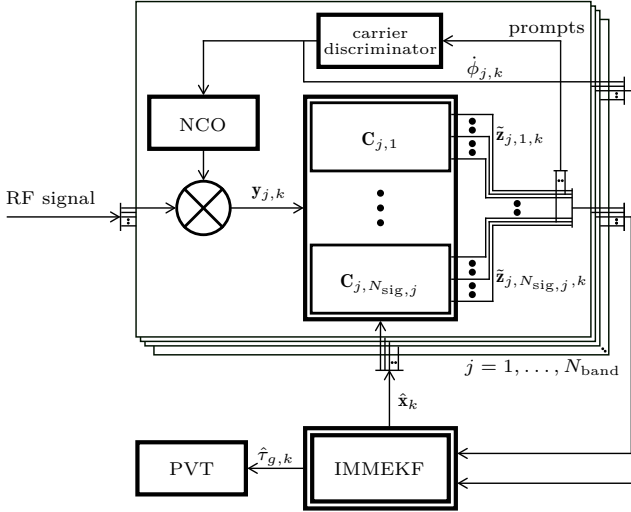


Figure 5.1: Proposed receiver architecture for IMMEKF.

TEC, a correction according to the broadcast TGD is required. Furthermore, on the receiver side, RF front ends and digitizers can introduce additional signal transit time differences. However, as they are common to all satellites, in contrast to TGDs, these errors will be absorbed by the user clock bias estimate in the PVT solution in a conventional receiver. The TEC estimate of the IMMEKF is also affected by these differential hardware delays. In order to get the actual TEC value, the common offset needs to be removed from all $\hat{n}_{e,k}$. This offset is in general unknown but can be measured for the specific hardware setup.

5.2 Summary

This chapter has been motivated by the fourths research question, which asked for a combined multipath mitigation and ionospheric delay estimation. Since multipath errors prevent an accurate elimination of ionospheric delays with state-of-the-art techniques, it was crucial to combine the suppression of both sources of error. With the MMEKF developed in Chapter 2, the additional ionospheric delay estimation is a natural extension and is achieved by extending the underlying EKF accordingly. An additional carrier range rate aiding has been proposed to assist the EKF in its estimation process and increase robustness. The obtained IMMEKF fulfills therewith the fourth research question. In the following chapter, the effectiveness of the proposed MMEKF and its extension the IMMEKF will be demonstrated.

6 Performance Analysis and Validation

In Chapter 3, the capabilities of the developed multipath mitigating EKF (MMEKF) has been demonstrated with synthetic signals. This included deriving multipath error envelopes, drawing comparisons with other well-known multipath mitigation methods, and investigating its dynamic behavior. The goal of this chapter is to verify the capability of the MMEKF with authentic global navigation satellite system (GNSS) signals. This will allow to observe the effect of the increased robustness against multipath of the MMEKF's code tracking in the positioning domain. Different realistic scenarios are simulated in Section 6.2 using a hardware GNSS emulator followed by an evaluation of an actual measurement campaign conducted in a suburban environment.

Then, in Section 6.3, the integration of the MMEKF into vector tracking (VT) loops from Chapter 4 is investigated. First, a challenging urban canyon scenario has been simulated to test this advanced tracking structure under controlled conditions. Then, a measurement campaign conducted in an urban environment has been evaluated. The results will answer the third research question formulated in Section 1.3, which concerned the performance improvements with the joint processing of several satellites.

Furthermore, the ionospheric MMEKF (IMMEKF) from Chapter 5, which extends the code tracking to multiple frequencies for the ionospheric total electron content (TEC) estimation, is examined in Section 6.4. This is done again with authentically simulated GNSS signals as well as actual measurement data. Before all that, the simulation and measurement setups are defined in the following.

6.1 Setup of Simulations and Measurements

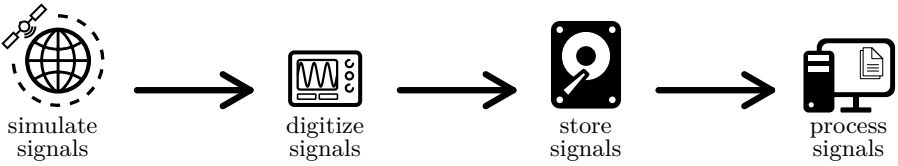
The simulation and measurement environments used for the testing below are defined. The parameters defined in Section 3.1 continue to be valid in this chapter, including sampling frequencies, signal bandwidths, and others. However, instead of using simple synthetic GNSS signals with no navigation data bits and zero Doppler, the signals considered in the following are fully authentic. Correspondingly, a carrier tracking loop can no longer be omitted. We implemented a conventional phase locked loop (PLL) relying on a two-quadrant ATAN Costas discriminator [Kap+06, Chapter 5] for the scalar tracking (ST) cases. The carrier loop filter is of third order with a bandwidth of 9 Hz. The integration time is set to 4 ms and navigation data bits were removed before integration. In case of multiple signals per band per satellite, e.g., data and pilot components as it is the case, among others, with the Galileo E1 Open Service (OS), the prompts of each signal are averaged under consideration of potential signal

phase offsets. The results of the carrier tracking loops are used for a carrier-aiding of the code tracking loops. For the VT cases, a frequency locked loop (FLL)-assisted PLL was employed as already explained in Section 4.1 using a second-order FLL assist. The position, velocity, and time (PVT) solution is determined in all ST cases with a simple snapshot-based least-squares algorithm where all available satellites are equally weighted. If not otherwise specified, the ionospheric delay is corrected according to the Klobuchar model. Moreover, tropospheric delays are modeled with the Hopfield model modified by Goad, see [Goa+74].

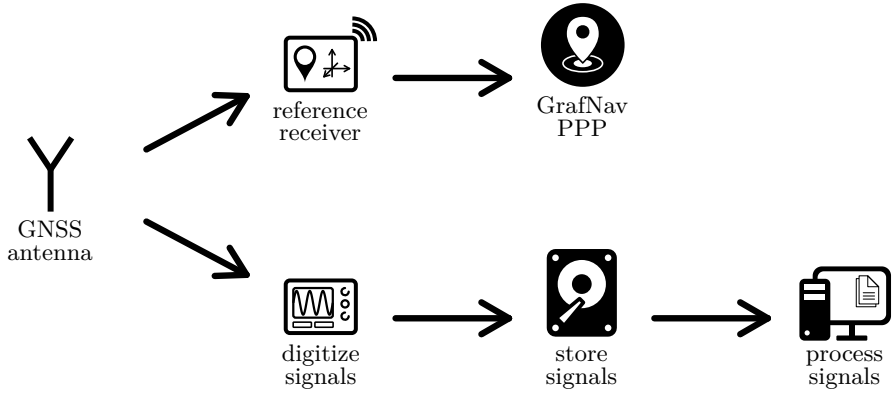
As discovered in Subsection 3.2.2, a correlator banks with a reduced number of correlators can still achieve a sufficiently good performance for the MMEKF. Therefore, the correlator banks used in this chapter rely only on $N_{\text{corr}} = 7$ correlators, unless otherwise specified, with a uniform correlator spacing of $\Delta_c^{(l)} = 0.05T_c$, $\forall l > 0$. The measurement noise variance σ_η^2 is determined based on the correlator output noise of a non-existing satellite that impinges with a carrier-to-noise density ratio (C/N₀) of 45 dB Hz, as described in [Sie+21b].

For the *hardware emulations*, GSS9000 series Spirent GNSS constellation simulators were used to generate authentic GNSS signals in real-time. With in-house developed radio frequency (RF) front ends [Hec+11], those signals were brought down to an intermediate frequency (IF) and were subsequently digitized and stored using a NI PXIe-51740 4-channel oscilloscope card. Figure 6.1a schematically illustrates the processing chain and a picture of the actual setup can be found in Figure 6.2. The recorded raw samples were processed using a software receiver. In order to reduce the time to first fix (TTFF), the broadcast ephemeris data was provided instead of extracting it from the navigation message during the processing. That means, no additional information was used for the processing and a real-time implementation would achieve the same results. The clocks of the front ends and the digitizer were synchronized with the one from the GNSS constellation simulator. The simulated satellite constellation of the conducted hardware emulations is shown in Figure 6.3. This hardware emulation with authentic signals from the constellation simulator allows to easily investigate the performance of different code tracking algorithms in a controlled environment.

For the *measurement campaigns*, an Antcom G8 antenna has been attached to the roof of a measurement vehicle while driving through the test environments. The measurement vehicle is shown in Figure 6.4. As for the simulator setup, the same front ends and NI PXIe-51740 4-channel oscilloscope card was used to digitize and subsequently store the antenna signal. A rubidium clock was used as a reference for the front ends and the digitizer. With a signal splitter, the antenna signal was simultaneously fed to the commercial NovAtel PwrPak7 receiver which has a built-in inertial measurement unit (IMU). The manufacturer's post-processing software GrafNav was used to process the obtained log files under consideration of precise point positioning (PPP) correction data. The determined PVT is used as a ground truth reference track, as discussed in Section 6.1.1. The measurement setup is shown in detail in Figure 6.5. In contrast to a hardware emulation in a controlled environment,



(a) Hardware emulations.



(b) Measurement campaigns.

Figure 6.1: Schematic illustrations of the different measurement setups.**Figure 6.2:** Setup for the hardware emulations. The racks of the Spirent GSS9000 series can be seen in the background. The generated RF signal is fed through the blue cable to the RF front end which sits on top of the digitizer with the NI PXIe-51740 4-channel oscilloscope card, i.e., the white machine on the bottom right.

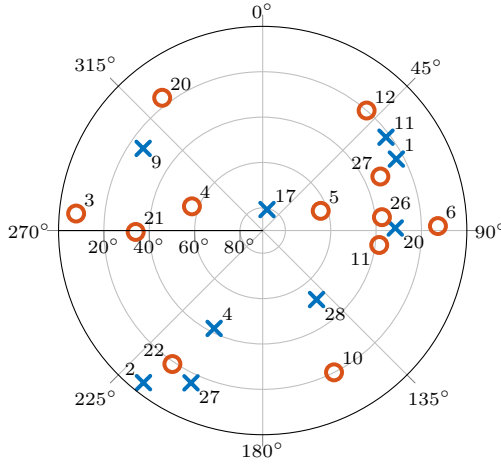


Figure 6.3: Satellite constellation during the hardware emulations as a sky plot. GPS and Galileo satellites are highlighted as crosses and circles, respectively.



Figure 6.4: Measurement vehicle.

the actual data allows to demonstrate the performance under real-world conditions at the cost of a limited knowledge about the environmental properties. For the processing, all available Global Positioning System (GPS) and Galileo satellites were used. In the L1 and E1 band, the GPS coarse/acquisition (C/A) code and the Galileo OS were tracked, respectively. Whenever available, both, the data and pilot signal components were used.

6.1.1 Ground Truth

In order to have a reference against which to compare the results obtained, a ground truth must be defined. This is easy for the hardware emulations, as the hardware emulator provides the ground truth data. Defining a reference trajectory for the

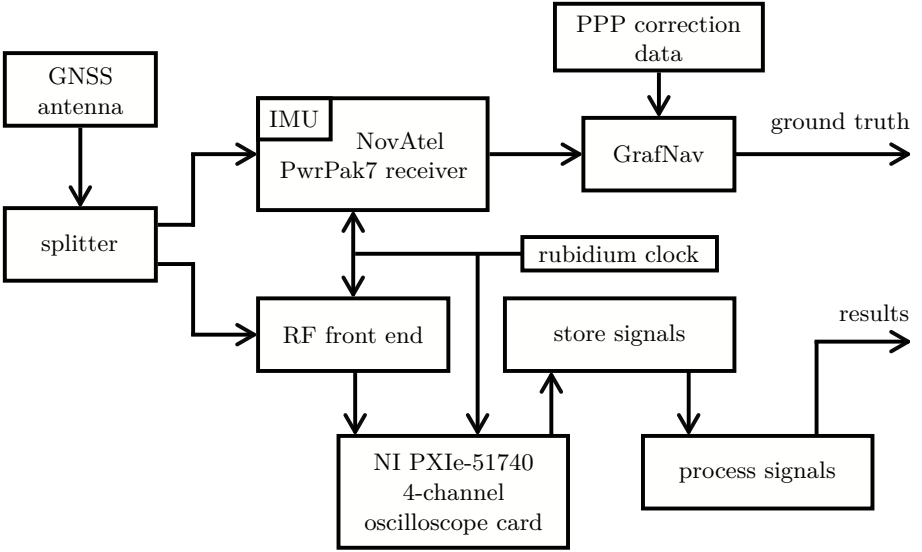


Figure 6.5: Detailed schematic illustration of the measurement setup.

measurement campaigns, on the other hand, is less straight forward. Ideal would be an accurate and independent measurement system, such as an external laser triangulation system [Don+15]. However, such a system is very impracticable to setup for larger areas, if not impossible for the large-scale suburban and urban measurement route carried out in see Sections 6.2.2 and 6.3.2, respectively. For this reason, a ground truth has been generated using the commercial NovAtel PwrPak7 GNSS receiver.

It may seem counterintuitive at first to compare GNSS position estimates to a ground truth that is also based on GNSS. However, the GNSS receiver for the ground truth trajectory operates on multiple frequencies across multiple GNSSs. This adds frequency diversity and improves the dilution of precision (DOP) with the increased number of satellites available. It also includes an IMU whose measurements are fused with the GNSS measurements. This improves positioning accuracy by overcoming short-term errors and bridging short GNSS outages. In addition, the manufacturer’s post-processing software GrafNav was used to process the resulting log files using a forward/backward smoothing under consideration of PPP correction data. This processing step goes beyond what a real-time solution could achieve, as the forward/backward filtering requires the measurements of the entire trajectory to be available, and the incorporated correction parameters only become available in retrospect. All these measures result in a very accurate and reliable reference trajectory, which is well suited as a ground truth for our position estimates.

6.2 Multipath Mitigating EKF

First of all, the base version of the proposed algorithm, the MMEKF of Section 2.3, will be tested in the following. This is done first as a hardware emulation in Subsection 6.2.1 using signals from the GNSS constellation simulator. Then, in Subsection 6.2.2, a measurement campaign conducted in a suburban environment is evaluated to demonstrate the real-world performance.

6.2.1 Hardware Emulation

With the hardware emulation, a simple static test is conducted. For the static scenario, the receiver tracks four GPS satellites using their L1 C/A signals. After around 50 s seconds, three of the four satellites are affected by a single static multipath each with a 3 dB line-of-sight (LOS) to multipath ratio. After around 50 s seconds, three of the four satellites are affected a single static multipath each. The multipath signals are attenuated by 3 dB with respect to the LOS and otherwise unaltered, i.e., they are in-phase with the LOS signal and have the same Doppler. The simulated satellite constellation is shown in Figure 6.3 and Table 6.1 lists details about the processed satellites and their multipaths.

Figure 6.6 shows the resulting position root-mean-square error (RMSE). The plots begin after 3 s which was the TTFF in this scenario. For the conventional early minus late (EML)-based code tracking, the errors increase abruptly to 13 m on average once the multipaths appear at approximately 50 s.

On the other hand, the proposed MMEKF with the full correlator bank consisting of $N_{\text{corr}} = 41$ shows no noticeable increase in position error. Its lower complexity variant with only $N_{\text{corr}} = 7$ leads to a mean steady-state error of 1.7 m. This is because the delays of the simulated multipath fall with 50 to 150 m into the region of the multipath error envelope, where the low complexity variant has a residual error, see Figure 3.4. With the high-resolution correlator (HRC), the appearing multipaths also do not affect the position RMSE. The direct comparison with the MMEKF cases confirm, however, its slightly inferior noise performance.

Moreover, Figure 6.7 illustrates the channel impulse response (CIR) estimates using the full $N_{\text{corr}} = 41$ correlators. The LOS signal is represented for each satellite by the central tap with the large peak. After 50 s, additional peaks arise for three out of the four satellites, representing the appearing multipath components. The simulated

Table 6.1: GPS satellite parameters of hardware emulation for MMEKF.

GPS satellite pseudorandom noise (PRN)	9	11	17	27
Multipath delay τ_{mul} / T_c	0.34	0.51	–	0.17
Multipath to LOS ratio / dB	–3	–3	–	–3
C/N ₀ / dBHz	43.37	43.34	44.86	43.18

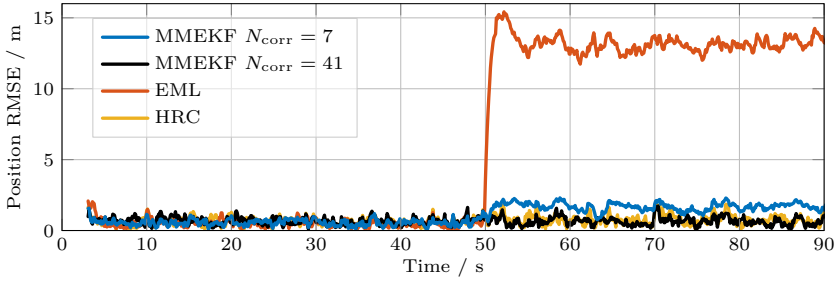


Figure 6.6: Position RMSE for the static scenario over time for three different receiver processing strategies: state of the art early minus late (EML), high-resolution correlator (HRC) and new multipath mitigating EKF (MMEKF). Three out of four tracked satellites are affected by multipath after 50s.

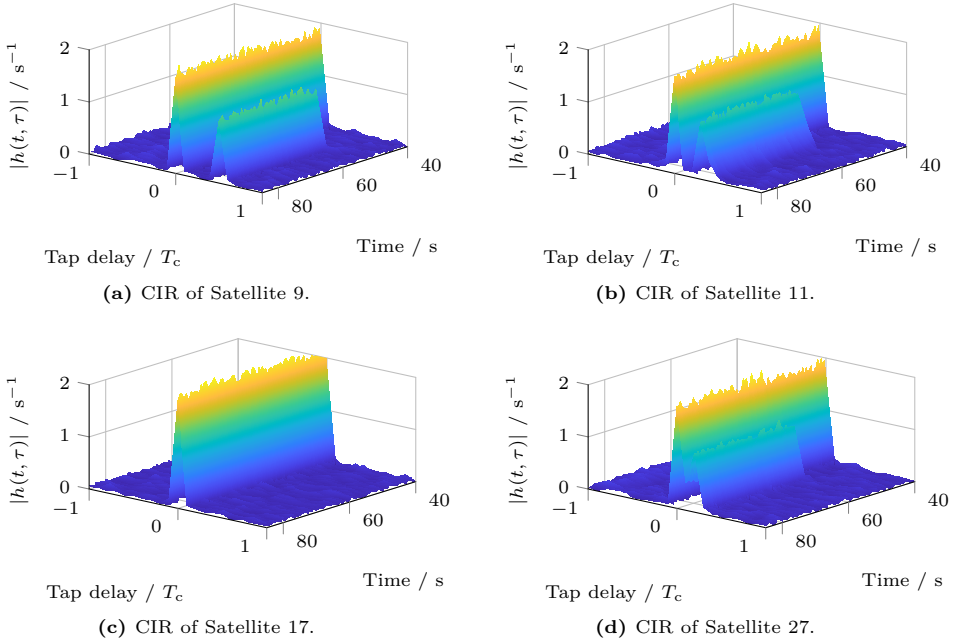


Figure 6.7: Estimated CIRs of the static scenario. The central peaks represent the LOS signal. Additional peaks arise from 50s onwards, representing the appearing multipaths. See Table 6.1 for the corresponding multipath delays.

3 dB LOS to multipath power ratio is not accurately reflected in the estimated CIRs. This is because the constraining measurement distorts the estimates in favor for a higher LOS channel tap amplitude and lower non-line-of-sight (NLOS) taps.

6.2.2 Suburban Measurement Campaign

In order to demonstrate the real-world performance of the proposed MMEKF, a measurement campaign has been conducted in Germering, near Munich, Germany. This campaign has been evaluated before in [Sie+23a]. The measurement vehicle drove through a variety of different environments, including suburban environments, short forest sections along rural roads, and highways. An overview of the entire route can be found in Figure 6.8. The sky plot in Figure 6.9 illustrates all acquired and tracked satellites. As already mentioned in Section 6.1, the PVT solution has been determined with a snapshot-based least-squares algorithm. An obtained position estimate has been rejected if the RMSE of the residual pseudoranges exceeded 3 m, the estimated time scale offset between GPS and Galileo deviated from the broadcast Galileo-GPS time offset (GGTO) by more than 20 ns, or the geometric dilution of precision (GDOP) exceeded a value of 20. Moreover, satellites require a minimal C/N_0 of 30 dB Hz to be considered in the PVT solution.

The 2D position RMSE as well as the altitude estimates of the entire campaign can be found in Figure 6.10. Despite the PVT estimate filtering based on residual pseudorange errors, DOP, and GGTOs as described above, multiple significant error peaks can still be found in the results. The first one around minute 2, which affected both code tracking algorithms equally, is due to a close pass of a multi-story building. With all satellites blocked from one side, the GDOP increases to around 11, causing the position estimate to deviate from the ground truth. Moreover, multiple bridge underpasses led to error peaks between 12 min and 16.5 min, including the overall largest peak at 16 min. Figure 6.11a illustrates in a 3D rendering the resulting position estimates for a few bridge underpasses. The errors occur for the first PVT estimates after the vehicle has passed the bridge. This is likely due to reflections from the bridge construction and affects therefore the conventional EML-based GNSS receiver to a larger extent. Last but not least, the large number of error peaks in the suburban section are due to numerous NLOS-only situations. Low elevation satellites are being blocked by buildings, while its multipath continues to persist. Both receiver algorithms begin to track the reflected signal replica, leading to erroneous pseudoranges (PSRs). Since the reflected signal is above the set C/N_0 threshold, the LOS blockage is not detected by the receiver, leading to the large position errors. Such a LOS blockage also caused the longer PVT outage around minute 24. The vehicle was waiting at a red light in an unfavorable position with buildings on both sides of the street, see Figure 6.11b. While the GPS satellites 2 and 4 were blocked, both receiver algorithms continued to track their persisting multipaths. The resulting PVT estimate exceeded the set Galileo GPS time scale offset, so that the estimates were rejected. As soon as the vehicle continues driving, the MMEKF and the EML-based tracking quickly lock back in with the reappearing LOS signals due

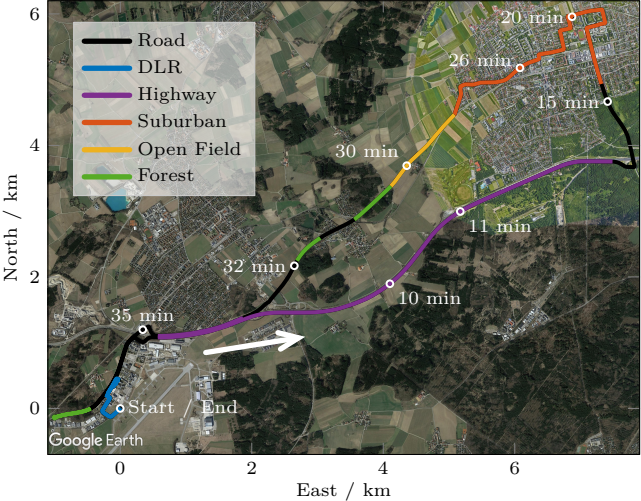


Figure 6.8: Route of the suburban measurement campaign. The background satellite image originates from Google Earth and the arrow indicates the direction of travel. The Deutsches Zentrum für Luft- und Raumfahrt (German Aerospace Center) (DLR) Oberpfaffenhofen site was start and endpoint of the campaign.

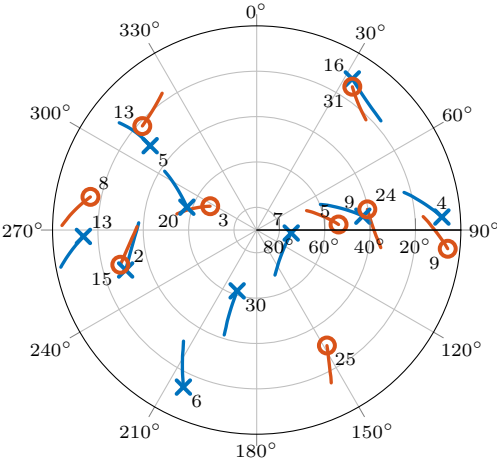


Figure 6.9: Satellite constellation during the entire suburban measurement campaign as a sky plot. PRN code numbers are indicated by the integers. The crosses and circles highlight the direction of arrivals (DOAs) of the GPS and Galileo satellites, respectively, at the end of the campaign at minute 42.

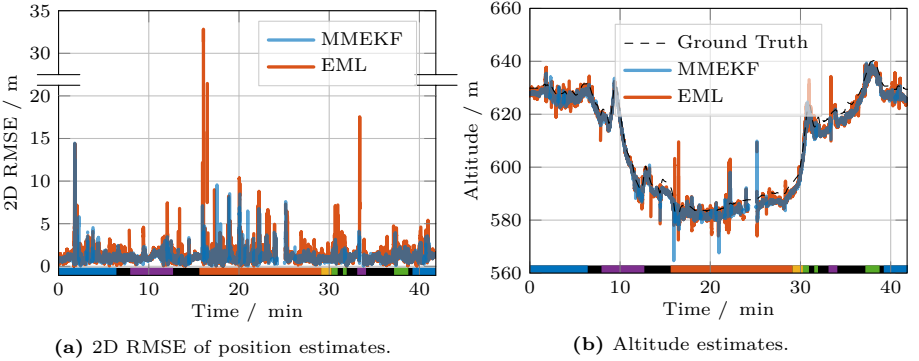


Figure 6.10: Results of the suburban measurement campaign. The time axes are colored according to the different route sections, see Figure 6.8.



(a) Bridge underpasses lead to error peaks, in particular for the EML case.



(b) Stopping between buildings with NLOS reception.



(c) Suburban section with NLOS reception around the corner.

Figure 6.11: Representation of the position estimates of the suburban measurement campaign in 3D renderings from Google Earth. The blue line shows the results with the MMEKF and the red one with a conventional EML-based DLL. The black line is the ground truth trajectory.

to their higher signal power compared to the reflected signal replicas. Such false locks during LOS blockages may be detectable using a receiver autonomous integrity monitoring (RAIM) algorithm [Par+96, Chapter 5], though high dynamics tend to complicate this process. Alternatively, one can also rely on advanced VT structures to overcome such situations, as it will be done in the following Section 6.3. A second noteworthy PVT outage can be found around minute 33. This is due to an extended tunnel section blocking all GNSS signals. In such an environment, only the use of additional sensors, such as wheel speed sensors, could help to overcome the complete signal outage.

In the altitude estimates in Figure 6.10b, a constant bias of approximately 2m can be observed between the estimates and the ground truth. This bias most likely originates from the circumstance, that for the ground truth trajectory, more accurate correction data was available in the post-processing, minimizing ionospheric and tropospheric errors, as well as satellite clock biases and orbital deviations. Factoring out the above explained error peaks and PVT outages, the position RMSE and altitude estimates unveil that on route parts with less severe multipath propagation, i.e., the highway sections or on open fields, both, the conventional EML-based GNSS receiver as well as the proposed MMEKF-based one perform comparable. When the multipath propagation intensifies, however, as it is for example the case in the suburban section, the higher multipath resilience of the MMEKF becomes apparent. In order to have a more detailed look at such multipath scenarios, two sections of the campaign are shown in detail in the following.

First of all, the very beginning of the measurement campaign is examined as it points out the typical difficulties in static multipath environments. Therefore, the altitude error is shown in Figure 6.12. The obtained oscillating error for the EML-based receiver is typical for such static multipath environments. The root cause is the low elevation Galileo satellite 8 that appears to have a strong multipath. The altitude estimates of the proposed MMEKF are not notably affected by that. Once the vehicle starts to move from 57s onwards, the multipath disappears, and both solutions provide comparable results.

Figure 6.13 shows one part of the suburban section in more detail. Buildings on alternating sides of the street cause considerable multipath propagation. With the higher multipath resilience of the proposed MMEKF, lower position errors were obtained compared to a conventional EML-based code tracking. The larger error peak obtained around minute 22.2 is due to another NLOS-only reception. Figure 6.11c illustrates this situation with a 3D rendering. The Galileo satellite 31 disappeared behind a building and both receiver algorithms start to track the remaining multipath signal until the satellite is lost entirely after all.

6.3 Vector Tracking Enhanced Multipath Mitigation

The integration of the proposed MMEKF into VT architectures has been proposed in Chapter 4. In the following, the capabilities of this strong combination of a multipath

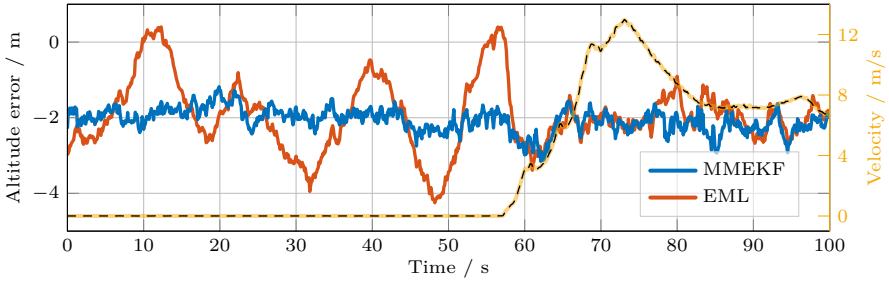
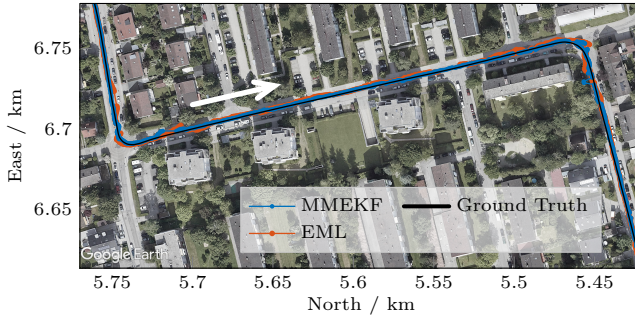
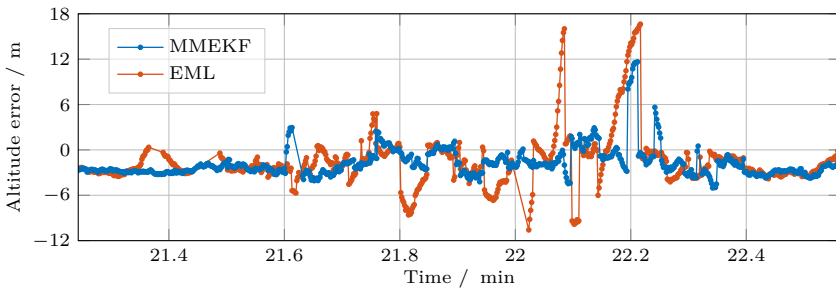


Figure 6.12: Altitude errors at the beginning of the suburban measurement campaign. The low elevation Galileo satellite 8 reaches the receiver via multiple paths during the initial static period, causing the EML-based solution to deviate from the ground truth while the MMEKF manages to provide good estimates. The vehicle velocity is given in orange.



(a) Position estimates.



(b) Altitude errors.

Figure 6.13: Position estimates and altitude errors from 21.24 to 22.57 min in the suburban route section. Residential buildings reflect signals from alternating sides of the street. They were causing the EML-based solution to deviate from the ground truth while the MMEKF mostly mitigates the effect of the additional signal replicas. The error peak around 22.2 min is caused by NLOS-only reception. The direction of travel is indicated with the arrow.

mitigation algorithm with the robust VT architecture are demonstrated. This is done first with a hardware emulation, simulating an urban canyon environment, and then with an actual measurement campaign in an urban environment in Subsection 6.3.2. In both cases, frequent LOS blockages occur in combination with strong multipath propagation, in order to challenge the advanced processing architecture accordingly. The measurement setups used were described in Section 6.1 and are identical to those already used in Section 6.2.

In both cases, the VT filter update interval was set to $T_{\text{PVT}} = 100$ ms. The C/N_0 threshold below which satellites are considered as concealed was set to 36 dB Hz, see Subsection 4.3.1. In order to prevent the divergence of the VT filter, it needs to be disabled when the environmental conditions are too challenging over an extended period of time. This mechanism is explained in detail in Subsection 4.3.2. The required counter threshold for this was set to $N_{\text{VT, off}} = 300$. This corresponds to a disabling of the VT after 30 s when at least one criteria is continuously exceeding its threshold. The process and measurement model parameters of the VT filter can be found in Table 6.2.

The code tracking begins in a ST mode. Once a sufficient number of satellites are tracked stably and a PVT solution has been found, it switches over to the VT architecture. In case the VT filter must be disabled, it falls back to ST until VT can be enabled again. The results show only the position estimates determined with VT enabled. These mechanisms are identical for the conventional vector delay/frequency locked loop (VDFLL) and the proposed integration of the MMEKF into the VT structure.

6.3.1 Simulated Urban Canyon

In order to demonstrate the capabilities of the VT architecture with the proposed integration of the MMEKF in a controlled environment, a challenging urban canyon scenario has been simulated with the constellation simulator. This hardware emulation has been conducted before in [Sie+22a]. A vehicle drove along a straight road northbound, passing by buildings on the right and left hand side. The vehicle stopped several times, simulating red lights at crossings. An overview of the simulated environment is given in Figure 6.14. On the roof of the vehicle, at an height of 1.5 m, the GNSS antenna is mounted. Initially, all satellites are visible and no multipaths are

Table 6.2: Parameters for VT EKF.

	User position			User clock		
Initial state STDs	$\sigma_{\text{P,pos}}$	=	1 m	σ_{P,t_u}	=	5 ns
	$\sigma_{\text{P,vel}}$	=	1 m/s	$\sigma_{\text{P},\dot{t}_u}$	=	5 ns/s
Process noise parameters	σ_{acc}	=	1 m/s ²	h_0	=	$2 \cdot 10^{-19}$
				h_{-2}	=	$2 \cdot 10^{-20}$

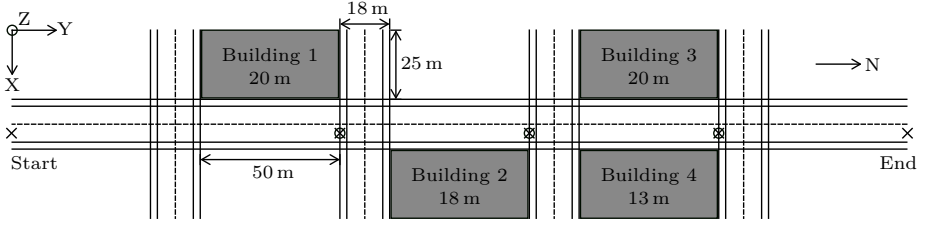


Figure 6.14: Illustration of the simulated urban canyon environment. A vehicle drives northbound, i.e., from the left to the right, along the straight road and stops at the three marked points at the crossings. The building heights are given by the meter specifications under the respective building numbers.

present, the vehicle velocity is zero. After 30 s the vehicle accelerates to its maximum velocity of 30 km/h until it reaches the end point, where it comes to a stop again. On its way it passes the four cuboid-shaped buildings with heights between 13 and 20 m. The buildings can block and reflect satellite signals. Their facades are simulated to be smooth non-magnetic lossy surfaces with a permittivity of $\epsilon_r = 5$ and a conductivity of $\sigma = 0.1 \text{ S}$ [Erc+06]. For simplicity it is assumed that only the street facing facades are reflecting satellite signals. Moreover, ground reflections are not considered. The simulated Doppler of the multipaths has been determined based on the vehicle and satellite velocity. The receiving GNSS antenna has an ideal isotropic characteristic and rejects left-hand circular polarization (LHCP) modes entirely. At each marked crossing, see Figure 6.14, the vehicles comes to a stop for 5 s. All accelerations are conducted within 5 s with a constant acceleration. The satellite constellation for this simulation can be found in Figure 6.3. Figure 6.15 illustrates the resulting number of visible LOS signals and currently active multipaths over time.

The resulting position estimates are illustrated in Figure 6.16. As expected, before the first building, when no multipaths are present, both solutions, i.e., the proposed integration of the MMEKF into a VT architecture and the conventional VDFLL, perform comparable. Once the vehicle passes the first building, multipaths appear and a few LOS signals are being blocked. The proposed solution remains basically unaffected by this. On the other hand, the conventional VDFLL starts to show first errors. However, due to the dominating number of remaining LOS signals, the overall error is small. This changes with the second building. Due to the closer distance to the building, the number of LOS signals goes down to only 6. Accordingly, the VDFLL struggles to mitigate the multipath effects and shows errors of up to 12.76 m. The errors jump back to lower values once a few LOS signals reappear. The proposed VT MMEKF also starts to show first errors, but manages to stay below a RMSE of 2 m. The final section of the simulation, between building 3 and 4, a similar result has been obtained. The conventional VDFLL shows errors of up to 3.88 m while the proposed solution hits only a maximal RMSE of 1.92 m. Once the vehicle is out of the zone of influence of the urban canyon, both solutions perform identical again.

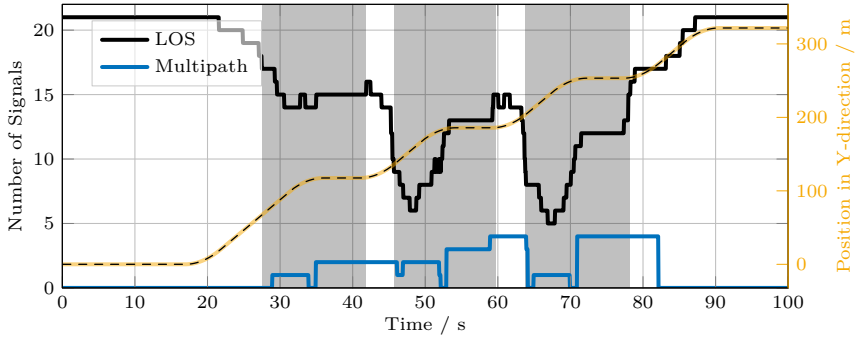
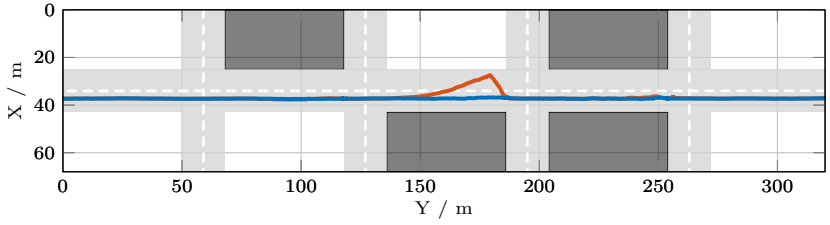


Figure 6.15: The number of visible LOS and active multipath signals during the urban canyon simulation plotted over time. Building passes are marked by the gray sections. The vehicle position in Y-direction is given by the orange line to facilitate the interpretation of the plots.

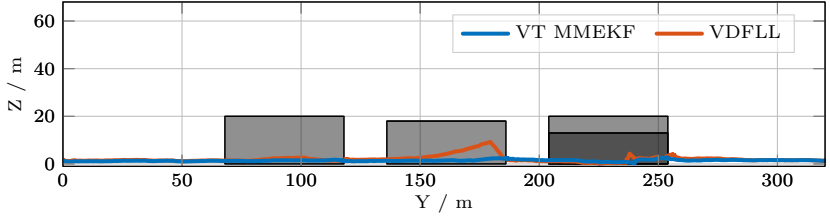
6.3.2 Urban Measurement Campaign

The results from the urban canyon simulation above will be verified with an actual urban measurement campaign in the following. Therefore, a measurement vehicle drove through the city center of Munich in Germany. This campaign has been evaluated before in [Sie+22a]. The route and the satellite constellation of all used satellites can be found in Figures 6.17 and 6.18.

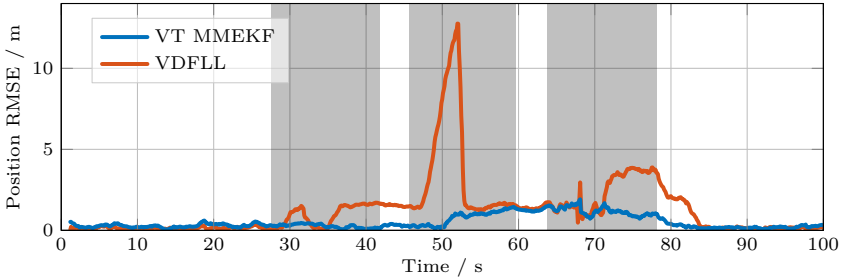
The plots in Figure 6.19 provide an overview of the position RMSE and the altitude estimates. The outcomes suggest that the proposed integration of the MMEKF into a VT architecture results in smoother estimates across the entire campaign, whereas the conventional VDFLL tends to show larger outliers. This distinction is especially notable in sections marked in orange, where the receiver encountered particularly challenging multipath conditions. In these situations, the conventional solution struggles notably due to the absence of a dedicated multipath mitigation. Around minute 27, the vehicle turned into an especially narrow urban canyon. As it was a dead end, the vehicle turned around. With the limited sky-view between the buildings, the majority of LOS signals were blocked. This allows the VT architecture to demonstrate its full potential. Blocked satellites are kept in lock until they reappear, avoiding time-consuming reacquisition processes. Nevertheless, the poor GDOP of the remaining visible satellites leads to larger position errors. In addition to that, multipath propagation due to reflective building facades introduce further errors. The latter is being mitigated to a greater extent by the proposed MMEKF leading to smaller position RMSEs. Towards the end of the campaign, around minute 37, another challenging situation arose. The vehicle had to wait at a red light next to a six-story building, see Figure 6.20b. This rather static multipath condition was particularly difficult for the conventional VDFLL relying on an EML discriminator. As multipath errors cannot average out over time, errors of up to 32.5m were obtained in this environment. The proposed solution on the other hand, relying on the



(a) Visualization of position estimates in a top view.



(b) Visualization of position estimates in a side view.



(c) Position RMSE plot where building passes are indicated by the gray areas.

Figure 6.16: Illustration of position estimates of urban canyon simulation.

MMEKF for a dedicated multipath mitigation, manages to keep errors significantly lower. Last but not least, there is a notable PVT outage between minute 14.1 and 15.1. This is due to a longer underpass followed by a red light at its end where only 6 satellites from a northwestern direction were received. With this poor GDOP, the VT filter was disabled to avoid a divergence, releasing the remaining visible satellites into the ST mode and requiring the reacquisition of the blocked ones. Such extended signal outages, as already discussed under Subsection 6.2.2, can only be overcome with additional sensors, such as wheel speed sensors or IMUs. Shortly after the VT is enabled again, the vehicle turns into another narrower urban canyon. The conventional VDFLL peaks here at an RMSE of 42.13 m at 15.6 min. On the other hand, the proposed solution is not exceeding a RMSE of 5 m in this situation once again due to its increased multipath resilience.

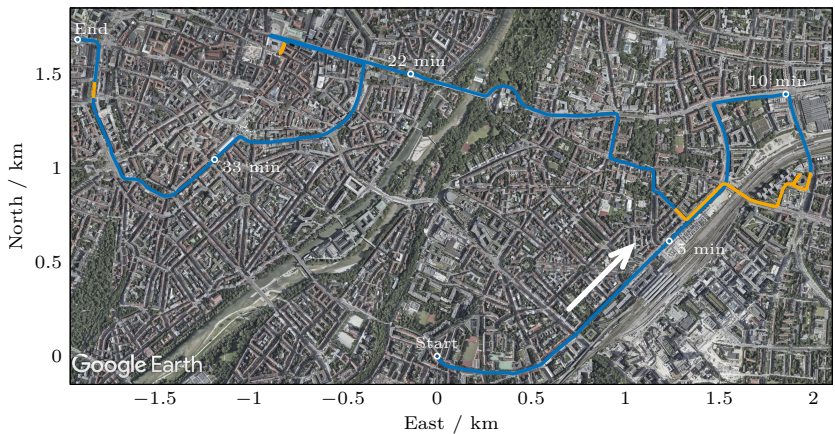


Figure 6.17: Route of the urban measurement campaign. The background satellite image originates from Google Earth and the arrow indicates the direction of travel. The orange stretches highlight particularly challenging passages.

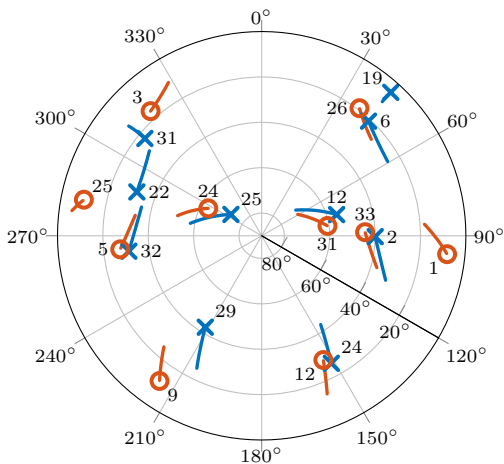


Figure 6.18: The satellite constellation during the entire urban measurement campaign as a sky plot. PRN code numbers are indicated by the integers. The crosses and circles highlight the DOAs of the GPS and Galileo satellites, respectively, at the end of the campaign at minute 38.

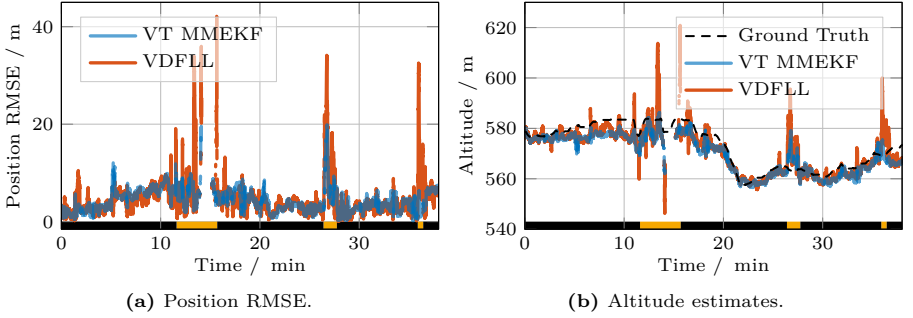


Figure 6.19: Results of the urban measurement campaign. Orange stretches indicate particularly challenging sections.



Figure 6.20: Representation of the position estimates of the urban measurement campaign in 3D renderings from Google Earth. The blue line shows the results with the VT MMEKF and the red one with the VDFLL. The black line is the ground truth trajectory. The static multipaths while stopping next to multi-story buildings lead to position errors.

With Figure 6.21, a more detailed view onto the first in orange highlighted challenging section is given. In this part, the vehicle passes several high-rise buildings and including a stop right next to one at a traffic light, see Figure 6.20a. Figure 6.21a shows the position estimates projected onto a satellite image. It unveils clearly, how the conventional VDFLL without a dedicated multipath mitigation deviates frequently from the ground truth. At the same time, the proposed solution provides more accurate position estimates. The altitude error plot in Figure 6.21b confirms that. In addition to that, it unveils a larger outlier around minute 13.4. This is where the vehicle was required to stop at the red light next to a multi-story building. As it was already the case at minute 37, the conventional VDFLL suffers in such a static multipath environment while the proposed integration of the MMEKF is significantly less affected by this condition as its measurement model considers for the additional signal replicas.

It can be concluded that the proposed integration of the MMEKF into VT ar-

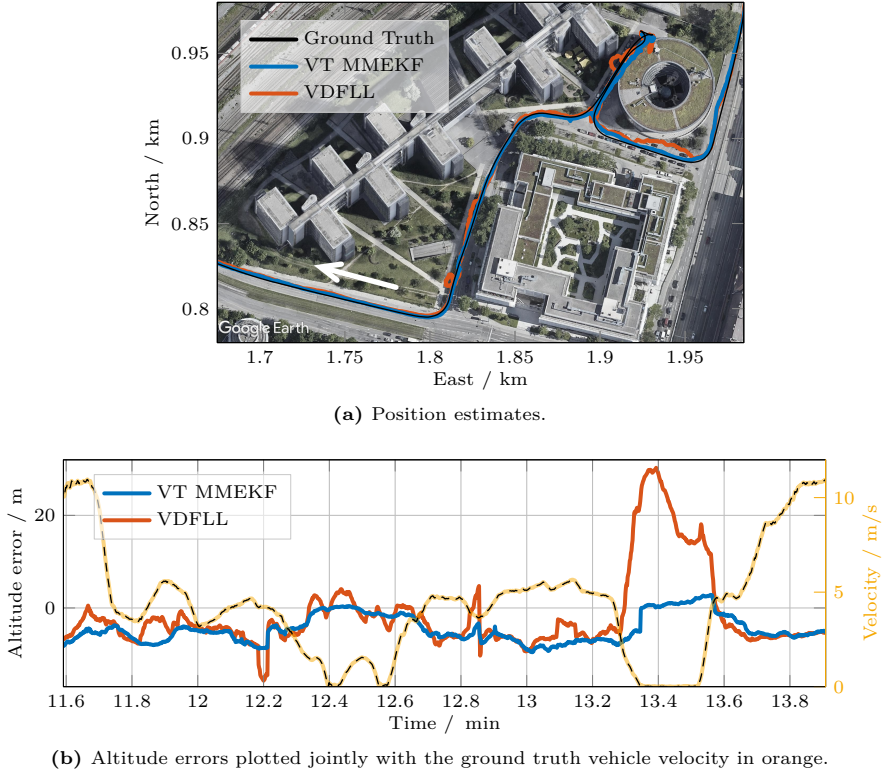


Figure 6.21: Position estimates and altitude errors of an exemplary section of the urban measurement campaign. Considerable multipath propagation is caused by high-rise buildings adjacent the street. The proposed solution shows smaller errors than the conventional VDFLL, especially during the extended static period around 13.4 min.

chitectures comes along with an improved multipath resilience when compared to a conventional VDFLL, which answers the third research question formulated in Section 1.3.

6.4 Ionospheric Multipath Mitigating EKF

Chapter 5 proposed the extension of the MMEKF to a multi-frequency processing. This allows for the active estimation of the ionospheric TEC and was thus referred to as the IMMEKF. The active estimation of the ionospheric delay dissolves the dependency on ionospheric models, such as the simple Klobuchar model as the use of ionospheric models can lead to erroneous corrections, as we have for example seen with the suburban measurement campaign in Subsection 6.2.2. The IMMEKF

is analyzed first using synthetically generated signals. Then, in Subsection 6.4.2, a hardware emulation has been conducted. Finally, actual measurement data has been processed in Subsection 6.4.3 to demonstrate the performance under real-world conditions. The signals used for the analysis were the Galileo E1 OS as well as the Galileo E5a band, each using both, data and pilot components. It follows that $N_{\text{band}} = 2$ and $N_{\text{sig},j} = 2$, $j = 1, 2$. GPS satellites were not considered as the deployment of L5 satellites has not been completed yet. The correlator bank for the E1 band uses $N_{\text{corr},1} = 7$ correlators, as defined in Subsection 6.1. For the E5a band, due to the higher chip rates, we used only $N_{\text{corr},2} = 5$ correlators with the same equal spacing of $\Delta_{c,2}^{(l)} = 0.05T_{c,1}$, $l > 0$. As for the IMMEKF, the latest results from the EML-based tracking were used to initialize the IMMEKF. This includes the initial geometric delay and Doppler $\hat{\tau}_{g,-1|-1}$ and $\hat{\tau}_{g,-1|-1}$, respectively, and the initial ionospheric TEC estimate $\hat{n}_{e,1|-1}$. The initial ionospheric TEC rate is simply set to $\hat{\dot{n}}_{e,1|-1} = 0$. Further IMMEKF specific parameters can be found in Table 6.3. If not otherwise specified, the in Subsection 5.1.2 proposed carrier range rate aiding has been enabled. The IMMEKF is primarily compared with a conventional dual-frequency GNSS receiver. It relies on a EML-based delay locked loop (DLL) and the well-known ionosphere-free combination to eliminate the ionospheric delays. The E5a early-late spacing is set to $0.5T_{c,2}$. While the ionosphere-free combination eliminates the first-order ionospheric delays entirely, it tends to amplify the noise from the individual bands and other errors such as multipath, as shown in the following subsections.

6.4.1 Synthetic Signals

First of all, a simple scenario has been simulated with synthetically generated signals, to demonstrate the basic functionality of the proposed IMMEKF. Therefore, a single geostationary satellite was assumed, broadcasting Galileo E1 and E5a signals. The receiver, located statically on the ground, received the LOS signal with 48.61 dB Hz and correspondingly zero Doppler. The ionosphere was simulated to have a TEC of 50 TECU. A single in-phase multipath arose after 120 s on all bands with an additional path delay of 50 m and 3 dB LOS to multipath power ratio. The evaluation of this synthetic scenario has been done before in [Sie+22b].

Table 6.3: IMMEKF specific parameters.

	Initial state covariance $\mathbf{P}_{-1 -1}$	Process covariance matrix \mathbf{Q}
Geometric code delay τ_g	$\sigma_{P,\tau_g} = 0.01T_{c,1}$ $\sigma_{P,\dot{\tau}_g} = 0.01 T_{c,1}/s$	$\sigma_{Q,\ddot{\tau}_g} = 0.02 T_{c,1}/s^2$
TEC n_e	$\sigma_{P,n_e} = 5 \text{ TECU}$ $\sigma_{P,\dot{n}_e} = 1 \text{ TECU}/s$	$\sigma_{Q,\ddot{n}_e} = 0.5 \text{ TECU}/s^2$
CIR \mathbf{h}	$\sigma_{P,h} = 0.05/s$	$\sigma_{Q,h} = 10^{-3.3}/s$

Figure 6.22 shows the ionospheric TEC estimates \hat{n}_e . While the estimates quickly converge towards the ground truth of 50 TECU, the arising multipath introduces from 120 s onwards a small error of approximately 1.3 TECU.

The code delay error is illustrated in Figure 6.23. It compares the results obtained with the proposed IMMEKF with a conventional dual-frequency receiver using the ionosphere-free and an EML-based DLL. For the latter, the code delay errors of each band individually were also plot. At this stage, the ionospheric delay has not yet been eliminated. Thus, those estimates are biased according to the simulated 50 TECU. The lower carrier frequency of E5a has accordingly the higher bias. The arising multipath introduces further errors for the E1 case. As the multipath is delayed by 50 m, the single-frequency E5a tracking is not affected by this since the multipath correlation triangle is already zero at the early and late correlators. After applying the ionosphere-free combination, the effect of the ionosphere has been eliminated. However, the arising multipath causes a significant increase in error to more than 20 m. The IMMEKF case achieves equally the complete elimination of the ionospheric delays. The difference is though, that the appearing multipath barely affects the code delay due to the multipath mitigating capability of the proposed solution. This is a key advantage of combining the MMEKF and the ionospheric TEC estimation. The fourth research question, which asked for an extension to ionospheric delay estimation while maintaining multipath mitigation capabilities, has thus been fully addressed. In addition to that, its estimate variance is significantly lower than the one from the ionosphere-free combination.

6.4.2 Hardware Emulation

After the simple simulation conducted above, the results are verified with a hardware emulation in the following. Therefore, the constellation simulator was set up to simulate a static receiver at 48°N and 11°E with an altitude of 550 m. After an initial LOS-only period, static multipaths appear after 45 s. For the processing, four Galileo satellites were selected. The satellite constellation can be found in Figure

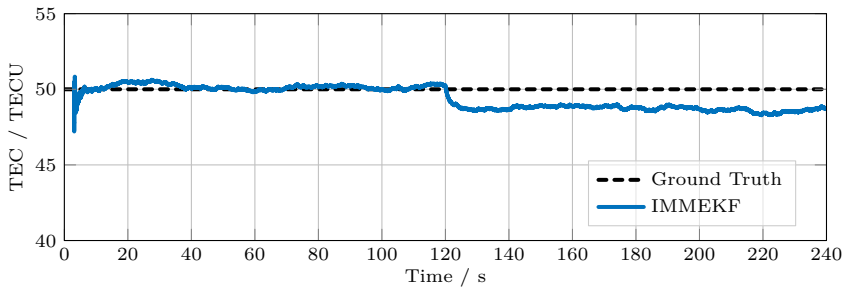


Figure 6.22: Ionospheric TEC estimate \hat{n}_e using synthetic signals. It quickly converges to the true value of 50 TECU. From 120 s onwards, the arising multipath causes a bias.

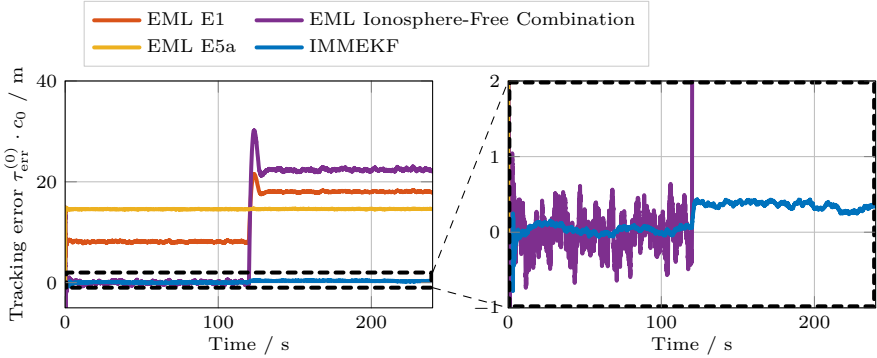


Figure 6.23: The tracking errors obtained for the IMMEKF and a conventional dual-frequency receiver using the synthetically generated signals. For the latter, the individual band-wise tracking results are additionally shown. As no ionospheric delay has been eliminated yet, those estimates are biased. The emerging multipath introduces additional errors from 120 s onwards.

6.3. Details about the satellites and their multipaths can be found in Table 6.4. The constellation simulator relied on the Klobuchar model to simulate the ionospheric delays. This hardware emulation has been evaluated before in [Sie+22b].

The resulting position RMSE can be found in Figure 6.24. Both, the ionosphere-free combination and the proposed IMMEKF manage to provide a bias-free position estimate during the initial multipath-free period. The appearing multipath leads to a RMSE of 22.5 m for the conventional dual-frequency receiver, as no dedicated multipath mitigation is performed and the ionosphere-free combination further amplifies multipath errors. The proposed IMMEKF on the other hand stays below a position error of 3 m. The additional carrier range rate aiding further smooths the estimates and also holds the IMMEKF back from converging too quickly to the multipath induced bias. As in the simulation above, the noise performance of the IMMEKF, with or without the additional carrier range rate aiding, outperforms the results from the ionosphere-free combination.

In addition to that, the TEC estimates \hat{n}_e of the IMMEKF are shown in Figure

Table 6.4: Satellite and multipath parameters of hardware emulation for IMMEKF.

GNSS	PRN	Multipath delay	Multipath to LOS ratio	C/N ₀ E1	C/N ₀ E5a
Galileo	5	–	–	47.43 dB Hz	52.97 dB Hz
Galileo	6	150 m	–3 dB	46.85 dB Hz	51.78 dB Hz
Galileo	20	100 m	–3 dB	47.35 dB Hz	51.93 dB Hz
Galileo	22	50 m	–3 dB	47.21 dB Hz	51.95 dB Hz

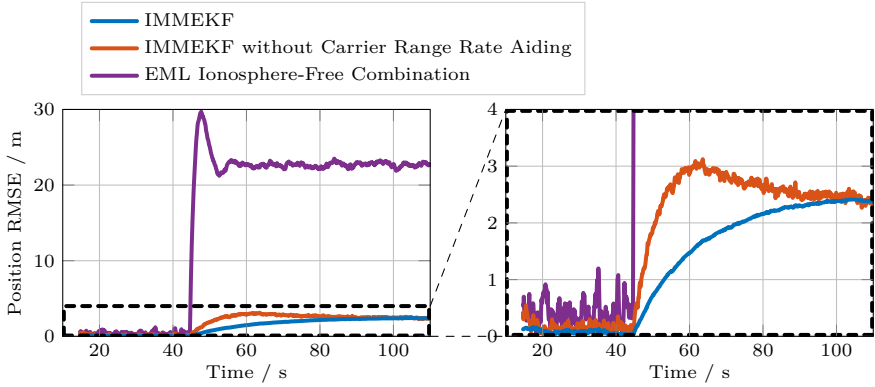


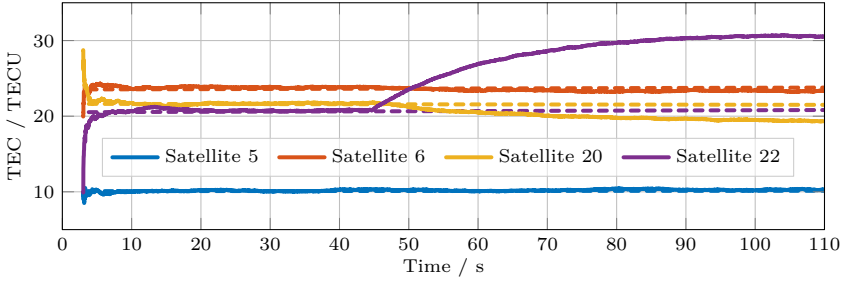
Figure 6.24: Position RMSE using a multi-frequency processing of hardware emulation. The after 45 s arising multipaths lead to positioning errors. Significantly noisier estimates were obtained with the ionosphere-free combination.

6.25. After a short initialization phase, the estimates quickly converge towards the ground truth. The arising multipaths induce errors again, in this case of up to 10 TECU which corresponds to 1.6 m for the E1 band. Moreover, the carrier range rate aiding clearly smooths the TEC estimates and, as in the position estimate domain, prevents the IMMEKF from converging too quickly towards the multipath induced bias.

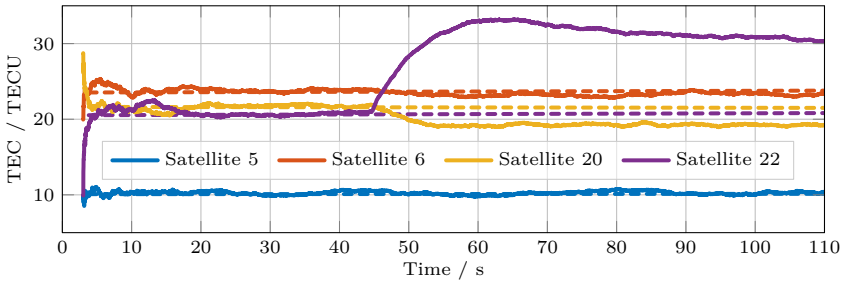
6.4.3 Actual Measurements

After the preliminary testing with the synthetic signals and the hardware emulation, actual measurement data is processed in the following to confirm the results. Therefore, the signal of a patch antenna placed on a rooftop has been recorded using the same equipment as for the measurement campaigns. The data was recorded in the late afternoon in order to observe maximum ionospheric TECs. For this reason, the data from the suburban measurement campaign from Section 6.2.2 were not used again, as these were recorded in the early morning. This measurement data has been evaluated before in [Sie+22b]. A ground truth has been determined using the open source tool RTKLIB [Tak+09] to determine a PPP estimate from the observables of a Trimble NetR9 receiver.

Figure 6.26 shows the constellation of the four used Galileo satellites with the resulting position RMSE in Figure 6.27. The conventional dual-frequency receiver using the ionosphere-free combination provides quite volatile position errors up to 15 m. The EML discriminator apparently suffers under the multipath propagation conditions on the rooftop. This effect is amplified by the ionosphere-free combination. The proposed IMMEKF on the other hand shows significantly lower position errors due to its multipath mitigating capability. With the proposed carrier range rate aiding the results are further smoothed and the RMSE is marginally reduces by 15 cm on



(a) With carrier range rate aiding.



(b) Without carrier range rate aiding.

Figure 6.25: Ionospheric TEC estimates of the proposed IMMEKF of hardware emulation. The dashed lines indicate the ground truth. After 45 s, the arising multipaths introduce errors.

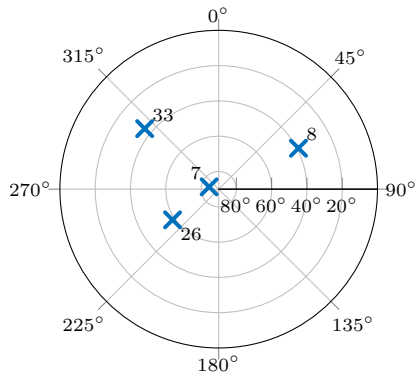


Figure 6.26: Satellite constellation of for processing selected Galileo satellites.

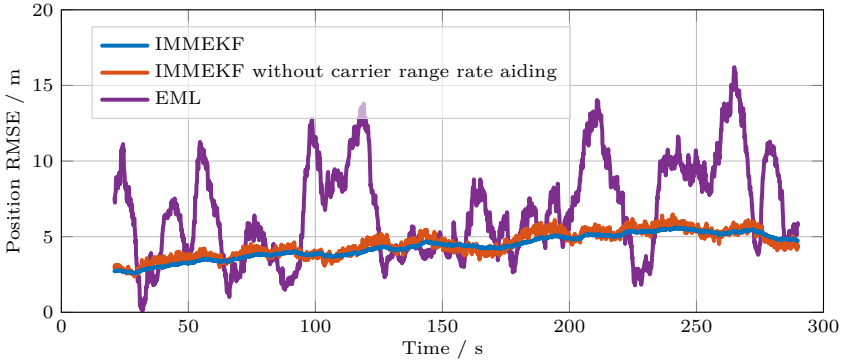


Figure 6.27: Position RMSE with proposed IMMEKF compared to the ionosphere-free combination.

average.

Figure 6.28 shows the estimated TEC estimates from the IMMEKF. The plotted values are already corrected by the differential hardware delays and broadcast group delays (BGDs), as explained in Subsection 5.1.4. Ionospheric maps from the International GNSS Service (IGS) were used to provide a ground truth. The estimated TECs match in the whole the ground truth values. Deviations may originate from residual multipath errors. The lower elevation satellites 8 and 33, that in general have stronger multipath propagation, seem to confirm that as they show larger deviations to the ground truth of up to 4 TECU. The proposed carrier range rate aiding helps to mitigate the effect of multipath to some extent resulting in smoother estimates.

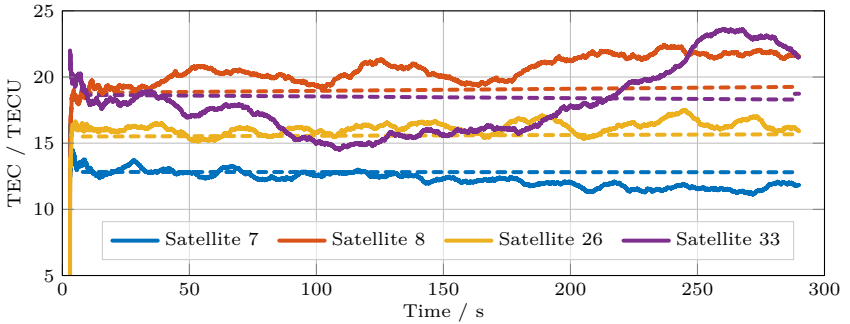
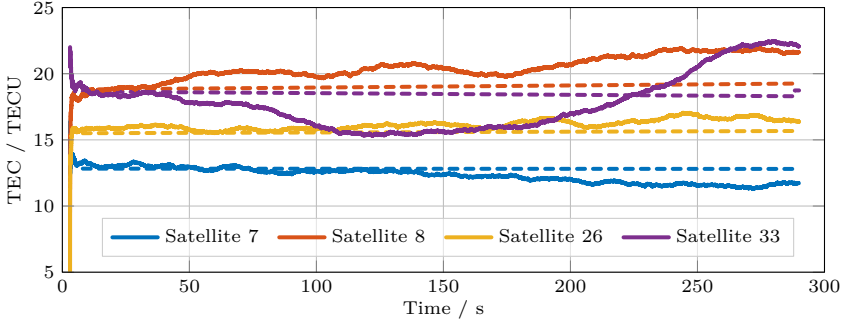


Figure 6.28: Ionospheric TEC estimates of the proposed IMMEKF. The dashed lines indicate the TEC values obtained from ionospheric maps from the IGS.

7 Extension of Multi-Correlator-Based Multipath Mitigation to Antenna Arrays

The preceding chapters have focused on global navigation satellite system (GNSS) receivers that rely on a single antenna only. As a result, the differentiation between line-of-sight (LOS) and multipath was limited to the time and frequency domain, which naturally limited its effectiveness. This limitation reflected in a residual multipath error, especially for short delay multipaths, see the multipath error envelopes in Chapter 3. As already mentioned in the introductory Chapter 1, the use of multiple antenna elements can overcome this limitation and facilitate the mitigation of multipath signals. With the additional spatial domain available, well-studied beamforming techniques can be applied, a review can be found in [Vag+16]. As a sufficient spatial separation is required between LOS and multipath, relying exclusively on the spatial domain for the multipath mitigation suffers likewise from limitations. For an efficient multipath mitigation, a combination of the space and time/frequency domain is needed. In the literature, proposals have been made that have pursued this approach before, see e.g., [Ant+05]; [Sah+07]; [Zor+20]. However, their increased complexity presents a challenge for practical application.

We propose therefore in the following the extension of the multipath mitigating EKF (MMEKF) from Chapter 2 to antenna arrays. The simultaneous exploitation of both, the space and time domain, is achieved by estimating one channel impulse response (CIR) for each antenna element and linking the central channel taps, which represent the LOS components, through the steering vector corresponding to the LOS direction of arrival (DOA) for the tracking criteria. All remaining channel taps can be set freely to consider for multipath propagation. The required signal model is given in Section 7.1 followed by the algorithm description in Section 7.2. The proposed solution is then evaluated in Section 7.3. This array extension addresses the fifth research question, that specifically points towards the potential of increased multipath robustness when using antenna arrays.

7.1 Signal Model

The signal model derived in Section 2.1 described the signal for a single antenna element. It can be simply generalized to the N_{ant} -element array case, see Figure 7.1, by introducing the element index $r = 1, \dots, N_{\text{ant}}$ to the pre-correlation signal model

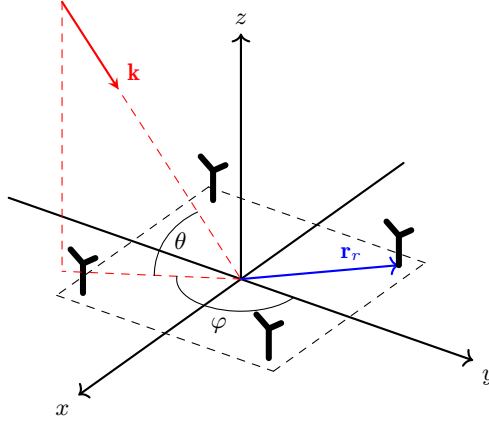


Figure 7.1: Schematic illustration of an antenna array with N_{ant} -elements. The element positions are given by the position vectors \mathbf{r}_r , $r = 1, \dots, N_{\text{ant}}$. The wave vector \mathbf{k} indicates an impinging signal with the azimuth and elevation angle φ and θ , respectively.

from Equation (2.10). This leads to

$$\begin{aligned} \mathbf{y}_{r,k} &= [y_{r,k}[0], \dots, y_{r,k}[N-1]]^T \in \mathbb{C}^{N \times 1} \\ &= \sum_{l_h=-L_h}^{L_h} h_{r,k}^{(l_h)} \mathbf{s}(\tau_k^{(0)} + T_h^{(l_h)}) + \boldsymbol{\eta}_{r,k}, \end{aligned} \quad (7.1)$$

where

$$\boldsymbol{\eta}_{r,k} = [\eta_{r,k}(kT_{\text{int}}), \eta_{r,k}(T_s + kT_{\text{int}}), \dots, \eta_{r,k}((N-1)T_s + kT_{\text{int}})]^T \quad (7.2)$$

$$\mathbf{s}(\tau_k^{(0)}) = [s(-\tau_k^{(0)}), s(T_s - \tau_k^{(0)}), \dots, s((N-1)T_s - \tau_k^{(0)})]^T. \quad (7.3)$$

The noise is modeled as an additive zero mean complex Gaussian noise $\boldsymbol{\eta}_{r,k} \sim \mathcal{N}(0, \sigma_{\eta_r}^2)$. For a better readability, the single-signal and single-frequency case has been considered only, omitting correspondingly the signal and band indices i and j , respectively. Moreover, it has been assumed that the LOS code delay $\tau_k^{(0)}$ is identical for each antenna element. This is a valid approximation when the maximal inter element spacing is sufficiently small with $\max_{r_1, r_2} |\mathbf{r}_{r_1} - \mathbf{r}_{r_2}| \ll c_0 T_c$, $r_1, r_2 = 1, \dots, N_{\text{ant}}$, $r_1 \neq r_2$, where \mathbf{r}_r is the antenna element position vector. Since arrays have typically a minimal inter element spacing of $\leq \lambda/2$ and consist of a limited number of elements, the approximation is valid for most GNSS applications. So far, the individual antenna signals are entirely independent. However, according to the DOAs of the impinging signals and the antenna element positions, dependencies exist. Consider the antenna array configuration as illustrated in Figure 7.1. The wave

vector of an impinging signal is given by [Tre04, Chapter 2]

$$\mathbf{k}(\varphi, \theta) = -\frac{2\pi}{\lambda} \begin{pmatrix} \cos(\theta) \sin(\varphi) \\ \cos(\theta) \cos(\varphi) \\ \sin(\theta) \end{pmatrix} \in \mathbb{R}^3. \quad (7.4)$$

The DOA of the impinging signal is specified by the azimuth and elevation angle φ and θ , respectively. Its corresponding steering vector can be computed as follows [Tre04, Chapter 2]

$$\mathbf{a}(\varphi, \theta) = \begin{bmatrix} e^{-j\mathbf{k}(\varphi, \theta)^T \mathbf{r}_1} \\ \vdots \\ e^{-j\mathbf{k}(\varphi, \theta)^T \mathbf{r}_{N_{\text{ant}}}} \end{bmatrix} \in \mathbb{C}^{N_{\text{ant}}}. \quad (7.5)$$

Since the angles φ and θ are defined in the local coordinate system of the array, its attitude is required to compute the steering vector. In the past, various approaches have been proposed to determine the attitude, see e.g. [Dan+14]; [Zor+20]. Without loss of generality, it is assumed to be known in the following. The steering vector definition in Equation (7.5) considers only the geometrical aspects. In reality, antenna element radiation characteristics introduce additional DOA dependent gain and phase mismatches. Since these effects are known to be constant over time [Sch+05], they can be measured once during the manufacturing process in an anechoic chamber and stored in a look-up table. At the radio frequency (RF) front end level, additional gain and phase mismatches are introduced by the active components, such as down-converters, amplifiers, or filters, as well as unequal cable lengths. Closely spaced signal guiding cables in the front end can additionally lead to crosstalk effects [Zor+16]. A calibration matrix can be used to model these effects. Without loss of generality however, we assumed in the signal model that the antenna array is calibrated and consists of ideal isotropic antenna elements without mutual coupling effects. Therewith, these additional uncertainties do not need to be considered. Having the pre-correlation signal model for antenna arrays defined, the subsequent section will cover the post-correlation signal model as well as the algorithm description.

7.2 Array Multipath Mitigating EKF

The extension of the MMEKF to antenna arrays has been initially proposed in [Sie+24] and will be referred to here as the array MMEKF (AMMEKF). Before the actual algorithm description, the post-correlation signal model is first defined in Subsection 7.2.1. Then, the actual AMMEKF is given in Subsection 7.2.2, followed by the required receiver architecture in Subsection 7.2.3. As the AMMEKF depicts an extension of the MMEKF, only differences are pointed out. Everything stated in Chapter 2 regarding the MMEKF also applies to the AMMEKF, if not otherwise specified below.

7.2.1 Correlator Bank

As for the base MMEKF, the received baseband signals $\tilde{\mathbf{z}}_{r,k}$ need to be first of all correlated by the receiver with a local replica of the pseudorandom noise (PRN) signal $s(t)$, see Section 2.3.1. The correlator bank required for this is given by

$$\mathbf{C}(\hat{\tau}_k^{(0)}) = \begin{bmatrix} \mathbf{s}^\top(\hat{\tau}_k^{(0)} - T_c^{(L_c)}) \\ \vdots \\ \mathbf{s}^\top(\hat{\tau}_k^{(0)} - T_c^{(1)}) \\ \mathbf{s}^\top(\hat{\tau}_k^{(0)} - T_c^{(0)}) \\ \vdots \\ \mathbf{s}^\top(\hat{\tau}_k^{(0)} - T_c^{(-L_c)}) \end{bmatrix}^\top \in \mathbb{C}^{N \times N_{\text{corr}}}. \quad (7.6)$$

Multiplying the correlator bank with the received baseband signals leads to the N_{corr} correlator outputs for the r -th antenna element

$$\begin{aligned} \tilde{\mathbf{z}}_{r,k} &= \mathbf{C}^H(\hat{\tau}_k^{(0)}) \mathbf{y}_{r,k} \in \mathbb{C}^{N_{\text{corr}} \times 1} \\ &= \sum_{l_h=-L_h}^{L_h} h_{r,k}^{(l_h)} \mathbf{C}^H(\hat{\tau}_k^{(0)}) \mathbf{s}(\tau_k^{(0)} + T_h^{(l_h)}) + \tilde{\boldsymbol{\eta}}_{r,\text{C},k}. \end{aligned} \quad (7.7)$$

The colored post-correlation noise $\tilde{\boldsymbol{\eta}}_{r,\text{C},k} \sim \mathcal{N}(\mathbf{0}_N, \mathbf{R}_{\tilde{\boldsymbol{\eta}}_{r,\text{C}}})$ has the noise covariance matrix [Mis+06, Chapter 10]

$$\mathbf{R}_{\tilde{\boldsymbol{\eta}}_{r,\text{C}}} = \sigma_{\eta_r}^2 \begin{bmatrix} \Phi_{ss}(0) & \cdots & \Phi_{ss}(2T_c^{(L_c)}) \\ \vdots & \ddots & \vdots \\ \Phi_{ss}(2T_c^{(L_c)}) & \cdots & \Phi_{ss}(0) \end{bmatrix} \in \mathbb{R}^{N_{\text{corr}} \times N_{\text{corr}}}. \quad (7.8)$$

The correlator outputs $\tilde{\mathbf{z}}_{r,k}$ are processed by the AMMEKF as explained in the following.

7.2.2 Joint Estimator

As for the base MMEKF from Chapter 2, a joint estimator will be used to process the correlator outputs and provide a LOS code delay estimate. Since the underlying signal model from Section 7.1 relies on one CIR per antenna signal, the state vector from Equation (2.29) for the AMMEKF must be extended accordingly to

$$\mathbf{x}_k = \left[\tau_k^{(0)}, \dot{\tau}_k^{(0)}, \text{Re}(\tilde{\mathbf{h}}_{1,k}^\top), \text{Im}(\tilde{\mathbf{h}}_{1,k}^\top), \dots, \text{Re}(\tilde{\mathbf{h}}_{N_{\text{ant}},k}^\top), \text{Im}(\tilde{\mathbf{h}}_{N_{\text{ant}},k}^\top) \right]^\top \in \mathbb{R}^{N_{\text{st}} \times 1} \quad (7.9)$$

with

$$\tilde{\mathbf{h}}_{r,k} = \left[h_{r,k}^{(-L_h)}, \dots, h_{r,k}^{(L_h)} \right]^T \in \mathbb{C}^{N_{\text{tap}} \times 1}, \quad (7.10)$$

holding then in total $N_{\text{st}} = 2N_{\text{ant}}(L_c + 1) + 2$ state variables. The process model of the MMEKF can be carried over unchanged for the AMMEKF using the same process matrix from Equation (2.31) and noise process covariance matrix from Equation (2.32). The constraining measurement from Equation (2.33), on the other hand, has to be adapted. While its purpose remains to ensure a reliable tracking of the LOS signal, it should now also exploit the newly available spatial domain with the intent to further increase multipath resilience. This has been done by incorporating the LOS steering vector $\mathbf{a}(\varphi_{\text{LOS}}, \theta_{\text{LOS}}) = [a_{1,k}, \dots, a_{N_{\text{ant}},k}]^T$ as follows

$$z_{k,\text{constr}} = \frac{1}{N_{\text{tap}}N_{\text{ant}}} \frac{\sum_{m=1}^{N_{\text{ant}}} \sum_{l_h=-L_h}^{L_h} \left| h_{r,k}^{(l_h)} \right|^2}{\left| \frac{1}{N_{\text{ant}}} \sum_{r=1}^{N_{\text{ant}}} h_{r,k}^{(0)} a_{r,k}^* \right|^2}. \quad (7.11)$$

The constraint is also set to $z_{k,\text{constr}} = 0$, $\forall k$, which results in the signal power maximization in the central channel coefficients $h_{r,k}^{(0)}$ of the CIRs, as for the MMEKF. However, due to the multiplication with the LOS steering vector in the denominator, this maximization is conducted only in the direction of the LOS signal. Multipaths, impinging with a sufficient spatial separation, even if they are temporally very close to the LOS, will be disregarded in this process, resulting in an increased multipath resilience. The required spatial separation between LOS and multipaths for a complete elimination depends on the array geometry and the number of antenna elements. In general, larger arrays with more antenna elements result in a better spatial resolution so that multipaths closer to the LOS can still be suppressed [Tre04, Chapter 2]. Just like with the single antenna MMEKF from Chapter 3, a weak or an obstructed LOS path imposes the risk of locking in with another signal path of higher power. The array characteristic, however, reduces this risk as the LOS power is being amplified and short delay multipaths, represented with the central channel coefficient, are being mitigated. It should be noted in this context, that the above defined constraining measurement is also compatible for the single antenna case with $N_{\text{ant}} = 1$. In this case, the LOS steering vector is reduced down to a scalar. The resulting loss of spatial information limits the multipath mitigation again to the temporal domain. The measurement model with the above defined constraining measurement is given by

$$\mathbf{z}_k = [\mathbf{z}_{1,k}^T, \dots, \mathbf{z}_{N_{\text{ant}},k}^T, z_{k,\text{constr}}]^T = \mathbf{f}(\mathbf{x}_k) \in \mathbb{R}^{N_{\text{meas}} \times 1} \quad (7.12)$$

with

$$\mathbf{z}_{r,k} = [\text{Re}(\tilde{\mathbf{z}}_{r,k}^T), \text{Im}(\tilde{\mathbf{z}}_{r,k}^T)]^T \in \mathbb{R}^{2N_{\text{corr}} \times 1} \quad (7.13)$$

and $N_{\text{meas}} = 2N_{\text{corr}}N_{\text{ant}} + 1$. The measurement noise scaling introduced with Equation (2.36) is applied unmodified with

$$\mathbf{R}_{\mathbf{w}\tilde{\eta}_{r,C}} = \mathbf{w}\mathbf{w}^T \circ \mathbf{R}_{\tilde{\eta}_{r,C}}, \quad (7.14)$$

where \mathbf{w} is the weighting function from Equation (2.37). The resulting measurement noise covariance matrix is then given by

$$\mathbf{R} = \text{diag} \left(\mathbf{R}_{\mathbf{w}\tilde{\eta}_{1,C}}/2, \mathbf{R}_{\mathbf{w}\tilde{\eta}_{1,C}}/2, \dots, \mathbf{R}_{\mathbf{w}\tilde{\eta}_{N_{\text{ant}},C}}/2, \mathbf{R}_{\mathbf{w}\tilde{\eta}_{N_{\text{ant}},C}}/2, \sigma_{\text{constr}}^2 \right) \in \mathbb{R}^{N_{\text{meas}} \times N_{\text{meas}}}. \quad (7.15)$$

Therewith, the measurement model is fully defined and one can apply the extended Kalman filter (EKF) with its prediction and update step, as explained in Section 2.2. The Jacobian matrix required for this is defined as

$$\begin{aligned} \mathbf{J}_{f,k} &= \left. \frac{d\mathbf{f}(\mathbf{x}_k)}{d\mathbf{x}_k} \right|_{\mathbf{x}_k = \tilde{\mathbf{x}}_{k|k-1}} \in \mathbb{R}^{N_{\text{meas}} \times N_{\text{st}}} \\ &= \left[\begin{array}{ccccccc} \frac{\partial \mathbf{f}(\mathbf{x}_k)}{\partial \tau_k^{(0)}} & \frac{\partial \mathbf{f}(\mathbf{x}_k)}{\partial \tau_k^{(0)}} & \frac{\partial \mathbf{f}(\mathbf{x}_k)}{\partial \text{Re}(\tilde{\mathbf{h}}_{1,k})} & \frac{\partial \mathbf{f}(\mathbf{x}_k)}{\partial \text{Im}(\tilde{\mathbf{h}}_{1,k})} & \cdots & \frac{\partial \mathbf{f}(\mathbf{x}_k)}{\partial \text{Re}(\tilde{\mathbf{h}}_{1,k})} & \frac{\partial \mathbf{f}(\mathbf{x}_k)}{\partial \text{Im}(\tilde{\mathbf{h}}_{1,k})} \end{array} \right] \Big|_{\mathbf{x}_k = \tilde{\mathbf{x}}_{k|k-1}}. \end{aligned} \quad (7.16)$$

The individual partial derivatives can be found in Appendix C. The approximation made in Equation (2.43) has been applied to the AMMEKF as well.

7.2.3 Receiver Architecture

The block diagram in Figure 7.2 shows an exemplary receiver architecture for the proposed AMMEKF. All N_{ant} RF signals are fed into the structure from the left. The first processing step is the down-conversion, leading to the baseband signals $\mathbf{y}_{r,k}$, which are in the figure referred to as \mathbf{Y}_k . These signals undergo then the correlation process leading to the correlator outputs $\tilde{\mathbf{z}}_{r,k}$ which are referred to as $\tilde{\mathbf{Z}}_k$ with the condensed notation in the figure. For the carrier tracking, the central prompt correlator outputs of $\tilde{\mathbf{Z}}_k$ are first beamformed and then used to compute the carrier discriminator. The latter drives the carrier numerically-controlled oscillator (NCO) which provides a suitable carrier replica for the down-conversion. On the code tracking side, the proposed AMMEKF is integrated. It processes all correlator outputs $\tilde{\mathbf{Z}}_k$, estimates internally the CIRs and the code Doppler, and provides then, under consideration of the constraining measurement from Equation (7.11), the LOS code delay estimate $\hat{\tau}_k^{(0)}$. It is used to adjust the local replicas in the correlator bank \mathbf{C} which closes the code tracking loop. Moreover, $\hat{\tau}_k^{(0)}$ is also provided to the position, velocity, and time (PVT) block. Once an approximate position estimate has been found, in combination with the assumption of a known array attitude and a calibrated array, the LOS steering vector $\mathbf{a}(\varphi_{\text{LOS}}, \theta_{\text{LOS}})$ can be computed using Equation (7.5). The required LOS DOAs can be determined from the ephemeris data in the navigation signals. The LOS steering vector $\mathbf{a}(\varphi_{\text{LOS}}, \theta_{\text{LOS}})$ is used to beamform the central prompt

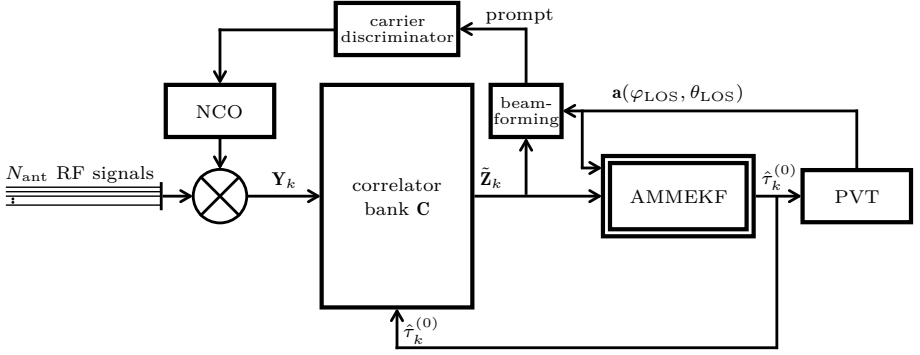


Figure 7.2: Proposed receiver architecture for the AMMEKF with $\mathbf{Y}_k = [\mathbf{y}_{1,k}, \dots, \mathbf{y}_{N_{\text{ant}},k}]$ and $\tilde{\mathbf{Z}}_k = [\tilde{\mathbf{z}}_{1,k}, \dots, \tilde{\mathbf{z}}_{N_{\text{ant}},k}]$.

correlators for the carrier tracking and is also provided to the AMMEKF so that it can exploit the spatial domain.

7.3 Performance Evaluation

The simulation parameters specified in Section 3.1 were adopted unchanged for the analyses in the following. Accordingly, synthetic signals are used again to ensure controlled conditions. Only the measurement noise variance for the constraining measurement has been adjusted to $\sigma_{\text{constr}} = 10^{-4}/N_{\text{ant}}$ in order to take the newly defined constraint from Equation (7.11) into account. The proposed AMMEKF is compared with solutions relying on a conventional deterministic beamformer (DET) [Tre04, Chapter 2]. Since the same information, i.e., the LOS steering vector, is provided to both, the proposed AMMEKF, as well as the DET, it depicts a valid competitor. The application of the DET results in a single beamformed signal which can be simply processed by the single-element code tracking algorithm. For the analyses in the following we use either a conventional early minus late (EML)-based delay locked loop (DLL) or the single-element variant of the AMMEKF in order to process the beamformed signal. The latter is simply the AMMEKF with $N_{\text{ant}} = 1$ so that the provided steering vector is reduced down to a scalar, i.e., in this case simply $\mathbf{a}(\varphi_{\text{LOS}}, \theta_{\text{LOS}}) = 1$. These two DET-based solutions will be referred to as DET + EML and DET + MMEKF, respectively. In all scenarios, Global Positioning System (GPS) coarse/acquisition (C/A) signals were considered. The number of correlators in the correlator banks were set to $N_{\text{corr}} = 11$ with a correlator spacing of $\Delta_c^{(l)} = 0.05T_c$, $l > 0$, resulting in a total bank width of $W_{\text{bank}} = 0.25T_c$. As discovered in Section 3.2.2, this bank configuration is a valid tradeoff between performance and complexity as adding more correlators results only in negligible performance improvements. The different considered antenna array configurations can be found in Figure 7.3. Each

array was simulated to be horizontally aligned. Moreover, the antenna element were simulated to be ideal isotropic, without mutual coupling between elements.

7.3.1 Multipath Mitigation

In the following, the multipath mitigation capability of the proposed AMMEKF is demonstrated. Therefore, the LOS is assumed to impinge from the zenith. The multipath hits the array with a 3 dB LOS to multipath power ratio, an additional access delay and phase of the multipath signal with respect to the LOS τ_{mul} and ϕ_{mul} , respectively. Its DOA is specified with the azimuth and elevation angles φ_{mul} and θ_{mul} , respectively. In all cases, no noise was added to the synthetic signals. The Figures 7.4 and 7.5 show the resulting tracking errors for different array configurations and multipath DOAs, delays, and phases using the proposed AMMEKF. The comparison with the corresponding single-element case, i.e., using the antenna from Figure 7.3a, clearly unveils how the proposed array extension improves the multipath mitigation. Obviously, when the multipath DOA approaches the LOS DOA, the performance of the array cases converge towards the single-antenna case with respect to the tracking error.

Figure 7.6 shows additionally the multipath errors for certain multipath elevation angles θ_{mul} . As only negligible variations have been observed over the multipath azimuth angle in the Figures 7.4 and 7.5, we set $\varphi_{\text{mul}} = 0^\circ$. Overall, the errors become smaller with increasing spatial separation between LOS and multipath. The largest errors have been obtained for the DET + EML case due to the limited multipath mitigation of the EML discriminator in the time domain. Replacing the EML with the multipath mitigating single-antenna variant of the AMMEKF, i.e., the DET + MMEKF case, considerably reduce the errors for the majority of multipath delays. The in this chapter proposed array extension for the MMEKF, namely the AMMEKF, turned out to not further improve the multipath resilience in the considered scenarios. Given that the proposed AMMEKF is of higher computational complexity as the code tracking filter has to process all N_{ant} satellite signals, one might prefer using

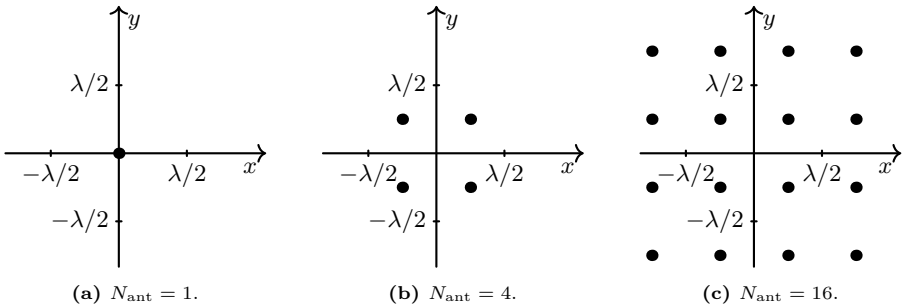


Figure 7.3: Considered array configurations for the performance evaluation. The minimal inter-element spacing is $\lambda/2$.

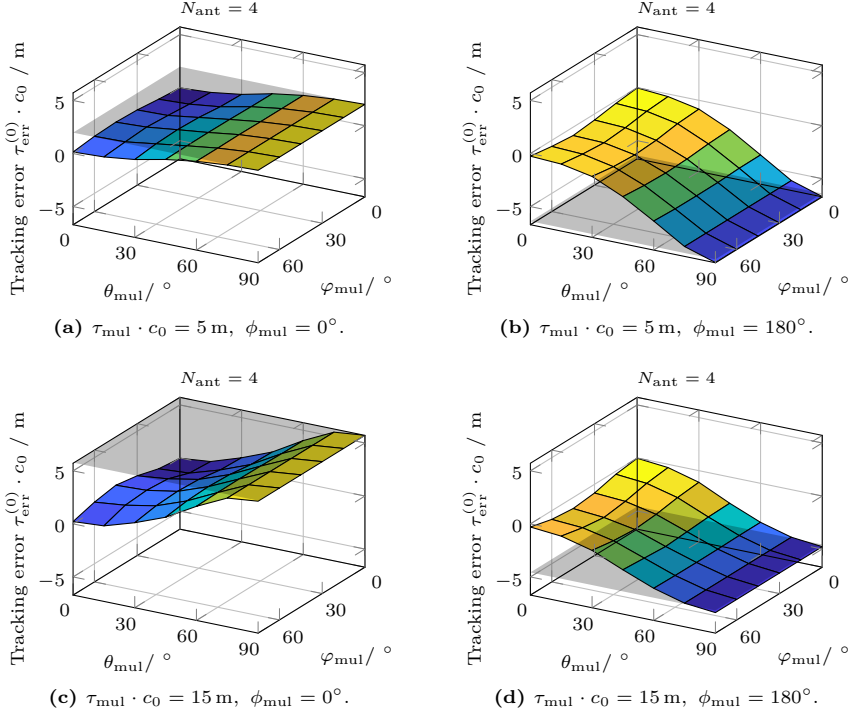


Figure 7.4: Illustration of the steady-state tracking error of the proposed AMMEKF for $N_{\text{ant}} = 4$. It was assumed that the LOS impinged from the zenith and a single static multipath existed with its azimuth and elevation angles φ_{mul} and θ_{mul} , respectively. The azimuth angles φ_{mul} were limited to the first 90° as the considered array configuration is rotationally symmetric. The performance of the single-element antenna from Figure 7.3a is indicated by the black translucent surface. As expected, the array solution performs identically to the single-element case when the DOA of the LOS coincides with the one from the multipath.

the DET + MMEKF case. It achieved the same steady-state tracking errors and the subsequent code tracking algorithm only has to process a single beamformed signal. When it comes to the noise performance, however, the proposed AMMEKF can be advantageous over the sequential application of a beamformer and a single-element code tracking algorithm. This is demonstrated in the following subsection.

7.3.2 Noise Performance

The noise performance of the proposed AMMEKF will be evaluated and compared with the DET + MMEKF case in the following. For the analyses conducted so far, the provided steering vector for the AMMEKF or the DET always coincided exactly with the actual LOS steering vector. In real-world scenarios, however, this is not always

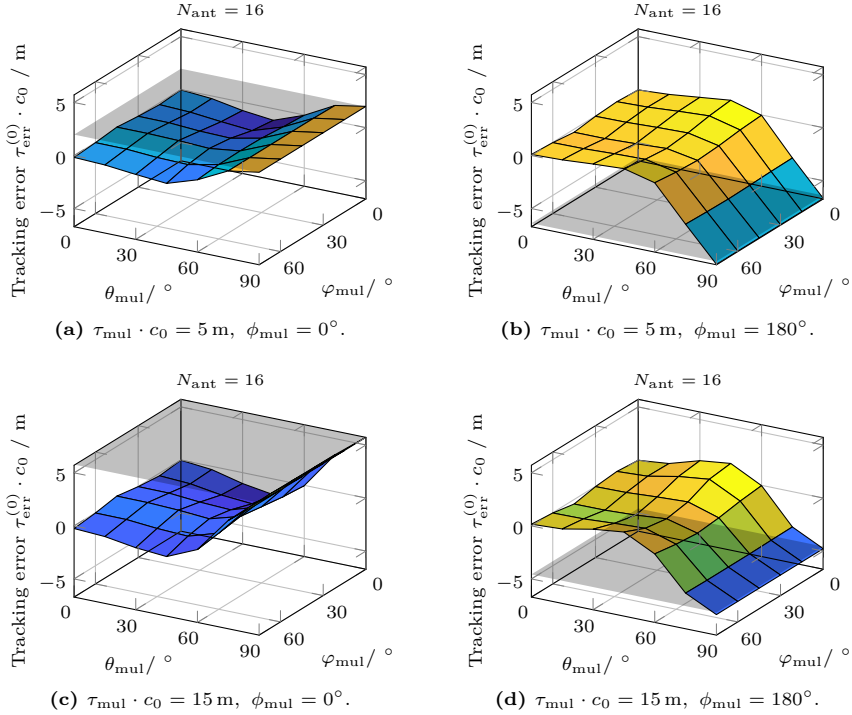


Figure 7.5: Illustration of the steady-state tracking error of the proposed AMMEKF for $N_{\text{ant}} = 16$. The considered setup is identical to the one from Figure 7.4. The larger antenna array enables the suppression of multipaths with a closer spatial proximity to the LOS.

possible. Due to for example an inaccurately estimated array attitude or an imperfect array calibration, the provided steering vector may be erroneous. For this reason, a steering vector is provided in the following, that coincides with a signal impinging with an azimuth angle $\varphi_a = 0^\circ$ and an elevation angle of θ_a . The latter is stepwise increased from 45° to 90° while the LOS stays throughout the entire simulation in the zenith. The noise performance is then determined as follow. The LOS signal with a constant carrier-to-noise density ratio (C/N_0) is tracked for 60s under consideration of the provided steering vector in the absence of multipath signals. The standard deviation (STD) of the obtained code delay estimates is averaged over in total 20 Monte Carlo runs.

Figure 7.7 illustrates the results. One can clearly see how for erroneous provided LOS steering vectors, i.e., for lower elevation angles θ_a , the STD of the code delay estimates increases. This effect, however, is in particular dominant for the DET-based approach. When providing erroneous steering vectors, the beamformer eliminates valuable LOS signal power. The subsequent code tracking algorithm suffers accord-

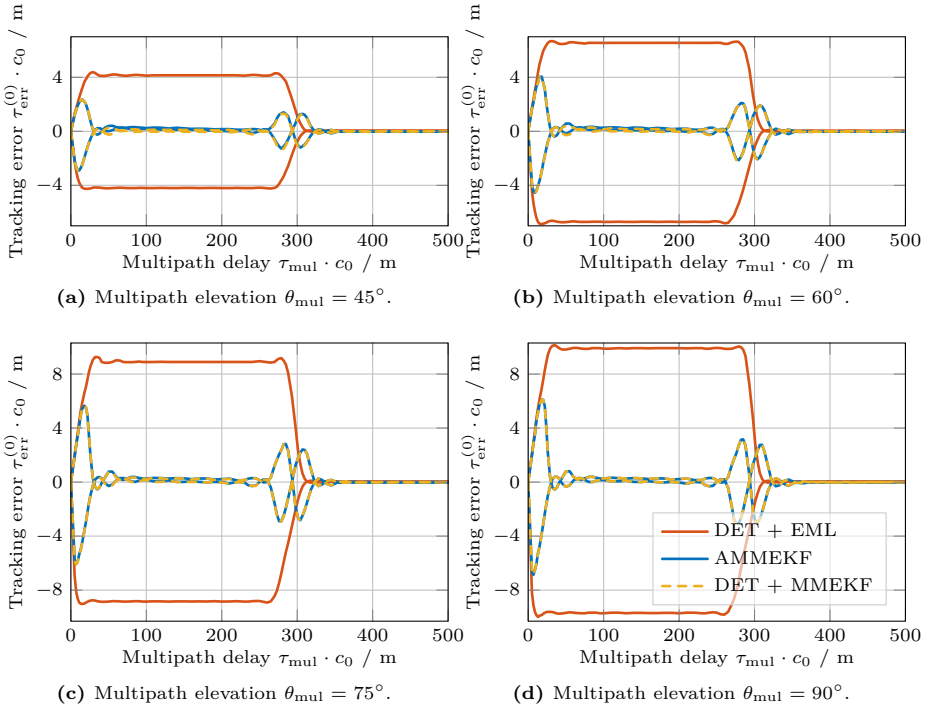


Figure 7.6: Multipath errors for different multipath elevation angles θ_{mul} using the 4-element array from Figure 7.3b. In all cases, the multipath azimuth angle was set to $\varphi_{\text{mul}} = 0^\circ$. As expected, with increased spatial separation between LOS and multipath, i.e., for decreasing θ_{mul} , the errors are reduced. The proposed AMMEKF performs basically identical to the combination of the DET and the corresponding single-element variant of the AMMEKF.

ingly under a higher observed noise level. For the proposed AMMEKF, on the other hand, the unfiltered antenna signals reach the code tracking stage. Therewith, the code delay estimate noise increases to a lesser extent for erroneous provided steering vectors.

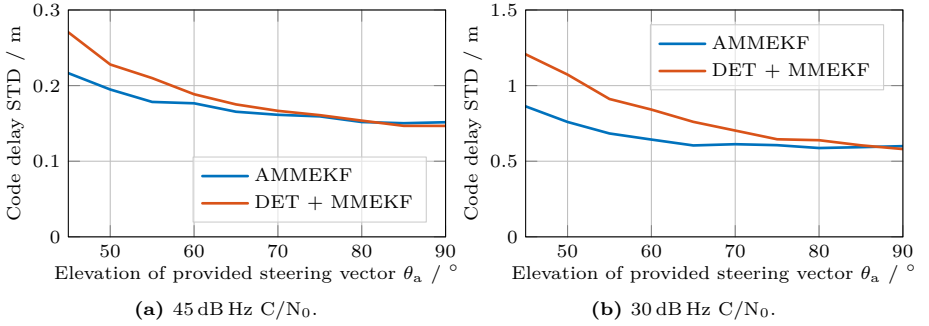


Figure 7.7: The noise performance of the proposed AMMEKF compared with the DET-based solution. For the shown results, the LOS impinged from the zenith. On the x-axis, the elevation of the signal corresponding to the provided steering vector is drawn. Lower elevation angles mean larger deviations between the provided steering vector and the actual LOS steering vector. The proposed AMMEKF outperforms the DET-based solution with respect to its noise performance for erroneous provided LOS steering vectors.

8 Conclusion

8.1 Summary and Contributions

The aim of this thesis was to develop a robust code tracking algorithm for global navigation satellite systems (GNSSs). An introduction to the main sources of error in this context and a broad overview of existing countermeasures was given in the first Chapter 1. This revealed certain gaps in the solutions available in the literature. In order to fill these gaps, five research questions were formulated in Section 1.3, which were addressed in the remainder of this thesis.

With multipath propagation being one of the major sources of error for GNSS receivers, a code tracking algorithm relying on a multi-correlator structure has been developed in Chapter 2, that was specifically designed to minimize such errors. Its multipath mitigation performance has been analyzed and demonstrated extensively with simulations in Chapter 3, including comparisons to state-of-the-art approaches. For an improved performance in environments with limited sky-view, the integration into an advanced vector tracking (VT) architecture has been proposed in Chapter 4.

The second major source of error in GNSSs originates from the ionosphere. State-of-the-art multi-frequency approaches are theoretically able to eliminate this effect to a large extent. However, residual multipath errors tend to be amplified in this process. For optimal results, both sources of error, multipath propagation and ionospheric delays, must be considered jointly. The proposed algorithm has therefore been extended to a multi-frequency processing in Chapter 5, combining its multipath mitigation capabilities with the estimation and elimination of the ionospheric delay.

The proposed solutions have finally been validated with actual measurement data in Chapter 6. Last but not least, an extension to antenna array systems has been proposed in Chapter 7 in order to additionally incorporate the spatial domain.

In this process, the following three *major* contributions were made.

- The development of a multipath mitigation algorithm for GNSS receivers that makes minimal assumptions about the radio propagation channel: Its multipath mitigation performance reached the current state-of-the-art. At the same time, an analysis of the algorithm's complexity revealed a lower computational complexity than the multipath estimating delay locked loop (MEDLL), i.e., a state-of-the-art multipath mitigation approach. Furthermore, its noise performance has been analyzed and found to be competitive to a conventional code tracking algorithm. Additionally, the integration of the developed algorithm

into advanced VT receiver architectures has been proposed. Therewith, the first three research questions have been fulfilled.

- The joint mitigation of multipath signals and estimation and elimination of ionospheric delays: Since residual multipath errors prevent an accurate elimination of ionospheric delays with state-of-the-art techniques, both effects must be treated jointly. This has been achieved by extending the proposed algorithm to a multi-frequency processing and taking into account the ionospheric effects. An additional carrier range rate aiding has been proposed to further increase robustness. This extension addresses the fourth research question.
- The extension of the proposed multipath mitigation algorithm to the spatial domain: Techniques relying solely in the time domain have a natural resolution limit, resulting in increasing residual multipath errors for short delay multipaths. In order to overcome this limitation, we have extended the proposed algorithm so that it also exploits the spatial domain using antenna array systems. Simulations have demonstrated the increased multipath resilience, in particular for short delay multipaths, answering the fifth research question.

In addition to that, several *minor* contributions were made, as listed in the following.

- The development of a reliable criterion for the tracking of the line-of-sight (LOS) signal in Chapter 2, which is largely unaffected by multipath signals: The signal model for the proposed multipath mitigation algorithm describes the radio propagation channel with a channel impulse response (CIR). In order to achieve a tracking of the LOS signal with this model, it was necessary to establish a relationship between the CIR and the LOS code delay. Therefore, an additional constraining measurement has been defined to link these two dimensions with minimal influence from multipath effects. The results in Chapter 3 and 6 have demonstrated successfully its effectiveness.
- Accounting for approximations made in the signal model by introducing a scaling of the measurement noise covariance matrix: With the assumption of finite CIRs in the signal model for the proposed multipath mitigation algorithm, signal contributions with delays larger than the maximal delay in the CIR cannot be accurately represented. In order to minimize errors that arise from this approximation, a scaling of the measurement noise covariances of the affected measurements has been proposed. Its effectiveness has been analyzed in Chapter 3.
- Determination of the multipath error envelopes of the proposed algorithm: The observed characteristics of the envelopes were discussed and explained. A comparison to other well-known multipath mitigation techniques, i.e., the high-resolution correlator (HRC) and the MEDLL, unveiled that the proposed solution reaches the current state-of-the-art performance, addressing the first research question.
- Derivation of the computational complexity of the proposed solution: Using the

required number of arithmetic operations as a metric allowed for a straight forward complexity comparison with other approaches. Comparisons were drawn to the well-known MEDLL in Chapter 3, where the proposed solution turned out to be of lower complexity.

- Investigation of low complexity variants of the proposed multipath mitigation algorithm: A reduction in the total number of correlators and alternative correlator placements were explored. Chapter 3 analyzed the tradeoffs made and showed a large potential for a complexity reduction until the multipath mitigation performance begins to degrade. This addresses the second research question.
- Comparison of the noise performance of the proposed multipath mitigation algorithm with state-of-the-art approaches: The results shown in Chapter 3 have shown the competitive noise performance of the proposed solution, addressing the first research question.
- Analysis of the dynamic response of the proposed algorithm and its dependency of different parameters: In order to allow for a fair comparison with other code tracking algorithms, their dynamic behaviors must be comparable. This has been shown in Chapter 3 in addition to an exhaustive analysis how different parameters of the proposed algorithm affect its dynamic behavior.
- Integration of the proposed multipath mitigation algorithm into an advanced VT receiver architecture in order to increase its robustness against LOS blockages: Since the proposed solution, just like conventional code tracking algorithms, assumes the availability of the LOS signal, the algorithm cannot handle blocked satellites. Integrated into an advanced VT receiver architecture, where all satellites are tracked jointly, overcomes this limitation. Chapter 6 demonstrated the effectiveness of this solution in challenging urban environments, fulfilling the third research question.

8.2 Recommendations

A multipath mitigation algorithm has been developed and evaluated in this thesis. Based on the findings of this work, the following recommendations can be made.

Since multipath propagation is an omnipresent environmental condition, as observed in the measurement campaigns in Chapter 6, it is generally recommended to rely on some form of multipath mitigation solution for a GNSS receiver. With the algorithm developed in this work, a well-working solution has been proposed. It is universally applicable, as in its design, minimal assumptions about the radio propagation channel were made. The proposed measurement noise scaling, which has been suggested to consider for approximations made in the signal model, is recommended to be used to improve the multipath mitigation performance. The low-complexity variants that have been proposed are in particular advisable for low power and small form factor applications, as they can reduce the computational complexity drastically

with minimal performance tradeoffs. When operating in environments with limited sky-view, such as urban environments, the proposed integration into advanced VT architectures is highly recommended. The joint processing of all satellites increases the ability to handle frequent LOS blockages which is a powerful combination with the multipath mitigation capability of the proposed algorithm.

In environments with high ionospheric activities, one may want to rely on multi-frequency receivers to actively eliminate ionospheric delays. Since state-of-the-art approaches tend to amplified multipath errors, limiting the ability to eliminate ionospheric delays, it is advisable to use the proposed joint multipath mitigation and ionospheric delay estimation and elimination algorithm in order to achieve improved results in such environments.

When the accuracy requirements are particularly high, antenna array systems can depict a powerful solution as they enable spatial signal processing techniques. The proposed multipath mitigation algorithm has been extended to exploit jointly the time and spatial domain. This approach is recommended when a high multipath mitigation, in particular against short delay multipaths, is desired.

A Jacobian Matrix for Multipath Mitigating EKF

The in Section 2.3 developed multipath mitigating EKF (MMEKF) relies on a nonlinear measurement model. Correspondingly, it is linearized at the current state estimate as part of the extended Kalman filter (EKF). This is done with the Jacobian matrix $\mathbf{J}_{f,k}$ introduced in Equation (2.42). In the following, the individual partial derivatives of the Jacobian are derived, under consideration of the approximation made in Equation (2.43). Beginning with the code delay, the derivative with respect to $\tau_k^{(0)}$ is given by [Ili+17]

$$\begin{aligned} \left. \frac{\partial \tilde{\mathbf{z}}_{i,k}}{\partial \tau_k^{(0)}} \right|_{\mathbf{x}_k = \hat{\mathbf{x}}_{k|k-1}} &= \sum_{l_h = -L_h}^{L_h} \hat{h}_{k|k-1}^{(l_h)} \mathbf{C}_i^H(\hat{\tau}_{k|k-1}^{(0)}) \left. \frac{\partial \mathbf{s}_i(\tau_k^{(0)} + T_h^{(l_h)})}{\partial \tau_k^{(0)}} \right|_{\mathbf{x}_k = \hat{\mathbf{x}}_{k|k-1}} \\ &= \sum_{l_h = -L_h}^{L_h} \hat{h}_{k|k-1}^{(l_h)} \begin{bmatrix} \Phi'_{s_i s_i}(T_h^{(l_h)} + T_c^{(L_c)}) \\ \vdots \\ \Phi'_{s_i s_i}(T_h^{(l_h)} + T_c^{(-L_c)}) \end{bmatrix}, \end{aligned} \quad (\text{A.1})$$

where $\Phi'_{s_i s_i}(\tau) = \int_{T_{\text{int}}} s_i^*(t) \dot{s}_i(t + \tau) dt$ with $\dot{s}_i(\tau) = \frac{ds_i(\tau)}{d\tau}$. The partial derivatives with respect to the real and imaginary part of the channel coefficients $h_k^{(l_h)}$ can be expressed as [Ili+17]; [Sie+21b]

$$\begin{aligned} \left. \frac{\partial \tilde{\mathbf{z}}_{i,k}}{\partial \text{Re}(h_k^{(l_h)})} \right|_{\mathbf{x}_k = \hat{\mathbf{x}}_{k|k-1}} &= -j \left. \frac{\partial \tilde{\mathbf{z}}_{i,k}}{\partial \text{Im}(h_k^{(l_h)})} \right|_{\mathbf{x}_k = \hat{\mathbf{x}}_{k|k-1}} \\ &= \mathbf{C}_i^H(\hat{\tau}_{k|k-1}^{(0)}) \mathbf{s}_i(\hat{\tau}_{k|k-1}^{(0)} + T_h^{(l_h)}) \\ &= \begin{bmatrix} \Phi_{s_i s_i}(T_h^{(l_h)} + T_c^{(L_c)}) \\ \vdots \\ \Phi_{s_i s_i}(T_h^{(l_h)} + T_c^{(-L_c)}) \end{bmatrix}. \end{aligned} \quad (\text{A.2})$$

For the constraining measurement from Equation (2.33), the following partial derivatives exist with [Sie+21b]

$$\frac{\partial z_{k,\text{constr}}}{\partial \text{Re}\left(h_k^{(l_h)}\right)\big|_{l_h \neq 0}} = \frac{2}{N_{\text{tap}} - 1} \frac{\text{Re}\left(h_k^{(l_h)}\right)\big|_{l_h \neq 0}}{\left|h_k^{(0)}\right|^2} \quad (\text{A.3})$$

$$\frac{\partial z_{k,\text{constr}}}{\partial \text{Im}\left(h_k^{(l_h)}\right)\big|_{l_h \neq 0}} = \frac{2}{N_{\text{tap}} - 1} \frac{\text{Im}\left(h_k^{(l_h)}\right)\big|_{l_h \neq 0}}{\left|h_k^{(0)}\right|^2} \quad (\text{A.4})$$

$$\frac{\partial z_{k,\text{constr}}}{\partial \text{Re}\left(h_k^{(0)}\right)} = -\frac{2}{N_{\text{tap}} - 1} \frac{\text{Re}\left(h_k^{(0)}\right)}{\left|h_k^{(0)}\right|^4} \sum_{l_h=-L_h, l_h \neq 0}^{L_h} \left|h_k^{(l_h)}\right|^2 \quad (\text{A.5})$$

$$\frac{\partial z_{k,\text{constr}}}{\partial \text{Im}\left(h_k^{(0)}\right)} = -\frac{2}{N_{\text{tap}} - 1} \frac{\text{Im}\left(h_k^{(0)}\right)}{\left|h_k^{(0)}\right|^4} \sum_{l_h=-L_h, l_h \neq 0}^{L_h} \left|h_k^{(l_h)}\right|^2. \quad (\text{A.6})$$

The remaining partial derivatives of $\mathbf{J}_{f,k}$ that are not explicitly specified above are simply zero. In order to reduce computational load during runtime of the MMEKF, one can precompute the time-invariant parts of Equations (A.1) and (A.2).

B Jacobian Matrix for Ionospheric Multipath Mitigating EKF

In the following the individual partial derivatives for the Jacobian matrix from Equation (5.24) of the ionospheric MMEKF (IMMEKF) are listed. The approximation made in Equation (2.43) for the multipath mitigating EKF (MMEKF) has also been applied here. First of all, the partial derivative with respect to the geometric code delay is given by

$$\begin{aligned} \left. \frac{\partial \tilde{\mathbf{z}}_{j,i,k}}{\partial \tau_{g,k}} \right|_{\mathbf{x}_k = \hat{\mathbf{x}}_{k|k-1}} &= \sum_{l_h = -L_{h,j}}^{L_{h,j}} \hat{h}_{j,k|k-1}^{(l_h)} \mathbf{C}_{j,i}^H(\hat{\tau}_{g,k|k-1}) \frac{\partial s_{j,i}(\tau_{g,k} + T_{h,j}^{(l_h)})}{\partial \tau_{g,k}} \bigg|_{\mathbf{x}_k = \hat{\mathbf{x}}_{k|k-1}} \\ &= \sum_{l_h = -L_{h,j}}^{L_{h,j}} \hat{h}_{j,k|k-1}^{(l_h)} \begin{bmatrix} \Phi'_{s_{j,i} s_{j,i}}(T_{h,j}^{(l_h)} + T_{c,j}^{(L_{c,j})}) \\ \vdots \\ \Phi'_{s_{j,i} s_{j,i}}(T_{h,j}^{(l_h)} + T_{c,j}^{(-L_{c,j})}) \end{bmatrix} \end{aligned} \quad (\text{B.1})$$

where $\Phi'_{s_{j,i} s_{j,i}}(\tau) = \int_{T_{\text{int}}} s_{j,i}^*(t) \dot{s}_{j,i}(t + \tau) dt$ with $\dot{s}_{j,i}(\tau) = \frac{ds_{j,i}(\tau)}{d\tau}$. Therewith, the derivative for the ionospheric total electron content (TEC) estimate can be expressed as

$$\left. \frac{\partial \tilde{\mathbf{z}}_{j,i,k}}{\partial n_{e,k}} \right|_{\mathbf{x}_k = \hat{\mathbf{x}}_{k|k-1}} = \frac{\alpha_I}{c_0 f_{c,j}^2} \left. \frac{\partial \tilde{\mathbf{z}}_{j,i,k}}{\partial \tau_{g,k}} \right|_{\mathbf{x}_k = \hat{\mathbf{x}}_{k|k-1}}. \quad (\text{B.2})$$

For the carrier range rate aiding introduced with Equations (5.10) and (5.11) the following derivatives exist.

$$\left. \frac{\partial z_{j1,j2,k,i\text{-free}}}{\partial \dot{\tau}_{g,k}} \right|_{\mathbf{x}_k = \hat{\mathbf{x}}_{k|k-1}} = \left. \frac{\partial z_{j1,j2,k,g\text{-free}}}{\partial \dot{n}_{e,k}} \right|_{\mathbf{x}_k = \hat{\mathbf{x}}_{k|k-1}} = 1 \quad (\text{B.3})$$

The remaining derivatives with respect to the channel coefficients and for the constraining measurement are basically equivalent to the MMEKF. However, for completeness, they are also listed below. The notation includes the frequency band indices

j .

$$\begin{aligned}
 \left. \frac{\partial \tilde{\mathbf{z}}_{j,i,k}}{\partial \text{Re} \left(h_{j,k}^{(l_h)} \right)} \right|_{\mathbf{x}_k = \hat{\mathbf{x}}_{k|k-1}} &= -j \left. \frac{\partial \tilde{\mathbf{z}}_{j,i,k}}{\partial \text{Im} \left(h_{j,k}^{(l_h)} \right)} \right|_{\mathbf{x}_k = \hat{\mathbf{x}}_{k|k-1}} \\
 &= \mathbf{C}_{j,i}^H \left(\hat{\tau}_{k|k-1}^{(0)} \right) \mathbf{s}_{j,i} \left(\hat{\tau}_{k|k-1}^{(0)} + T_{h,j}^{(l_h)} \right) \\
 &= \begin{bmatrix} \Phi_{s_{j,i} s_{j,i}} \left(T_{h,j}^{(l_h)} + T_{c,j}^{(L_{c,j})} \right) \\ \vdots \\ \Phi_{s_{j,i} s_{j,i}} \left(T_{h,j}^{(l_h)} + T_{c,j}^{(-L_{c,j})} \right) \end{bmatrix}. \tag{B.4}
 \end{aligned}$$

$$\left. \frac{\partial z_{j,k,\text{constr}}}{\partial \text{Re} \left(h_{j,k}^{(l_h)} \right)} \right|_{l_h \neq 0} = \frac{2}{N_{\text{tap},j} - 1} \frac{\text{Re} \left(h_{j,k}^{(l_h)} \right) \Big|_{l_h \neq 0}}{\left| h_{j,k}^{(0)} \right|^2} \tag{B.5}$$

$$\left. \frac{\partial z_{j,k,\text{constr}}}{\partial \text{Im} \left(h_{j,k}^{(l_h)} \right)} \right|_{l_h \neq 0} = \frac{2}{N_{\text{tap},j} - 1} \frac{\text{Im} \left(h_{j,k}^{(l_h)} \right) \Big|_{l_h \neq 0}}{\left| h_{j,k}^{(0)} \right|^2} \tag{B.6}$$

$$\frac{\partial z_{j,k,\text{constr}}}{\partial \text{Re} \left(h_{j,k}^{(0)} \right)} = -\frac{2}{N_{\text{tap},j} - 1} \frac{\text{Re} \left(h_{j,k}^{(0)} \right)}{\left| h_{j,k}^{(0)} \right|^4} \sum_{l_h = -L_{h,j}, l_h \neq 0}^{L_{h,j}} \left| h_{j,k}^{(l_h)} \right|^2 \tag{B.7}$$

$$\frac{\partial z_{j,k,\text{constr}}}{\partial \text{Im} \left(h_{j,k}^{(0)} \right)} = -\frac{2}{N_{\text{tap},j} - 1} \frac{\text{Im} \left(h_{j,k}^{(0)} \right)}{\left| h_{j,k}^{(0)} \right|^4} \sum_{l_h = -L_{h,j}, l_h \neq 0}^{L_{h,j}} \left| h_{j,k}^{(l_h)} \right|^2. \tag{B.8}$$

All unmentioned remaining partial derivaties are simply zero. Similar to the MMEKF, the time-invariant parts of the partial derivatives in Equation (B.1) and (B.4) can be computed in an initialization phase to reduce computational load.

C Jacobian Matrix for Array Multipath Mitigating EKF

This appendix lists the individual partial derivatives for the Jacobian matrix from Equation (7.16) under consideration of the approximation shown in Equation (2.43). Beginning with the line-of-sight (LOS) code delay estimate, the partial derivative is given by

$$\begin{aligned} \left. \frac{\partial \tilde{\mathbf{z}}_{r,k}}{\partial \tau_k^{(0)}} \right|_{\mathbf{x}_k = \hat{\mathbf{x}}_{k|k-1}} &= \sum_{l_h = -L_h}^{L_h} \hat{h}_{r,k|k-1}^{(l_h)} \mathbf{C}^H(\hat{\tau}_{k|k-1}^{(0)}) \left. \frac{\partial \mathbf{s}(\tau_k^{(0)} + T_h^{(l_h)})}{\partial \tau_k^{(0)}} \right|_{\mathbf{x}_k = \hat{\mathbf{x}}_{k|k-1}} \\ &= \sum_{l_h = -L_h}^{L_h} \hat{h}_{r,k|k-1}^{(l_h)} \begin{bmatrix} \Phi'_{ss}(T_h^{(l_h)} + T_c^{(L_c)}) \\ \vdots \\ \Phi'_{ss}(T_h^{(l_h)} + T_c^{(-L_c)}) \end{bmatrix} \end{aligned} \quad (\text{C.1})$$

with $\Phi'_{ss}(\tau) = \int_{T_{\text{int}}} s^*(t) \dot{s}(t + \tau) dt$ and $\dot{s}(\tau) = \frac{ds(\tau)}{d\tau}$. The partial derivatives with respect to the channel coefficients can be expressed as

$$\begin{aligned} \left. \frac{\partial \tilde{\mathbf{z}}_{r,k}}{\partial \text{Re}(h_{r,k}^{(l_h)})} \right|_{\mathbf{x}_k = \hat{\mathbf{x}}_{k|k-1}} &= -j \left. \frac{\partial \tilde{\mathbf{z}}_{r,k}}{\partial \text{Im}(h_{r,k}^{(l_h)})} \right|_{\mathbf{x}_k = \hat{\mathbf{x}}_{k|k-1}} \\ &= \mathbf{C}^H(\hat{\tau}_{k|k-1}^{(0)}) \mathbf{s}(\hat{\tau}_{k|k-1}^{(0)} + T_h^{(l_h)}) \\ &= \begin{bmatrix} \Phi_{ss}(T_h^{(l_h)} + T_c^{(L_c)}) \\ \vdots \\ \Phi_{ss}(T_h^{(l_h)} + T_c^{(-L_c)}) \end{bmatrix}. \end{aligned} \quad (\text{C.2})$$

The partial derivatives for the constraining measurement are as follows:

$$\frac{\partial z_{k,\text{constr}}}{\partial \text{Re}(h_{r,k}^{(l_h)})} \Big|_{l_h \neq 0} = \frac{2}{N_{\text{tap}} N_{\text{ant}}} \frac{\text{Re}(h_{r,k}^{(l_h)}) \Big|_{l_h \neq 0}}{\left| \frac{1}{N_{\text{ant}}} \sum_{r=1}^{N_{\text{ant}}} h_{r,k}^{(0)} a_{r,k}^* \right|^2} \quad (\text{C.3})$$

$$\frac{\partial z_{k,\text{constr}}}{\partial \text{Im}(h_{r,k}^{(l_h)})} \Big|_{l_h \neq 0} = \frac{2}{N_{\text{tap}} N_{\text{ant}}} \frac{\text{Im}(h_{r,k}^{(l_h)}) \Big|_{l_h \neq 0}}{\left| \frac{1}{N_{\text{ant}}} \sum_{r=1}^{N_{\text{ant}}} h_{r,k}^{(0)} a_{r,k}^* \right|^2} \quad (\text{C.4})$$

$$\begin{aligned}
\frac{\partial z_{k,\text{constr}}}{\partial \text{Re} \left(h_{r,k}^{(0)} \right)} &= \frac{2}{N_{\text{tap}} N_{\text{ant}}} \frac{1}{\left| \frac{1}{N_{\text{ant}}} \sum_{r=1}^{N_{\text{ant}}} h_{r,k}^{(0)} a_{r,k}^* \right|^4} \\
&\cdot \left\{ \text{Re} \left(h_{r,k}^{(0)} \right) \left| \frac{1}{N_{\text{ant}}} \sum_{r=1}^{N_{\text{ant}}} h_{r,k}^{(0)} a_{r,k}^* \right|^2 - \frac{2}{N_{\text{ant}}^2} \sum_{m=1}^{N_{\text{ant}}} \sum_{l_h=-L_h}^{L_h} \left| h_{r,k}^{(l_h)} \right|^2 \right. \\
&\cdot \left[\sum_{r=1}^{N_{\text{ant}}} \left(\text{Re} \left(h_{r,k}^{(0)} \right) \text{Re} (a_{r,k}) + \text{Im} \left(h_{r,k}^{(0)} \right) \text{Im} (a_{r,k}) \right) \text{Re} (a_{r,k}) \right. \\
&\left. \left. - \sum_{r=1}^{N_{\text{ant}}} \left(\text{Im} \left(h_{r,k}^{(0)} \right) \text{Re} (a_{r,k}) - \text{Re} \left(h_{r,k}^{(0)} \right) \text{Im} (a_{r,k}) \right) \text{Im} (a_{r,k}) \right] \right\}
\end{aligned} \tag{C.5}$$

$$\begin{aligned}
\frac{\partial z_{k,\text{constr}}}{\partial \text{Im} \left(h_{r,k}^{(0)} \right)} &= \frac{2}{N_{\text{tap}} N_{\text{ant}}} \frac{1}{\left| \frac{1}{N_{\text{ant}}} \sum_{r=1}^{N_{\text{ant}}} h_{r,k}^{(0)} a_{r,k}^* \right|^4} \\
&\cdot \left\{ \text{Im} \left(h_{r,k}^{(0)} \right) \left| \frac{1}{N_{\text{ant}}} \sum_{r=1}^{N_{\text{ant}}} h_{r,k}^{(0)} a_{r,k}^* \right|^2 - \frac{2}{N_{\text{ant}}^2} \sum_{m=1}^{N_{\text{ant}}} \sum_{l_h=-L_h}^{L_h} \left| h_{r,k}^{(l_h)} \right|^2 \right. \\
&\cdot \left[\sum_{r=1}^{N_{\text{ant}}} \left(\text{Re} \left(h_{r,k}^{(0)} \right) \text{Re} (a_{r,k}) + \text{Im} \left(h_{r,k}^{(0)} \right) \text{Im} (a_{r,k}) \right) \text{Im} (a_{r,k}) \right. \\
&\left. \left. + \sum_{r=1}^{N_{\text{ant}}} \left(\text{Im} \left(h_{r,k}^{(0)} \right) \text{Re} (a_{r,k}) - \text{Re} \left(h_{r,k}^{(0)} \right) \text{Im} (a_{r,k}) \right) \text{Re} (a_{r,k}) \right] \right\}
\end{aligned} \tag{C.6}$$

All unmentioned partial derivatives are simply zero. It is advisable to precompute the time-invariant terms in an initialization phase in order to reduce the computing load during runtime, as for the base multipath mitigating EKF (MMEKF).

D Gauss-Jordan Elimination Complexity

For the complexity considerations made in Section 2.3.3, the number of elementary arithmetic operations for a matrix inversion was required. For simplicity, the well-known Gauss-Jordan Elimination was exemplarily chosen. With this technique, the inverse of an invertible matrix $\mathbf{A} \in \mathbb{R}^{p \times p}$ with the entries $a_{jk}^{(0)}$, $j, k = 1, \dots, p$ is determined by applying row and columns operations until \mathbf{A} is an identity matrix. The inverse is then obtained by applying the same sequence of row and column operations onto an identity matrix \mathbf{I}_p of identical dimension. In [Far88, Chapter 1], the number of operations required for the Gaussian elimination to solve a system of linear equations has been derived. As this is a related problem, the derivation in the following is based on [Far88, Chapter 1]. The variable names chosen in this appendix are to be considered independently of the rest of this work, as the nomenclature conflicts in part with definitions made in other chapters. Table D.1 illustrates the first part of the Gauss-Jordan Elimination. The left most column indicates the current stage index i . In the initialization stage $i = 0$, the second column holds the coefficients $a_{jk}^{(0)}$ of the matrix \mathbf{A} that will be inverted. The right most column holds the identity matrix \mathbf{I}_p , which will be transformed to the inverse of \mathbf{A} in this process. The entries $a_{jk}^{(i)}$ and $b_{jk}^{(i)}$ are given by

$$a_{jk}^{(i)} = a_{jk}^{(i-1)} - \frac{a_{ji}^{(i-1)}}{a_{ii}^{(i-1)}} a_{ik}^{(i-1)} \quad \begin{cases} j = i+1, \dots, p \\ k = i+1, \dots, p \end{cases} \quad (\text{D.1})$$

$$b_{jk}^{(i)} = b_{jk}^{(i-1)} - \frac{a_{ji}^{(i-1)}}{a_{ii}^{(i-1)}} b_{ik}^{(i-1)} \quad \begin{cases} j = i+1, \dots, p \\ k = 1, \dots, i-1 \end{cases} \quad (\text{D.2})$$

$$b_{ji}^{(i)} = -\frac{a_{ji}^{(i-1)}}{a_{ii}^{(i-1)}} \quad \begin{cases} j = i+1, \dots, p \end{cases} \quad (\text{D.3})$$

Table D.1: First part of Gauss-Jordan Elimination.

$i = 0$	$a_{11}^{(0)}$	$a_{12}^{(0)}$	$a_{13}^{(0)}$	\cdots	$a_{1p}^{(0)}$	1	0	0	\cdots	0
	$a_{21}^{(0)}$	$a_{22}^{(0)}$	$a_{23}^{(0)}$	\cdots	$a_{2p}^{(0)}$	0	1	0	\cdots	0
	$a_{31}^{(0)}$	$a_{32}^{(0)}$	$a_{33}^{(0)}$	\cdots	$a_{3p}^{(0)}$	0	0	1	\cdots	0
	\vdots	\vdots	\vdots	\ddots	\vdots	\vdots	\vdots	\vdots	\ddots	\vdots
	$a_{p1}^{(0)}$	$a_{p2}^{(0)}$	$a_{p3}^{(0)}$	\cdots	$a_{pp}^{(0)}$	0	0	0	\cdots	1
$i = 1$	$a_{11}^{(0)}$	$a_{12}^{(0)}$	$a_{13}^{(0)}$	\cdots	$a_{1p}^{(0)}$	1	0	0	\cdots	0
	0	$a_{22}^{(1)}$	$a_{23}^{(1)}$	\cdots	$a_{2p}^{(1)}$	$b_{21}^{(1)}$	1	0	\cdots	0
	0	$a_{32}^{(1)}$	$a_{33}^{(1)}$	\cdots	$a_{3p}^{(1)}$	$b_{31}^{(1)}$	0	1	\cdots	0
	\vdots	\vdots	\vdots	\ddots	\vdots	\vdots	\vdots	\vdots	\ddots	\vdots
	0	$a_{p2}^{(1)}$	$a_{p3}^{(1)}$	\cdots	$a_{pp}^{(1)}$	$b_{p1}^{(1)}$	0	0	\cdots	1
$i = 2$	$a_{11}^{(0)}$	$a_{12}^{(0)}$	$a_{13}^{(0)}$	\cdots	$a_{1p}^{(0)}$	1	0	0	\cdots	0
	0	$a_{22}^{(1)}$	$a_{23}^{(1)}$	\cdots	$a_{2p}^{(1)}$	$b_{21}^{(1)}$	1	0	\cdots	0
	0	0	$a_{33}^{(2)}$	\cdots	$a_{3p}^{(2)}$	$b_{31}^{(2)}$	$b_{32}^{(2)}$	1	\cdots	0
	\vdots	\vdots	\vdots	\ddots	\vdots	\vdots	\vdots	\vdots	\ddots	\vdots
	0	0	$a_{p3}^{(2)}$	\cdots	$a_{pp}^{(2)}$	$b_{p1}^{(2)}$	$b_{p2}^{(2)}$	0	\cdots	1
$i = p - 1$	$a_{11}^{(0)}$	$a_{21}^{(0)}$	$a_{13}^{(0)}$	\cdots	$a_{1p}^{(0)}$	1	0	0	\cdots	0
	0	$a_{22}^{(1)}$	$a_{23}^{(1)}$	\cdots	$a_{2p}^{(1)}$	$b_{21}^{(1)}$	1	0	\cdots	0
	0	0	$a_{33}^{(2)}$	\cdots	$a_{3p}^{(2)}$	$b_{31}^{(2)}$	$b_{32}^{(2)}$	1	\cdots	0
	\vdots	\vdots	\vdots	\ddots	\vdots	\vdots	\vdots	\vdots	\ddots	\vdots
	0	0	0	\cdots	$a_{pp}^{(p-1)}$	$b_{p1}^{(p-1)}$	$b_{p2}^{(p-1)}$	$b_{p3}^{(p-1)}$	\cdots	1

with the stage index $i = 1, \dots, p - 1$. Correspondingly, the following number of operations for the first part of the algorithm are needed

$$\text{Multiplications} \quad \sum_{i=1}^{p-1} (p-i)^2 + \sum_{i=1}^{p-1} (i-1)(p-i) = \frac{p(p-1)^2}{2} \quad (\text{D.4})$$

$$\text{Division} \quad \sum_{i=1}^{p-1} (p-i) = \frac{p(p-1)}{2} \quad (\text{D.5})$$

$$\text{Subtractions} \quad \sum_{i=1}^{p-1} (p-i)^2 + \sum_{i=1}^{p-1} (i-1)(p-i) + \sum_{i=1}^{p-1} (p-i) = \frac{p(p-1)^2}{2} + \frac{p(p-1)}{2}. \quad (\text{D.6})$$

Equally, the second part of the algorithm is illustrated in Table D.2. In the last row, i.e., for stage $i = p$, the left matrix turns into a diagonal matrix and the right one

holds the inverse of \mathbf{A} with the coefficients

$$b_{jk}^{(i)} = b_{jk}^{(i-1)} - \frac{a_{j,p-i+1}}{a_{p-i+1,p-i+1}} b_{p-i+1,k}^{(i-1)} \quad \begin{cases} j = 1, \dots, p-i \\ k = 1, \dots, p \\ i = 2, \dots, p-1 \end{cases} \quad (\text{D.7})$$

Due to the lower triangular matrix shape of the coefficients in the right most column in Table D.2, the coefficient calculation for the first stage $i = 1$ is simplified with

$$b_{jk}^{(i)} = b_{jk}^{(i-1)} - \frac{a_{j,p-i+1}}{a_{p-i+1,p-i+1}} b_{p-i+1,k}^{(i-1)} \quad \begin{cases} j = 2, \dots, p-i \\ k = 1, \dots, j-1 \\ i = 1 \end{cases} \quad (\text{D.8})$$

$$b_{jk}^{(i)} = 1 - \frac{a_{j,p-i+1}}{a_{p-i+1,p-i+1}} b_{p-i+1,k}^{(i-1)} \quad \begin{cases} j = 1, \dots, p-i \\ k = j \\ i = 1 \end{cases} \quad (\text{D.9})$$

$$b_{jk}^{(i)} = -\frac{a_{j,p-i+1}}{a_{p-i+1,p-i+1}} b_{p-i+1,k}^{(i-1)} \quad \begin{cases} j = 1, \dots, p-i \\ k = j+1, \dots, p-1 \\ i = 1 \end{cases} \quad (\text{D.10})$$

$$b_{jk}^{(i)} = -\frac{a_{j,p-i+1}}{a_{p-i+1,p-i+1}} \quad \begin{cases} j = 1, \dots, p-i \\ k = p \\ i = 1 \end{cases} \quad (\text{D.11})$$

To reach the final stage, one only needs to divide by the remaining diagonal entries on the left hand side, thus

$$b_{jk}^{(i)} = b_{jk}^{(i-1)} / a_{jj}^{(i-1)} \quad \begin{cases} j = 1, \dots, p-i \\ k = 1, \dots, p \\ i = p \end{cases} \quad (\text{D.12})$$

This leads to the following number of operations for the second part of the algorithm

$$\text{Multiplications} \quad \sum_{i=1}^{p-1} p(p-i) - (p-1) = \frac{p^2(p-1)}{2} - (p-1) \quad (\text{D.13})$$

$$\text{Division} \quad \sum_{i=1}^{p-1} (p-i) = \frac{p(p-1)}{2} \quad (\text{D.14})$$

$$\text{Subtractions} \quad \sum_{i=1}^{p-1} p(p-i) + p^2 = \frac{p^2(p-1)}{2} + p^2 \quad (\text{D.15})$$

Both parts together result in the following numbers of operations for the full Gauss-Jordan Elimination algorithm.

$$\text{Multiplications} \quad p^2 + \frac{3}{2}p^2 - \frac{1}{2}p + 1 \quad (\text{D.16})$$

$$\text{Division} \quad 2p^2 - p \quad (\text{D.17})$$

$$\text{Subtractions} \quad p^3 - p^2 \quad (\text{D.18})$$

Bibliography

- [Aka74] H. Akaike. “A New Look at the Statistical Model Identification”. In: *IEEE Transactions on Automatic Control* 19.6 (Dec. 1974), pp. 716–723. DOI: 10.1109/TAC.1974.1100705.
- [Ant+05] F. Antreich et al. “Estimation of Synchronization Parameters Using SAGE in a GNSS-Receiver”. In: *Proceedings of the 18th International Technical Meeting of the Satellite Division of The Institute of Navigation (ION GNSS 2005)*. Sept. 2005, pp. 2124–2131.
- [Ant+22a] T. Anthony and M. Kerns. *Interface Control Documents IS-GPS-200 N*. Aug. 22, 2022.
- [Ant+22b] T. Anthony and V. Quan. *Interface Control Documents IS-GPS-705 J*. Aug. 1, 2022.
- [Bal+00] Í. Ballester-Gúrpide et al. “Future GNSS Constellation Performances inside Urban Environments”. In: *Proceedings of the 13th International Technical Meeting of the Satellite Division of The Institute of Navigation (ION GPS 2000)*. Sept. 2000, pp. 2436–2445.
- [Bar+01] Y. Bar-Shalom, X. R. Li, and T. Kirubarajan. *Estimation with Applications to Tracking and Navigation: Theory Algorithms and Software*. 1st ed. John Wiley & Sons, Ltd, 2001. 584 pp. DOI: 10.1002/0471221279.
- [Bar+12] M. Barczyk and A. F. Lynch. “Integration of a Triaxial Magnetometer into a Helicopter UAV GPS-Aided INS”. In: *IEEE Transactions on Aerospace and Electronic Systems* 48.4 (Oct. 2012), pp. 2947–2960. DOI: 10.1109/TAES.2012.6324671.
- [Ben24] C. Benoît. “Note Sur Une Méthode de Résolution des équations Normales Provenant de L’Application de la MéThode des Moindres Carrés a un Système D’équations Linéaires en Nombre Inférieur a Celui des Inconnues. — Application de la Méthode a la Résolution D’un Système Défini D’éQuations LinéAires”. In: *Bulletin géodésique* 2.1 (Apr. 1, 1924), pp. 67–77. DOI: 10.1007/BF03031308.
- [Bia+12] O. Bialer, D. Raphaeli, and A. J. Weiss. “Efficient Time of Arrival Estimation Algorithm Achieving Maximum Likelihood Performance in Dense Multipath”. In: *IEEE Transactions on Signal Processing* 60.3 (Mar. 2012), pp. 1241–1252. DOI: 10.1109/TSP.2011.2174055.
- [Bis+14] I. Bisio et al. “A Trainingless WiFi Fingerprint Positioning Approach Over Mobile Devices”. In: *IEEE Antennas and Wireless Propagation Letters* 13 (2014), pp. 832–835. DOI: 10.1109/LAWP.2014.2316973.

- [Bla+12] N. Blanco-Delgado and F. D. Nunes. "Multipath Estimation in Multi-correlator GNSS Receivers Using the Maximum Likelihood Principle". In: *IEEE Transactions on Aerospace and Electronic Systems* 48.4 (Oct. 2012), pp. 3222–3233. DOI: 10.1109/TAES.2012.6324696.
- [Boc+22] M. Bochkati, J. Dampf, and T. Pany. "On the Use of Multi-correlator Values as Sufficient Statistics as Basis for Flexible Ultra-tight GNSS/INS Integration Developments". In: *2022 25th International Conference on Information Fusion (FUSION)*. July 2022, pp. 1–8. DOI: 10.23919/FUSION49751.2022.9841253.
- [Bra01] M. Braasch. "Performance Comparison of Multipath Mitigating Receiver Architectures". In: *2001 IEEE Aerospace Conference Proceedings (Cat. No.01TH8542)*. Vol. 3. Mar. 2001, pp. 1309–1315. DOI: 10.1109/AERO.2001.931361.
- [Bre+07] M. Brenneman et al. "Mitigation of GPS Multipath Using Polarization and Spatial Diversities". In: *Proceedings of the 20th International Technical Meeting of the Satellite Division of The Institute of Navigation (ION GNSS 2007)*. Sept. 2007, pp. 1221–1229.
- [Bre+92] B. J. H. van den Brekel and D. J. R. van Nee. "GPS Multipath Mitigation by Antenna Movements". In: *Electronics Letters* 28.25 (Dec. 3, 1992), pp. 2286–2288. DOI: 10.1049/e1:19921471.
- [Bre+97] K. Breivik et al. "Estimation of Multipath Error in GPS Pseudorange Measurements". In: *NAVIGATION* 44.1 (Mar. 1, 1997), pp. 43–52. DOI: 10.1002/j.2161-4296.1997.tb01938.x.
- [Bro+12] R. G. Brown and P. Y. C. Hwang. *Introduction to Random Signals and Applied Kalman Filtering with Matlab Exercises*. 4th ed. John Wiley & Sons, Feb. 2012. 400 pp. ISBN: 978-0-470-60969-9.
- [Che+11] X. Chen et al. "Turbo Architecture for Multipath Mitigation in Global Navigation Satellite System Receivers". In: *IET Radar, Sonar & Navigation* 5.5 (June 2, 2011), pp. 517–527. DOI: 10.1049/iet-rsn.2010.0356.
- [Che+13] X. Chen et al. "Comparative Studies of GPS Multipath Mitigation Methods Performance". In: *IEEE Transactions on Aerospace and Electronic Systems* 49.3 (July 2013), pp. 1555–1568. DOI: 10.1109/TAES.2013.6558004.
- [Chi+20] K.-W. Chiang et al. "Assessment for INS/GNSS/Odometer/Barometer Integration in Loosely-Coupled and Tightly-Coupled Scheme in a GNSS-Degraded Environment". In: *IEEE Sensors Journal* 20.6 (Mar. 2020), pp. 3057–3069. DOI: 10.1109/JSEN.2019.2954532.
- [Cio+20] G. Cioffi and D. Scaramuzza. "Tightly-Coupled Fusion of Global Positional Measurements in Optimization-based Visual-Inertial Odometry". In: *2020 IEEE/RSJ International Conference on Intelligent Robots and Systems (IROS)*. Oct. 2020, pp. 5089–5095. DOI: 10.1109/IROS45743.2020.9341697.

- [Clo+07a] P. Closas, C. Fernandez-Prades, and J. A. Fernandez-Rubio. "Maximum Likelihood Estimation of Position in GNSS". In: *IEEE Signal Processing Letters* 14.5 (May 2007), pp. 359–362. DOI: 10.1109/LSP.2006.888360.
- [Clo+07b] P. Closas, C. Fernandez-Prades, and J. A. Fernandez-Rubio. "ML Estimation of Position in a GNSS Receiver Using the SAGE Algorithm". In: *2007 IEEE International Conference on Acoustics, Speech and Signal Processing - ICASSP '07*. Vol. 3. Apr. 2007, pp. III-1045-III-1048. DOI: 10.1109/ICASSP.2007.366862.
- [Clo+09] P. Closas, C. Fernandez-Prades, and J. A. Fernandez-Rubio. "A Bayesian Approach to Multipath Mitigation in GNSS Receivers". In: *IEEE Journal of Selected Topics in Signal Processing* 3.4 (Aug. 2009), pp. 695–706. DOI: 10.1109/JSTSP.2009.2023831.
- [Clo+10] P. Closas and C. Fernández-Prades. "Bayesian Nonlinear Filters for Direct Position Estimation". In: *2010 IEEE Aerospace Conference*. Mar. 2010, pp. 1–12. DOI: 10.1109/AERO.2010.5446676.
- [Clo+17] P. Closas and A. Gusi-Amigo. "Direct Position Estimation of GNSS Receivers: Analyzing Main Results, Architectures, Enhancements, and Challenges". In: *IEEE Signal Processing Magazine* 34.5 (Sept. 2017), pp. 72–84. DOI: 10.1109/MSP.2017.2718040.
- [Cop+80] E. M. Copps et al. "Optimal Processing of GPS Signals". In: *NAVIGATION, Journal of the Institute of Navigation* 27.3 (1980), pp. 171–182.
- [Cun+16] M. Cuntz, A. Konovaltsev, and M. Meurer. "Concepts, Development, and Validation of Multiantenna GNSS Receivers for Resilient Navigation". In: *Proceedings of the IEEE* 104.6 (June 2016), pp. 1288–1301. DOI: 10.1109/JPROC.2016.2525764.
- [Dam21] J. Dampf. "Probability Analysis for Bayesian Directposition Estimation". Graz: Graz University of Technology, Feb. 2021. 244 pp.
- [Dan+14] S. Daneshmand, N. Sokhandan, and G. Lachapelle. "Precise GNSS Attitude Determination Based on Antenna Array Processing". In: *Proceedings of the 27th International Technical Meeting of the Satellite Division of The Institute of Navigation (ION GNSS+ 2014)*. Sept. 2014, pp. 2555–2562.
- [Don+15] A. Donges and R. Noll. "Laser Triangulation". In: *Laser Measurement Technology: Fundamentals and Applications*. Ed. by A. Donges and R. Noll. Berlin, Heidelberg: Springer, 2015, pp. 247–278. ISBN: 978-3-662-43634-9. DOI: 10.1007/978-3-662-43634-9_10.
- [Dov+04] F. Dovis, M. Pini, and P. Mulassano. "Turbo DLL: An Innovative Architecture for Multipath Mitigation in GNSS Receivers". In: *Proceedings of the 17th International Technical Meeting of the Satellite Division of The Institute of Navigation (ION GNSS 2004)*. Sept. 2004, pp. 1–7.
- [Enn+17] C. Enneking and F. Antreich. "Exploiting WSSUS Multipath for GNSS Ranging". In: *IEEE Transactions on Vehicular Technology* 66.9 (Sept. 2017), pp. 7663–7676. DOI: 10.1109/TVT.2017.2688724.

- [Erc+06] R. Ercek, P. De Doncker, and F. Grenez. “Statistical Study of NLOS-Multipath in Urban Canyons”. In: *European Journal of Navigation* 4.3 (2006), pp. 41–48.
- [Eur21a] European Union. *European GNSS (Galileo) Open Service: Service Definition Document (OS SDD)*. Nov. 2021.
- [Eur21b] European Union. *European GNSS (Galileo) Open Service: Signal-in-Space Interface Control Document (OS SIS ICD)*. Jan. 2021.
- [Eur24] European Union Agency for the Space Programme. *EUSPA EO and GNSS Market Report*. LU: Publications Office, Jan. 2024.
- [Far+18] R. Faragher et al. “Supercorrelation: Enhancing the Accuracy and Sensitivity of Consumer GNSS Receivers with a DSP Upgrade”. In: *Proceedings of the 31st International Technical Meeting of the Satellite Division of The Institute of Navigation (ION GNSS+ 2018)*. Sept. 2018, pp. 357–375. DOI: 10.33012/2018.15823.
- [Far88] Farebrother. *Linear Least Squares Computations*. CRC Press, Feb. 19, 1988. 322 pp. ISBN: 978-0-8247-7661-9.
- [Fen+05] P. C. Fenton and J. Jones. “The Theory and Performance of NovAtel Inc.’s Vision Correlator”. In: *Proceedings of the 18th International Technical Meeting of the Satellite Division of The Institute of Navigation (ION GNSS 2005)*. Sept. 2005, pp. 2178–2186.
- [Fes+94] J. A. Fessler and A. O. Hero. “Space-Alternating Generalized Expectation-Maximization Algorithm”. In: *IEEE Transactions on Signal Processing* 42.10 (Oct. 1994), pp. 2664–2677. DOI: 10.1109/78.324732.
- [Fle+99] B. Fleury et al. “Channel Parameter Estimation in Mobile Radio Environments Using the SAGE Algorithm”. In: *IEEE Journal on Selected Areas in Communications* 17.3 (Mar. 1999), pp. 434–450. DOI: 10.1109/49.753729.
- [Foh+17] F. Fohlmeister et al. “Dual Polarization Beamforming Algorithm for Multipath Mitigation in GNSS”. In: *Signal Processing* 138 (2017), pp. 86–97. DOI: 10.1016/j.sigpro.2017.03.012.
- [Fra+13] D. M. Franco-Patiño, G. Seco-Granados, and F. Dovis. “Signal Quality Checks for Multipath Detection in GNSS”. In: *2013 International Conference on Localization and GNSS (ICL-GNSS)*. June 2013, pp. 1–6. DOI: 10.1109/ICL-GNSS.2013.6577268.
- [Gar+96] L. Garin, F. van Diggelen, and J.-M. Rousseau. “Strobe & Edge Correlator Multipath Mitigation for Code”. In: *Proceedings of the 9th International Technical Meeting of the Satellite Division of The Institute of Navigation (ION GPS 1996)*. Kansas City, MO, Sept. 1996, pp. 657–664.
- [Gar+97] L. Garin and J.-M. Rousseau. “Enhanced Strobe Correlator Multipath Rejection for Code & Carrier”. In: *Proceedings of the 10th International Technical Meeting of the Satellite Division of The Institute of Navigation (ION GPS 1997)*. Sept. 1997, pp. 559–568.

- [Goa+74] C. C. Goad and L. Goodman. “A Modified Hopfield Tropospheric Refraction Correction Model”. In: *Fall Annual Meeting American Geophysical Union*. San Fransisco, CA, Dec. 1974.
- [Gro+10] P. D. Groves et al. “Novel Multipath Mitigation Methods Using a Dual-Polarization Antenna”. In: *Proceedings of the 23rd International Technical Meeting of the Satellite Division of The Institute of Navigation (ION GNSS 2010)*. Sept. 2010, pp. 140–151.
- [Gro+20] P. D. Groves et al. “Combining Inertially-aided Extended Coherent Integration (Supercorrelation) with 3D-Mapping-Aided GNSS”. In: *Proceedings of the 33rd International Technical Meeting of the Satellite Division of The Institute of Navigation (ION GNSS+ 2020)*. Sept. 2020, pp. 2327–2346. DOI: 10.33012/2020.17767.
- [Gro11] P. D. Groves. “Shadow Matching: A New GNSS Positioning Technique for Urban Canyons”. In: *The Journal of Navigation* 64.3 (July 2011), pp. 417–430. DOI: 10.1017/S0373463311000087.
- [Gun+19] S. Gunawardena, J. Raquet, and M. Carroll. “Correlator Beamforming for Multipath Mitigation in High-Fidelity GNSS Monitoring Applications”. In: *NAVIGATION* 66.1 (2019), pp. 169–183. DOI: 10.1002/navi.286.
- [Hah17] J. Hahn. “GPS-Galileo Time Offset (GGTO): Galileo Implementation Status and Performance”. In: *International Committee on GNSS (ICG) Working Group D*. Kyoto, Japan, Dec. 4, 2017.
- [Har+84] G. K. Hartmann and R. Leitingner. “Range Errors Due to Ionospheric and Tropospheric Effects for Signal Frequencies above 100 MHz”. In: *Bulletin géodésique* 58.2 (June 1984), pp. 109–136. DOI: 10.1007/BF02520897.
- [Hec+11] M. V. T. Heckler et al. “Development of Robust Safety-of-Life Navigation Receivers”. In: *IEEE Transactions on Microwave Theory and Techniques* 59.4 (Apr. 2011), pp. 998–1005. DOI: 10.1109/TMTT.2010.2103090.
- [Hen+18] P. Henkel et al. “Precise Positioning of Robots with Fusion of GNSS, INS, Odometry, Barometer, Local Positioning System and Visual Localization”. In: *Proceedings of the 31st International Technical Meeting of the Satellite Division of The Institute of Navigation (ION GNSS+ 2018)*. Sept. 2018, pp. 3078–3087. DOI: 10.33012/2018.16097.
- [Hof+01] B. Hofmann-Wellenhof, H. Lichtenegger, and J. Collins. *Global Positioning System. Theory and Practice*. 5th ed. Springer Verlag, Feb. 2001. ISBN: 978-3-211-83534-0. DOI: 10.1007/978-3-7091-6199-9.
- [Hsu+16] L.-T. Hsu, Y. Gu, and S. Kamijo. “3D Building Model-Based Pedestrian Positioning Method Using GPS/GLONASS/QZSS and Its Reliability Calculation”. In: *GPS Solutions* 20.3 (July 2016), pp. 413–428. DOI: 10.1007/s10291-015-0451-7.
- [Hsu13] L.-T. Hsu. “Integration of Vector Tracking Loop and Multipath Mitigation Technique and Its Assessment”. In: *Proceedings of the 26th Inter-*

- national Technical Meeting of the Satellite Division of The Institute of Navigation (ION GNSS+ 2013)*. Sept. 2013, pp. 3263–3278.
- [Ili+17] A. Iliopoulos et al. “Multicorrelator Signal Tracking and Signal Quality Monitoring for GNSS with Extended Kalman Filter”. In: *2017 IEEE Aerospace Conference*. Mar. 2017, pp. 1–10. DOI: 10.1109/AERO.2017.7943579.
- [Ili+18] A. Iliopoulos et al. “Multi-Frequency Kalman Filtering for Joint Ionospheric Delay and Multipath Mitigation”. In: *WSA 2018; 22nd International ITG Workshop on Smart Antennas*. Mar. 2018, pp. 1–8.
- [Ilt90] R. Iltis. “Joint Estimation of PN Code Delay and Multipath Using the Extended Kalman Filter”. In: *IEEE Transactions on Communications* 38.10 (Oct. 1990), pp. 1677–1685. DOI: 10.1109/26.61437.
- [Irs+03] M. Irsigler and B. Eissfeller. “Comparison of Multipath Mitigation Techniques with Consideration of Future Signal Structures”. In: *Proceedings of the 16th International Technical Meeting of the Satellite Division of The Institute of Navigation (ION GPS/GNSS 2003)*. Sept. 2003, pp. 2584–2592.
- [Irs+04] M. Irsigler, G. W. Hein, and B. Eissfeller. “Multipath Performance Analysis for Future GNSS Signals”. In: *Proceedings of the 2004 National Technical Meeting of The Institute of Navigation*. Jan. 28, 2004, pp. 225–238.
- [Irs+05] M. Irsigler, J. A. Avila-Rodriguez, and G. W. Hein. “Criteria for GNSS Multipath Performance Assessment”. In: *Proceedings of the 18th International Technical Meeting of the Satellite Division of The Institute of Navigation (ION GNSS 2005)*. Sept. 2005, pp. 2166–2177.
- [Jia+14] Z. Jiang and P. D. Groves. “NLOS GPS Signal Detection Using a Dual-Polarisation Antenna”. In: *GPS Solutions* 18.1 (Jan. 2014), pp. 15–26. DOI: 10.1007/s10291-012-0305-5.
- [Kan+98] S. M. Kanekal and M. S. Braasch. “Multipath Mitigation with Gated Signal Technique”. In: *Proceedings of the 54th Annual Meeting of The Institute of Navigation (1998)*. June 3, 1998, pp. 535–542.
- [Kao91] W.-W. Kao. “Integration of GPS and Dead-Reckoning Navigation Systems”. In: *Vehicle Navigation and Information Systems Conference, 1991*. Vol. 2. Oct. 1991, pp. 635–643. DOI: 10.1109/VNIS.1991.205808.
- [Kap+06] E. D. Kaplan and C. J. Hegarty, eds. *Understanding GPS: Principles and Applications*. 2nd ed. Boston: Artech House, 2006. 703 pp. ISBN: 978-1-58053-894-7.
- [Kas+23] Z. M. Kassas et al. “Navigation with Multi-Constellation LEO Satellite Signals of Opportunity: Starlink, OneWeb, Orbcomm, and Iridium”. In: *2023 IEEE/ION Position, Location and Navigation Symposium (PLANS)*. Apr. 2023, pp. 338–343. DOI: 10.1109/PLANS53410.2023.10140066.
- [Klo87] J. A. Klobuchar. “Ionospheric Time-Delay Algorithm for Single-Frequency GPS Users”. In: *IEEE Transactions on Aerospace and*

- Electronic Systems* AES-23.3 (May 1987), pp. 325–331. DOI: 10.1109/TAES.1987.310829.
- [Kos+10] T. Kos, I. Markežic, and J. Pokrajčić. “Effects of Multipath Reception on GPS Positioning Performance”. In: *Proceedings ELMAR-2010*. Sept. 2010, pp. 399–402.
- [Kra+10] B. Krach, P. Robertson, and R. Weigel. “An Efficient Two-Fold Marginalized Bayesian Filter for Multipath Estimation in Satellite Navigation Receivers”. In: *EURASIP Journal on Advances in Signal Processing* 2010.1 (1 Dec. 2010), pp. 1–12. DOI: 10.1155/2010/287215.
- [Lan+11] M. Langer et al. “Simulation and Efficient Implementation of a Multipath Estimating Delay Locked Loop Using FIMLA Algorithm”. In: *Proceedings of the 24th International Technical Meeting of the Satellite Division of The Institute of Navigation (ION GNSS 2011)*. Sept. 2011, pp. 1152–1161.
- [Lee+22] W. Lee et al. “Tightly-Coupled GNSS-aided Visual-Inertial Localization”. In: *2022 International Conference on Robotics and Automation (ICRA)*. May 2022, pp. 9484–9491. DOI: 10.1109/ICRA46639.2022.9811362.
- [Lee86] Y. C. Lee. “Analysis of Range and Position Comparison Methods as a Means to Provide GPS Integrity in the User Receiver”. In: *Proceedings of the 42nd Annual Meeting of The Institute of Navigation (1986)*. June 26, 1986.
- [Len+06] M. Lentmaier and B. Krach. “Maximum Likelihood Multipath Estimation in Comparison with Conventional Delay Lock Loops”. In: *Proceedings of the 19th International Technical Meeting of the Satellite Division of The Institute of Navigation (ION GNSS 2006)*. Sept. 2006, pp. 1741–1751.
- [Len+08] M. Lentmaier, B. Krach, and P. Robertson. “Bayesian Time Delay Estimation of GNSS Signals in Dynamic Multipath Environments”. In: *International Journal of Navigation and Observation* 2008 (Apr. 24, 2008). DOI: 10.1155/2008/372651.
- [Luo+14] Y. Luo et al. “Multipath Effects on Vector Tracking Algorithm for GNSS Signal”. In: *Science China Information Sciences* 57.10 (10 Oct. 2014), pp. 1–13. DOI: 10.1007/s11432-014-5153-1.
- [Mai+10] D. Maier and A. Kleiner. “Improved GPS Sensor Model for Mobile Robots in Urban Terrain”. In: *2010 IEEE International Conference on Robotics and Automation*. May 2010, pp. 4385–4390. DOI: 10.1109/ROBOT.2010.5509895.
- [Man+04] D. Manandhar, R. Shibasaki, and P.-L. Normark. “GPS Signal Analysis Using LHCP / RHCP Antenna and Software GPS Receiver”. In: *Proceedings of the 17th International Technical Meeting of the Satellite Division of The Institute of Navigation (ION GNSS 2004)*. Sept. 2004, pp. 2489–2498.
- [McG+99] G. A. McGraw and M. S. Braasch. “GNSS Multipath Mitigation Using Gated and High Resolution Correlator Concepts”. In: *Proceedings of the*

- 1999 *National Technical Meeting of The Institute of Navigation*. Jan. 27, 1999, pp. 333–342.
- [Meg+09] J.-i. Meguro et al. “GPS Multipath Mitigation for Urban Area Using Omnidirectional Infrared Camera”. In: *IEEE Transactions on Intelligent Transportation Systems* 10.1 (Mar. 2009), pp. 22–30. DOI: 10.1109/ITITS.2008.2011688.
- [Mei+07] O. Meister et al. “Development of a GPS/INS/MAG Navigation System and Waypoint Navigator for a VTOL UAV”. In: *Unmanned Systems Technology IX*. Vol. 6561. SPIE, May 2, 2007, pp. 399–408. DOI: 10.1117/12.718623.
- [Mel+20] F. T. Melman et al. “Using Broadcast Time Offsets for Multi-Constellation Users in Harsh Environments”. In: *Proceedings of the 51st Annual Precise Time and Time Interval Systems and Applications Meeting*. Jan. 24, 2020, pp. 267–278. DOI: 10.33012/2020.17305.
- [Mis+06] P. Misra and P. Enge. *Global Positioning System: Signals, Measurements, and Performance*. 2nd ed. Ganga-Jamuna Press, 2006. 587 pp. ISBN: 978-0-9709544-2-8.
- [Mor+16] J. J. Morales, P. F. Roysdon, and Z. M. Kassas. “Signals of Opportunity Aided Inertial Navigation”. In: *Proceedings of the 29th International Technical Meeting of the Satellite Division of The Institute of Navigation (ION GNSS+ 2016)*. Sept. 2016, pp. 1492–1501. DOI: 10.33012/2016.14652.
- [Mor+21] Y. J. Morton et al. *Position, Navigation, and Timing Technologies in the 21st Century: Integrated Satellite Navigation, Sensor Systems, and Civil Applications*. John Wiley & Sons, 2021. ISBN: 978-1-119-45841-8. DOI: 10.1002/9781119458449.
- [Mub+10a] O. M. Mubarak and A. G. Dempster. “Analysis of Early Late Phase in Single-and Dual-Frequency GPS Receivers for Multipath Detection”. In: *GPS Solutions* 14.4 (Sept. 2010), pp. 381–388. DOI: 10.1007/s10291-010-0162-z.
- [Mub+10b] O. M. Mubarak and A. G. Dempster. “Exclusion of Multipath-Affected Satellites Using Early Late Phase”. In: *Journal of Global Positioning Systems* 9.2 (2010), pp. 145–155.
- [Ner+15] A. Neri, S. Sabina, and U. Mascia. “GNSS and Odometry Fusion for High Integrity and High Availability Train Control Systems”. In: *Proceedings of the 28th International Technical Meeting of the Satellite Division of The Institute of Navigation (ION GNSS+ 2015)*. Sept. 2015, pp. 639–648.
- [Nun+07] F. D. Nunes, F. M. G. Sousa, and J. M. N. Leitao. “Nonlinear Least-Squares Algorithm for Close-in Multipath Mitigation in GNSS Receivers”. In: *Proceedings of the 20th International Technical Meeting of the Satellite Division of The Institute of Navigation (ION GNSS 2007)*. Sept. 2007, pp. 1683–1691.
- [Nun+08] F. D. Nunes, F. M. G. Sousa, and J. M. N. Leitao. “BOC/MBOC Multicorrelator Receiver with Least-Squares Multipath Mitigation Tech-

- nique". In: *Proceedings of the 21st International Technical Meeting of the Satellite Division of The Institute of Navigation (ION GNSS 2008)*. Sept. 2008, pp. 652–662.
- [Obs+12] M. Obst, S. Bauer, and G. Wanielik. "Urban Multipath Detection and Mitigation with Dynamic 3D Maps for Reliable Land Vehicle Localization". In: *Proceedings of the 2012 IEEE/ION Position, Location and Navigation Symposium*. Apr. 2012, pp. 685–691. DOI: 10.1109/PLANS.2012.6236944.
- [Pan+08] T. Pany and B. Eissfeller. "Demonstration of a Synthetic Phased Array Antenna for Carrier/Code Multipath Mitigation". In: *Proceedings of the 21st International Technical Meeting of the Satellite Division of The Institute of Navigation (ION GNSS 2008)*. Sept. 2008, pp. 663–668.
- [Pan+13] T. Pany et al. "GNSS Synthetic Aperture Processing with Artificial Antenna Motion". In: *Proceedings of the 26th International Technical Meeting of the Satellite Division of The Institute of Navigation (ION GNSS+ 2013)*. Sept. 2013, pp. 3163–3171.
- [Pan10] T. Pany. *Navigation Signal Processing for GNSS Software Receivers*. Artech House, 2010. 352 pp. ISBN: 978-1-60807-027-5.
- [Par+96] B. W. Parkinson and J. J. Spilker Jr. *Global Positioning System: Theory and Applications, Volume II*. AIAA, 1996. 830 pp. ISBN: 978-1-60086-419-3.
- [Pey+13] S. Peyraud et al. "About Non-Line-Of-Sight Satellite Detection and Exclusion in a 3D Map-Aided Localization Algorithm". In: *Sensors* 13.1 (1 Jan. 11, 2013), pp. 829–847. DOI: 10.3390/s130100829.
- [Phe01] R. E. Phelts. "Multicorrelator Techniques for Robust Mitigation of Threats to GPS Signal Quality". PhD thesis. Stanford University, June 2001.
- [Piñ+11] C. Piñana-Diaz et al. "GPS Multipath Detection and Exclusion with Elevation-Enhanced Maps". In: *2011 14th International IEEE Conference on Intelligent Transportation Systems (ITSC)*. Oct. 2011, pp. 19–24. DOI: 10.1109/ITSC.2011.6083042.
- [Pra04] A. R. Pratt. "Performance of Multi-path Mitigation Techniques at Low Signal to Noise Ratios". In: *Proceedings of the 17th International Technical Meeting of the Satellite Division of The Institute of Navigation (ION GNSS 2004)*. Sept. 2004, pp. 43–53.
- [Pra14] K. M. M. Prabhu. *Window Functions and Their Applications in Signal Processing*. Taylor & Francis, 2014. 404 pp. ISBN: 978-1-4665-1584-0. DOI: 10.1201/9781315216386.
- [Pro+22] F. S. Prol et al. "Position, Navigation, and Timing (PNT) Through Low Earth Orbit (LEO) Satellites: A Survey on Current Status, Challenges, and Opportunities". In: *IEEE Access* 10 (2022), pp. 83971–84002. DOI: 10.1109/ACCESS.2022.3194050.
- [Rib+07] C. B. Ribeiro, A. Richter, and V. Koivunen. "Joint Angular- and Delay-Domain MIMO Propagation Parameter Estimation Using Approximate

- ML Method". In: *IEEE Transactions on Signal Processing* 55.10 (Oct. 2007), pp. 4775–4790. DOI: 10.1109/TSP.2007.896247.
- [Ris78] J. Rissanen. "Modeling by Shortest Data Description". In: *Automatica* 14.5 (Sept. 1978), pp. 465–471. DOI: 10.1016/0005-1098(78)90005-5.
- [Saa96] H. Saarnisaari. "ML Time Delay Estimation in a Multipath Channel". In: *Proceedings of ISSSTA'95 International Symposium on Spread Spectrum Techniques and Applications*. Vol. 3. Sept. 1996, pp. 1007–1011. DOI: 10.1109/ISSSTA.1996.563457.
- [Sah+07] M. Sahmoudi and M. G. Amin. "Optimal Robust Beamforming for Interference and Multipath Mitigation in GNSS Arrays". In: *2007 IEEE International Conference on Acoustics, Speech and Signal Processing - ICASSP '07*. Vol. 3. Apr. 2007, pp. III–693. DOI: 10.1109/ICASSP.2007.366774.
- [Sah+08] M. Sahmoudi and M. G. Amin. "Fast Iterative Maximum-Likelihood Algorithm (FIMLA) for Multipath Mitigation in the Next Generation of GNSS Receivers". In: *IEEE Transactions on Wireless Communications* 7.11 (Nov. 2008), pp. 4362–4374. DOI: 10.1109/T-WC.2008.070700.
- [Sah+09] M. Sahmoudi and M. G. Amin. "Robust Tracking of Weak GPS Signals in Multipath and Jamming Environments". In: *Signal Processing* 89.7 (July 2009), pp. 1320–1333. DOI: 10.1016/j.sigpro.2009.01.001.
- [Sch+05] R. Schmid et al. "Absolute Phase Center Corrections of Satellite and Receiver Antennas". In: *GPS Solutions* 9.4 (Nov. 2005), pp. 283–293. DOI: 10.1007/s10291-005-0134-x.
- [Sch+16] M. Schreiber et al. "Vehicle Localization with Tightly Coupled GNSS and Visual Odometry". In: *2016 IEEE Intelligent Vehicles Symposium (IV)*. June 2016, pp. 858–863. DOI: 10.1109/IVS.2016.7535488.
- [Sci+09] F. Scire-Scappuzzo and S. N. Makarov. "A Low-Multipath Wideband GPS Antenna With Cutoff or Non-Cutoff Corrugated Ground Plane". In: *IEEE Transactions on Antennas and Propagation* 57.1 (Jan. 2009), pp. 33–46. DOI: 10.1109/TAP.2008.2009655.
- [Sel04a] J. Selva Vera. "Complexity Reduction in the Parametric Estimation of Superimposed Signal Replicas". In: *Signal Processing* 84.12 (Dec. 2004), pp. 2325–2343. DOI: 10.1016/j.sigpro.2004.07.026.
- [Sel04b] J. Selva Vera. "Efficient Multipath Mitigation in Navigation Systems". PhD thesis. Universitat Politècnica de Catalunya, Feb. 9, 2004.
- [Sha+85] T.-J. Shan, M. Wax, and T. Kailath. "On Spatial Smoothing for Direction-of-Arrival Estimation of Coherent Signals". In: *IEEE Transactions on Acoustics, Speech, and Signal Processing* 33.4 (Aug. 1985), pp. 806–811. DOI: 10.1109/TASSP.1985.1164649.
- [Shy+16] E. Shytermeja, A. J. Garcia Peña, and O. Julien. "Performance Comparison of a Proposed Vector Tracking Architecture versus the Scalar Configuration for a L1/E1 GPS/Galileo Receiver". In: *ENC 2016, European Navigation Conference*. IEEE, May 30, 2016, ISBN : 9781479989164.
- [Sie+21a] C. Siebert, A. Konovaltsev, and M. Meurer. "Multipath Rejection Using Multi-Signal Multicorrelator Based GNSS Receiver With an Extended

- Kalman Filter”. In: *Proceedings of the 34th International Technical Meeting of the Satellite Division of The Institute of Navigation (ION GNSS+ 2021)*. Sept. 2021, pp. 3422–3436. DOI: 10.33012/2021.17980.
- [Sie+21b] C. Siebert, A. Konovaltsev, and M. Meurer. “Multipath Rejection Using Multicorrelator Based GNSS Receiver With an Extended Kalman Filter”. In: *Proceedings of the 2021 International Technical Meeting of The Institute of Navigation*. Jan. 2021, pp. 269–281. DOI: 10.33012/2021.17832.
- [Sie+21c] C. Siebert, A. Konovaltsev, and M. Meurer. “New Multipath Rejection Method: Multicorrelator Receiver with Extended Kalman Filter”. In: *Inside GNSS - Global Navigation Satellite Systems Engineering, Policy, and Design* (Sept. 20, 2021).
- [Sie+22a] C. Siebert, A. Konovaltsev, and M. Meurer. “Multipath Rejection Using Multi-Correlator Based GNSS Receiver in Vector Tracking Loops”. In: *Proceedings of the 35th International Technical Meeting of the Satellite Division of The Institute of Navigation (ION GNSS+ 2022)*. Sept. 2022, pp. 2042–2053. DOI: 10.33012/2022.18327.
- [Sie+22b] C. Siebert, A. Konovaltsev, and M. Meurer. “Multipath Rejection Using Multi-Frequency Multi-Correlator Based GNSS Receiver With an Extended Kalman Filter”. In: *Proceedings of the 2022 International Technical Meeting of The Institute of Navigation*. Jan. 2022, pp. 1039–1053. DOI: 10.33012/2022.18200.
- [Sie+23a] C. Siebert, A. Konovaltsev, and M. Meurer. “Development and Validation of a Multipath Mitigation Technique Using Multi-Correlator Structures”. In: *NAVIGATION: Journal of the Institute of Navigation* 70.4 (Aug. 9, 2023). DOI: 10.33012/navi.609.
- [Sie+23b] C. Siebert, A. Konovaltsev, and M. Meurer. “Low-Complexity Multipath Mitigation Technique Based on Multi-Correlator Structures”. In: *2023 IEEE/ION Position, Location and Navigation Symposium (PLANS)*. Apr. 2023, pp. 935–945. DOI: 10.1109/PLANS53410.2023.10140016.
- [Sie+24] C. Siebert, A. Konovaltsev, and M. Meurer. “Novel Multipath Mitigation Technique for Antenna Arrays Based on Multi-Correlator Structures”. In: *Proceedings of the 2024 International Technical Meeting of The Institute of Navigation*. Jan. 2024, pp. 917–930. DOI: 10.33012/2024.19548.
- [Sle+01] J. M. Sleewaegen and F. Boon. “Mitigating Short-Delay Multipath: A Promising New Technique”. In: *Proceedings of the 14th International Technical Meeting of the Satellite Division of The Institute of Navigation (ION GPS 2001)*. Salt Lake City, UT, Sept. 2001, pp. 204–213.
- [Sok+16] N. Sokhandan et al. “An Advanced GNSS Code Multipath Detection and Estimation Algorithm”. In: *GPS Solutions* 20.4 (Oct. 1, 2016), pp. 627–640. DOI: 10.1007/s10291-015-0475-z.

- [Sou+02] J. Soubielle et al. “GPS Positioning in a Multipath Environment”. In: *IEEE Transactions on Signal Processing* 50.1 (Jan. 2002), pp. 141–150. DOI: 10.1109/78.972490.
- [Spi+96] J. J. Spilker Jr. et al., eds. *Global Positioning System: Theory and Applications, Volume I*. Washington DC: American Institute of Aeronautics and Astronautics, 1996. ISBN: 978-1-56347-106-3. DOI: 10.2514/4.866388.
- [Ste+04] A. Steingass and A. Lehner. “Measuring the Navigation Multipath Channel – A Statistical Analysis”. In: *Proceedings of the 17th International Technical Meeting of the Satellite Division of The Institute of Navigation (ION GNSS 2004)*. Long Beach, CA, Sept. 2004, pp. 1157–1164.
- [Sto+90] P. Stoica and A. Nehorai. “Performance Study of Conditional and Unconditional Direction-of-Arrival Estimation”. In: *IEEE Transactions on Acoustics, Speech, and Signal Processing* 38.10 (Oct. 1990), pp. 1783–1795. DOI: 10.1109/29.60109.
- [Suz+12] T. Suzuki and N. Kubo. “GNSS Positioning with Multipath Simulation Using 3D Surface Model in Urban Canyon”. In: *Proceedings of the 25th International Technical Meeting of the Satellite Division of The Institute of Navigation (ION GNSS 2012)*. Sept. 2012, pp. 438–447.
- [Suz+13] T. Suzuki and N. Kubo. “Correcting GNSS Multipath Errors Using a 3D Surface Model and Particle Filter”. In: *Proceedings of the 26th International Technical Meeting of the Satellite Division of The Institute of Navigation (ION GNSS+ 2013)*. Sept. 2013, pp. 1583–1595.
- [Suz+14] T. Suzuki and N. Kubo. “N-LOS GNSS Signal Detection Using Fish-Eye Camera for Vehicle Navigation in Urban Environments”. In: *Proceedings of the 27th International Technical Meeting of the Satellite Division of The Institute of Navigation (ION GNSS+ 2014)*. Sept. 2014, pp. 1897–1906.
- [Suz16] T. Suzuki. “Integration of GNSS Positioning and 3D Map Using Particle Filter”. In: *Proceedings of the 29th International Technical Meeting of the Satellite Division of The Institute of Navigation (ION GNSS+ 2016)*. Sept. 2016, pp. 1296–1304. DOI: 10.33012/2016.14857.
- [Tak+09] T. Takasu and A. Yasuda. “Development of the Low-Cost RTK-GPS Receiver with an Open Source Program Package RTKLIB”. In: *Proceedings of the International Symposium on GPS/GNSS*. Jeju, Korea, Nov. 4–6, 2009.
- [Teu+17] P. J. G. Teunissen and O. Montenbruck, eds. *Springer Handbook of Global Navigation Satellite Systems*. 1st ed. Springer, Cham, 2017. 1335 pp. ISBN: 978-3-319-42926-7. DOI: 10.1007/978-3-319-42928-1.
- [Tow+94] B. R. Townsend and P. Fenton. “A Practical Approach to the Reduction of Pseudorange Multipath Errors in a L1 GPS Receiver”. In: *Proceedings of the 7th International Technical Meeting of the Satellite Division of The Institute of Navigation (ION GPS 1994)*. Sept. 1994, pp. 143–148.

- [Tow+95] B. R. Townsend et al. "Performance Evaluation of the Multipath Estimating Delay Lock Loop". In: *NAVIGATION* 42.3 (Sept. 1995), pp. 502–514. DOI: 10.1002/j.2161-4296.1995.tb01903.x.
- [Tre04] H. L. V. Trees. *Optimum Array Processing: Part IV of Detection, Estimation, and Modulation Theory*. John Wiley & Sons, Mar. 2004. 1472 pp. ISBN: 978-0-471-46383-2. DOI: 10.1002/0471221104.
- [Vag+16] N. Vagle et al. "Performance Analysis of GNSS Multipath Mitigation Using Antenna Arrays". In: *The Journal of Global Positioning Systems* 14.1 (Nov. 4, 2016), pp. 1–15. DOI: 10.1186/s41445-016-0004-6.
- [Van+92] A. J. Van Dierendonck, P. Fenton, and T. Ford. "Theory and Performance of Narrow Correlator Spacing in a GPS Receiver". In: *NAVIGATION* 39.3 (1992), pp. 265–283. DOI: 10.1002/j.2161-4296.1992.tb02276.x.
- [Van+97] A. J. Van Dierendonck and M. S. Braasch. "Evaluation of GNSS Receiver Correlation Processing Techniques for Multipath and Noise Mitigation". In: *Proceedings of the 1997 National Technical Meeting of The Institute of Navigation*. Jan. 16, 1997, pp. 207–215.
- [vGra+93] F. van Graas and J. L. Farrell. "Baseline Fault Detection and Exclusion Algorithm". In: *Proceedings of the 49th Annual Meeting of The Institute of Navigation (1993)*. June 23, 1993, pp. 413–420.
- [vNee+94] R. D. J. van Nee et al. "The Multipath Estimating Delay Lock Loop: Approaching Theoretical Accuracy Limits". In: *Proceedings of 1994 IEEE Position, Location and Navigation Symposium - PLANS'94*. Las Vegas, NV, Apr. 1994, pp. 246–251. DOI: 10.1109/PLANS.1994.303320.
- [vNee92a] R. D. J. van Nee. "Multipath Effects on GPS Code Phase Measurements". In: *NAVIGATION* 39.2 (1992), pp. 177–190. DOI: 10.1002/j.2161-4296.1992.tb01873.x.
- [vNee92b] R. D. J. van Nee. "The Multipath Estimating Delay Lock Loop". In: *IEEE Second International Symposium on Spread Spectrum Techniques and Applications (ISSSTA'92)*. Nov. 1992, pp. 39–42. DOI: 10.1109/ISSSTA.1992.665623.
- [Wan+13] L. Wang, P. D. Groves, and M. K. Ziebart. "GNSS Shadow Matching: Improving Urban Positioning Accuracy Using a 3D City Model with Optimized Visibility Scoring Scheme". In: *NAVIGATION* 60.3 (2013), pp. 195–207. DOI: 10.1002/navi.38.
- [War98] P. W. Ward. "Performance Comparisons Between FLL, PLL and a Novel FLL-Assisted-PLL Carrier Tracking Loop Under RF Interference Conditions". In: *Proceedings of the 11th International Technical Meeting of the Satellite Division of The Institute of Navigation (ION GPS 1998)*. Sept. 1998, pp. 783–795.
- [Wax+85] M. Wax and T. Kailath. "Detection of Signals by Information Theoretic Criteria". In: *IEEE Transactions on Acoustics, Speech, and Signal Processing* 33.2 (Apr. 1985), pp. 387–392. DOI: 10.1109/TASSP.1985.1164557.

- [Wei02] L. R. Weill. “Multipath Mitigation Using Modernized GPS Signals: How Good Can It Get?” In: *Proceedings of the 15th International Technical Meeting of the Satellite Division of The Institute of Navigation (ION GPS 2002)*. Sept. 2002, pp. 493–505.
- [Wei97] L. R. Weill. “GPS Multipath Mitigation by Means of Correlator Reference Waveform Design”. In: *Proceedings of the 1997 National Technical Meeting of The Institute of Navigation*. Santa Monica, CA, Jan. 16, 1997, pp. 197–206.
- [Wei98] L. R. Weill. “Application of Superresolution Concepts to the GPS Multipath Mitigation Problem”. In: *Proceedings of the 1998 National Technical Meeting of The Institute of Navigation*. Jan. 23, 1998, pp. 673–682.
- [Wen+15] F. Wendler et al. “Dual-Polarization Time Delay Estimation for Multipath Mitigation”. In: *WSA 2015; 19th International ITG Workshop on Smart Antennas*. Mar. 2015, pp. 1–6.
- [Win00] J. Ó. Winkel. “Modeling and Simulating GNSS Signal Structures and Receivers”. PhD thesis. Universität der Bundeswehr München, 2000. 247 pp.
- [Xie+17] L. Xie et al. “Mitigating Multipath Bias Using a Dual-Polarization Antenna: Theoretical Performance, Algorithm Design, and Simulation”. In: *Sensors* 17.2 (2 Feb. 13, 2017), p. 359. DOI: 10.3390/s17020359.
- [Yoz+15] R. Yozevitch and B. ben Moshe. “A Robust Shadow Matching Algorithm for GNSS Positioning”. In: *NAVIGATION* 62.2 (2015), pp. 95–109. DOI: 10.1002/navi.85.
- [Zie17] N. I. Ziedan. “Urban Positioning Accuracy Enhancement Utilizing 3D Buildings Model and Accelerated Ray Tracing Algorithm”. In: *Proceedings of the 30th International Technical Meeting of the Satellite Division of The Institute of Navigation (ION GNSS+ 2017)*. Sept. 2017, pp. 3253–3268. DOI: 10.33012/2017.15366.
- [Zor+16] S. Zorn et al. “Self-Contained Calibration Determination by Jointly Solving the Attitude Estimation and Calibration Problem in the Steering Vector Domain”. In: *2016 8th ESA Workshop on Satellite Navigation Technologies and European Workshop on GNSS Signals and Signal Processing (NAVITEC)*. Dec. 2016, pp. 1–9. DOI: 10.1109/NAVITEC.2016.7849321.
- [Zor+20] S. Zorn et al. “Accurate Position and Attitude Determination in a Severe Multipath Environment Using an Uncalibrated Multi-Antenna-System”. In: *2020 IEEE/ION Position, Location and Navigation Symposium (PLANS)*. Apr. 2020, pp. 1247–1255. DOI: 10.1109/PLANS46316.2020.9110151.

Curriculum Vitae

07.04.2025	Doctoral Examination for Dr.-Ing.
2020 – 2025	Doctoral Candidate at Chair of Navigation RWTH Aachen University, Germany
2017 – 2019	Master of Science Electrical Engineering, Information Technology and Computer Engineering RWTH Aachen University, Germany
2013 – 2016	Bachelor of Science Electrical Engineering and Information Technology TU Darmstadt, Germany
2005 – 2013	General Higher Education Entrance Qualification (Abitur) Lichtenbergschule, Darmstadt, Germany
1995	Born in Kassel, Germany